

Effect of Starting Microstructure and CGL Compatible Thermal  
Processing Cycle on the Mechanical Properties of a Medium Mn  
Third Generation Advanced High Strength Steel

Effect of Starting Microstructure and CGL Compatible Thermal  
Processing Cycle on the Mechanical Properties of a Medium Mn  
Third Generation Advanced High Strength Steel

BY KAZI BHADHON, B. SC.

A Thesis

Submitted to the Department of Materials Science & Engineering

and the School of Graduate Studies

in Partial Fulfilment of the Requirements

for the Degree

Master of Applied Science

McMaster University

© Copyright by Kazi Bhadhon May 2017

Master of Applied Science (2017)  
(Materials Science & Engineering)

McMaster University  
Hamilton, Ontario, Canada

TITLE: Effect of Starting Microstructure and CGL Compatible  
Thermal Processing Cycle on the Mechanical Properties of a  
Medium Mn Third Generation Advanced High Strength  
Steel

AUTHOR: Kazi Bhadhon, B. Sc.

SUPERVISOR: Dr. Joseph R. McDermid

NUMBER OF PAGES: xviii, 148

## Abstract

Medium Mn TRIP steels are amongst the most widely researched third generation advanced high strength steels (3G-AHSSs) as they are ideal candidates for automotive light-weighting applications owing to their superior strength and ductility balance. However, the thermal processing cycles of these steels need to be compatible with the industrial continuous galvanizing line (CGL) in order to successfully employ them in the automotive manufacturing industry. The main objective of the present research was to develop a CGL compatible thermal processing cycle for a prototype medium Mn steel (Fe-0.2C-6Mn-1.5Si-0.5Al-0.5Cr wt.%) that would produce significant volume fractions of chemically stable retained austenite and exhibit mechanical properties consistent with established 3G-AHSS targets.

The effects of intercritical annealing (IA) time and temperature and starting microstructure were determined in the first part of this research. The as-received tempered martensite (S-TM) and heat treated martensite (S-M) were the two different starting microstructures studied in this research. In this case, the overaging temperature (OT) treatment (460°C for 20s) was kept constant. It was found that the retained austenite volume fraction increased significantly with both increasing IA temperatures and IA holding times for the S-TM samples, with the S-TM 710°C + 600s sample yielding the highest retained austenite volume fractions (~0.37). However, similar volume fractions ( $\geq 0.30$ ) of retained austenite were achieved for the S-M samples intercritically annealed at 675°C for shorter times (i.e. 60 to 360s). SEM and TEM analysis revealed that the ultra-fine grained microstructure of the annealed samples consisted of ferrite/bainitic ferrite, retained

austenite and athermal martensite. Moreover, dark field TEM analysis of the S-M samples showed that most of the retained austenite was present in a film type morphology, which is known to be more stable chemically and mechanically compared to the block type morphology. The tensile test results showed that both the S-TM and S-M samples exhibited a high strength/ductility balance, as exemplified by having a  $UTS \times TE$  product in excess of 30,000 MPa%), meeting the 3G-AHSS target mechanical properties. However, the S-M starting microstructure, particularly the S-M 675°C + 120s samples, showed more potential in terms of CGL compatibility and achieving 3G-AHSS target mechanical properties owing to their faster austenite reversion transformation (ART) kinetics during intercritical annealing which produced higher volume fractions of chemically stable retained austenite for shorter, CGL-compatible intercritical annealing times. This chemically stable retained austenite gradually transformed to martensite during deformation and resulted in the maintenance of high work hardening rates at high strains. As a result, the onset of necking was delayed resulting in a superior strength and ductility balance in these annealed steels.

The effect of OT holding time was determined in the second part of this research. In that regard, the OT holding time was varied from 20s to 120s for selected S-TM and S-M samples. The S-TM 710°C samples with increased OT holding times (60s and 120s) had a significant increase in retained austenite volume fraction compared to the baseline 20s OT samples. However, the retained austenite volume fractions did not change for the S-M samples regardless of OT holding time. It was also found that the mechanical properties of the annealed S-TM and S-M steels depended on the OT holding time. For the S-TM samples with > 120s IA holding times, longer OT holding times (60s and 120s) produced chemically

unstable retained austenite which transformed rapidly at low strain resulting in low UTS  $\times$  TE products (less than 20,000 MPa%). However, although longer OT holding times significantly increased the yield strength of the annealed S-M samples, the UTS  $\times$  TE product decreased significantly owing to decreased retained austenite stability. It was also determined that the main fracture mechanism was classic void nucleation and coalescence along the grain boundaries for all of the starting microstructures and heat treatments explored.

Finally, based on the results of this research, it was concluded that the prototype medium Mn TRIP steel can achieve 3G-AHSS target mechanical properties using CGL-compatible thermal processing cycles. Moreover, depending on successful reactive wetting, it may be possible to perform both thermal processing and galvanizing of this steel in the industrial CGL.

## **Acknowledgements**

First of all, I would like to thank my supervisor, Dr. Joseph R. McDermid, for giving me the opportunity to work in his research group where I have learnt a lot. Furthermore, his valuable knowledge and continuous guidance helped me throughout this research project.

I would also like to thank the following people for their assistance with the experimental work: John Thomson and Raymond Fullerton (Galvanizing Simulator) from the McMaster Steel Research Centre, Dr. Xiaogang Li and Doug Culley for their help in the MSE labs, Dr. Glynis de Silveira and Chris Butcher (SEM training) from the Canadian Centre for Electron Microscopy (CCEM), Dr. James Britten and Victoria Jarvis (XRD analysis) from the McMaster Analytical X-Ray Facility (MAX), Dr. Connie Barry, Dr. Mike Bruhis and Dr. Elizabeth McNally from the Centre for Automotive Materials and Corrosion (CAMC), Dr. Xiang Wang (TEM analysis) and all the CAMC group members for their valuable feedbacks.

I would also like to acknowledge the members of the International Zinc Association Galvanized Autobody Partnership (IZA-GAP) program for their financial support and US Steel Research for the provision of the steel substrates used in this research.

Last, but not the least, I am grateful to my family and friends for their unconditional support and trust in me to do something good. Finally, I really appreciate all the sacrifices (especially moving to Canada) that my wife Fatema Tuj Zohra had to make in order to support me.

## Table of Contents

Abstract .....	iii
Acknowledgements .....	vi
List of Figures .....	ix
List of Tables .....	xviii
1 INTRODUCTION .....	1
1.1 Advanced High Strength Steels (AHSSs) in Automotive Industry.....	1
1.2 CGL Compatible Thermal Processing Cycle .....	4
2 LITERATURE REVIEW .....	7
2.1 Development of Third Generation Advanced High Strength Steels .....	7
2.2 Medium Mn TRIP Steels.....	8
2.3 Strengthening Mechanisms .....	10
2.3.1 Solid Solution Strengthening .....	10
2.3.2 Composite Strengthening .....	12
2.3.3 TRIP Effect .....	15
2.3.4 TWIP Effect .....	18
2.4 Effect of Starting Microstructure .....	21
2.5 Austenite Reversion Transformation (ART).....	25
2.6 Effect of Intercritical Annealing Parameters.....	30
2.7 Effect of Overaging Temperature (OT) Treatment Parameters .....	39
2.8 Effect of Heating Rate .....	41
2.9 Effect of Cooling Rate.....	45
2.10 Fracture Mechanisms.....	47
3 RESEARCH OBJECTIVES .....	50
4 EXPERIMENTAL .....	51
4.1 Material Chemistry and Sample Preparation .....	51
4.2 McMaster Galvanizing Simulator (MGS).....	52
4.3 ThermoCalc Calculations .....	56
4.4 Dilatometry and Starting Microstructures .....	57
4.5 Thermal Processing Cycle.....	59
4.6 Analysis Techniques .....	62

4.6.1	X-ray Diffraction.....	62
4.6.2	Scanning Electron Microscopy .....	63
4.6.3	Transmission Electron Microscopy .....	64
4.6.4	Tensile Testing.....	65
5	RESULTS .....	67
5.1	Effect of Intercritical Annealing Temperature and Holding Time.....	67
5.1.1	XRD Results .....	67
5.1.2	Microstructural Characterization by SEM .....	70
5.1.3	Microstructural Characterization by TEM.....	76
5.1.4	Mechanical Properties.....	87
5.1.5	Interrupted Tensile Tests.....	94
5.1.6	Fractography .....	95
5.2	Effect of Overaging Temperature Holding Time .....	99
5.2.1	XRD Results .....	99
5.2.2	Microstructural Characterization by SEM .....	102
5.2.3	Mechanical Properties.....	105
5.2.4	Interrupted Tensile Tests.....	115
5.2.5	Fractography .....	118
5.3	Results Summary.....	122
6	DISCUSSION .....	126
6.1	Effect of Intercritical Annealing Parameters on S-TM Samples.....	126
6.2	Effect of Starting Microstructure .....	130
6.3	Effect of Overaging Temperature Holding Time.....	135
7	CONCLUSIONS AND RECOMMENDATIONS FOR FUTURE STUDY .....	140
7.1	Conclusions .....	140
7.2	Recommendations for Future Study.....	142
8	REFERENCES .....	143

## List of Figures

Figure 1.1: A schematic of different steel grades used in the construction of 2016 Chevrolet Malibu and 2017 Buick LaCrosse body-in-white. ....	1
Figure 1.2: AHSS classification and U.S. D.O.E. target mechanical properties for 3G-AHSSs.....	2
Figure 1.3: Schematic of a continuous galvanizing/galvannealing line. ....	6
Figure 2.1: Effect of alloying elements on solid solution strengthening of ferrite .....	11
Figure 2.2: Nanohardness results for the different phases in a 0.29% C, 1.42% Mn and 1.41% Si TRIP-assisted steel where F = ferrite, B = bainitic ferrite, A = retained austenite and M = martensite .....	13
Figure 2.3: Comparison of the macroscopic stress and the stress calculated without taking the martensitic phase into account .....	14
Figure 2.4: Effect of austenite stability on predicted mechanical property combinations: a) four different austenite stability and b) corresponding predicted mechanical property combinations where each data point corresponds to an initial austenite volume fraction	15
Figure 2.5: BF and DF TEM micrographs illustrating the dislocations generated in the ferrite at the tip of the strain-induced martensitic variants .....	16
Figure 2.6: Fraction retained austenite vs a) normalized reduced stress and b) true strain .....	17

Figure 2.7: Intercritical annealing temperature diagram for a Fe-0.15 pct C-6.0 pct Mn-1.5 pct Si-3.0 pct Al steel .....	20
Figure 2.8: Comparison of the work hardening of 0.08 pct C-6 pct Mn-1.5 pct Si-2.0 pct Al-0.08 pct V steel (taken from [40]) and Fe-0.15 pct C-6.0 pct Mn-1.5 pct Si-3.0 pct Al steel .....	20
Figure 2.9: Dependence of tensile properties and retained austenite amount on starting microstructure, annealing temperature and carbon content of the steels .....	22
Figure 2.10: Comparison of EPMA Mn map (A) with the microstructure after Dino etching observed in OM (B) for the sample after second annealing at 670°C for 7 hr .....	24
Figure 2.11: TEM micrographs showing morphology and distribution of austenite grains in the specimens reversion-treated at a) 873 K for 10.8 ks, b) 913 K for 1.8 ks and c) 953 K for 0.18 ks .....	26
Figure 2.12: Variations of a) volume fraction of austenite, b) C concentration at the boundary in austenite (solid curve) and ferrite (dashed curve), c) Mn concentration and d) Si concentration during holding at 760°C.....	28
Figure 2.13: DICTRA calculation of C, Mn and Si profile across the ferrite-austenite phase boundary at different times during intercritical annealing; the arrow indicating the direction of the phase boundary movement .....	32
Figure 2.14: Calculated intercritical annealing temperature dependence of C and Mn content in austenite using ThermoCalc.....	33

Figure 2.15: a) Austenite vol. fraction as a function of the annealing temperature, b) austenite vol. fraction as a function of the annealing temperature assuming a single austenite grain diameter of 1 $\mu\text{m}$ (full line), and an annealing temperature-dependent austenite grain size (dotted line) .....	34
Figure 2.16: Schematic illustrations of microstructural evolution as function of intercritical annealing temperature: $\alpha$ is ferrite, $\gamma$ is reverted austenite, $\gamma_R$ is retained austenite and $\alpha'_F$ is fresh martensite; A.G.S. is average grain size of reverted austenite, $V_\gamma$ is volume fraction of reverted austenite and $V_{\gamma_R}$ is volume fraction of retained austenite .....	35
Figure 2.17: Austenite fraction as a function of annealing temperature where the lines represent the calculated equilibrium fractions .....	38
Figure 2.18: Variation of volume fractions and C content of retained austenite as a function of tempering temperature .....	41
Figure 2.19: OM micrographs of Fe-9Mn-0.05C steel a) $\alpha'$ martensite and b) prior austenite grain boundaries for hot rolled specimen and c) deformed $\alpha'$ martensite for the cold rolled specimen and d) XRD patterns of hot and cold rolled specimens .....	43
Figure 2.20: Change in critical temperatures as a function of heating rate for a) 5Mn, b) 7Mn and c) 9Mn steel specimens.....	44
Figure 2.21: Effect of cooling rate and carbon content on the retained austenite volume fraction .....	47

Figure 2.22: SEM images of cross section of fractured tensile samples showing preferential sites for void formation and crack propagation (untempered): (a) 1.5 Al (35 pct $\gamma$ ) steel and IBT time = 60s, (b) 1.5 Al (35 pct $\gamma$ ) steel and IBT time = 90s.....	49
Figure 2.23: Fracture mechanism in TRIP-assisted steel showing cracking of martensite. ....	49
Figure 4.1: a) McMaster Galvanizing Simulator (MGS) main column and b) gas mixing system. ....	53
Figure 4.2: Schematic diagram of the McMaster Galvanizing Simulator (MGS).....	54
Figure 4.3: a) Microstructural examination sample coupons and b) panel samples for mechanical property testing, showing corresponding thermocouple positions. ....	55
Figure 4.4: Austenite volume fraction as a function of annealing temperature.....	56
Figure 4.5: C and Mn partitioning in austenite as a function of annealing temperature....	57
Figure 4.6: Ac1 and Ac3 temperatures versus heating rate. ....	58
Figure 4.7: Schematic diagram of the austenitizing heat treatment.....	59
Figure 4.8: SEM micrographs of a) as received S-TM samples with tempered martensite and b) heat treated S-M samples with martensite. ....	59
Figure 4.9: Schematic diagram of the experimental heat treatment. ....	60
Figure 4.10: XRD apparatus with Co K $\alpha$ radiation source. ....	62
Figure 4.11: ASTM E8M- 01 $\epsilon$ 2 tensile specimen dimensions. ....	66

Figure 5.1: Retained austenite volume fraction and C content as a function of intercritical annealing temperature and holding time for S-TM samples.....	68
Figure 5.2: Retained austenite volume fraction and C content as a function of intercritical annealing temperature and holding time for S-M samples. ....	69
Figure 5.3: Martensite volume fraction as a function of holding time at 675°C and 710°C IATs for S-M samples.....	70
Figure 5.4: SEM micrographs of S-TM samples subjected to 675°C IAT for a) 60s, b) 120s, c) 240s, d) 360s, e) 480s and f) 600s. ....	72
Figure 5.5: SEM micrographs of S-TM samples subjected to 710°C IAT for a) 60s, b) 120s, c) 240s, d) 360s, e) 480s and f) 600s. ....	73
Figure 5.6: SEM micrographs of S-M samples subjected to 675°C IAT for a) 60s, b) 120s, c) 240s, d) 360s, e) 480s and f) 600s. ....	74
Figure 5.7: SEM micrographs of S-M samples subjected to 710°C IAT for a) 60s, b) 120s, c) 240s, d) 360s, e) 480s and f) 600s. ....	75
Figure 5.8: Montage of bright field (BF) TEM micrographs at lower magnification for S-M samples annealed at the 675°C IAT for a) 120s, b) 480s and at the 710°C IAT for c) 60s, d) 360s.....	76
Figure 5.9: Bright field TEMs showing different morphologies of ferrite/bainitic ferrite, martensite and retained austenite in S-M 675°C + 600s sample. ....	77

Figure 5.10: Bright field TEMs showing different morphologies of ferrite/bainitic ferrite, martensite and retained austenite in S-M 710°C + 600s sample. ....	78
Figure 5.11: a) Bright field (BF) TEM, b) dark field (DF) TEM corresponding to $\langle 110 \rangle \gamma$ and c) SAD patterns of S-M 675°C + 120s sample. ....	80
Figure 5.12: a) Bright field (BF) TEM; dark field (DF) TEM corresponding to b) $\langle 111 \rangle \alpha$ , c) $\langle 100 \rangle \alpha$ , d) $\langle 110 \rangle \gamma$ and e) SAD patterns of S-M 675°C + 480s sample. ....	81
Figure 5.13: a) Bright field (BF) TEM; dark field (DF) TEM corresponding to b) $\langle 111 \rangle \alpha$ , c) $\langle 100 \rangle \alpha$ , d) $\langle 110 \rangle \gamma$ and e) SAD patterns of S-M 710°C + 360s sample. ....	82
Figure 5.14: SAD pattern (a) and schematic representation of SAD patterns for b) N-W and c) K-S orientation relationship. ....	83
Figure 5.15: Particles and their corresponding SAD patterns of S-M sample annealed at 675°C IAT for 480s. ....	85
Figure 5.16: EDS spectra of the particle and the matrix of the S-M 675°C + 480s sample. ....	85
Figure 5.17: EDS spectra of the particle and the matrix of the S-M 710°C + 360s sample. ....	86
Figure 5.18: EDS spectra of a titanium-rich particle of an S-M 710°C + 600s sample. ....	86
Figure 5.19: Engineering stress vs engineering strain and true stress vs true strain curves for selected as-received and heat treated S-TM and S-M samples. ....	89

Figure 5.20: Summary of S-TM sample engineering stress-strain mechanical properties as a function of 710°C IAT time. ....	90
Figure 5.21: Summary of S-M sample engineering stress-strain mechanical properties as a function of 675°C IAT time. ....	92
Figure 5.22: Work hardening rate vs true strain for selected a) S-TM and b) S-M samples. ....	93
Figure 5.23: Retained austenite transformation kinetics of S-M 675°C IAT samples with 20s OT holding time. ....	95
Figure 5.24: Fracture surface micrographs of a) as received, b) S-TM 710°C + 600s; c) S-M 675°C + 60s and d) S-M 675°C + 120s samples where the microcracks are shown using red circles. ....	96
Figure 5.25: Cross-section near fracture surface of the S-TM 710°C + 600s sample where the microvoids and microcracks are shown in red circles and red arrow, respectively. ....	97
Figure 5.26: Cross-section near fracture surface of the S-M 675°C + 120s sample where microcracks are shown using red circles. ....	97
Figure 5.27: EDS mapping of the area showing decohesion of inclusion in S-M 675°C + 120s sample. ....	98
Figure 5.28: a) Retained austenite volume fraction and b) C content in retained austenite as a function of OT holding time for S-TM samples. ....	100

Figure 5.29: a) Retained austenite and b) C content in retained austenite as a function of OT holding time for S-M samples. ....	101
Figure 5.30: SEM micrographs of S-TM samples subjected to 710°C IAT for a) 60s, b) 120s, c) 240s, d) 360s, e) 480s and f) 600s and 60s OT treatment. ....	103
Figure 5.31: SEM micrographs of S-TM samples subjected to 710°C IAT for a) 60s, b) 120s, c) 240s, d) 360s, e) 480s and f) 600s and 120s OT treatment. ....	104
Figure 5.32: SEM micrographs of S-M samples subjected to 60s OT treatment following 675°C IAT for a) 60s, b) 120s; to 120s OT treatment following 675°C IAT for c) 60s, d) 120s. ....	105
Figure 5.33: Engineering stress vs strain curves as a function of OT holding times for S-TM samples annealed at 710°C IAT for a) 120s, b) 240s and S-M samples annealed at 675°C IAT for c) 60s and d) 120s.....	107
Figure 5.34: Summary of mechanical properties of a) S-TM 710°C + 120s and b) S-TM 710°C + 240s samples as a function of OT holding times.....	108
Figure 5.35: Summary of mechanical properties of a) S-M 675°C + 60s and b) S-M 675°C + 120s samples as a function of OT holding times. ....	109
Figure 5.36: Work hardening rate vs true strain for a) S-TM 710°C + 120s and b) S-TM 710°C + 240s samples as a function of OT holding times.....	111
Figure 5.37: Work hardening rate vs true strain for a) S-M 675°C + 60s and b) S-M 675°C + 120s samples as a function of OT holding time. ....	112

Figure 5.38: Retained austenite transformation kinetics of S-TM 710°C + 240s sample as a function of OT holding times..... 116

Figure 5.39: Retained austenite transformation kinetics of a) S-M 675°C + 60s and b) S-M 675°C + 120s samples as a function of OT holding times..... 117

Figure 5.40: Fracture surface micrographs of S-TM 710°C+ 120s samples with a) 60s OT and b) 120s OT and S-TM 710°C + 240s samples with c) 60s OT and d) 120s OT treatment where the microcracks are shown in red circles. .... 119

Figure 5.41: Cross section near fracture surface of S-TM 710°C + 240s sample with a) 60s OT and b) 120s OT treatment where the microvoids and microcracks are shown using red arrows and red circles, respectively. .... 120

Figure 5.42: Fracture surface micrographs of S-M 675°C + 60s samples with a) 60s OT and b) 120s OT and S-M 675°C + 120s samples with c) 60s OT and d) 120s OT treatment where the microcracks are shown using red circles..... 121

Figure 5.43: Cross-section near fracture surface of S-M 675°C + 120s sample with a) 60s and b) 120s OT treatment where the microcracks are shown using red circles..... 122

## **List of Tables**

Table 4.1 Chemical Composition of the Prototype 3G-AHSS (wt.%) .....	51
Table 4.2 Summary of Heat Treatment Parameters .....	61
Table 4.3 Summary of SEM Parameters.....	64
Table 5.1 Average Particle and Matrix Composition from EDS Spot Analysis (at.%).....	87
Table 5.2 Summary of the Mechanical Properties (Engineering Stress vs Strain) .....	90
Table 5.3 Summary of the Mechanical Properties (Effect of OT Holding Time) .....	114

# 1 INTRODUCTION

## 1.1 Advanced High Strength Steels (AHSSs) in Automotive Industry

Automotive weight reduction is governed by increased fuel efficiency demands from consumers and government legislation to both increase fuel efficiency and reduce greenhouse gas emissions [1] [2]. This has led to the design of thinner cross sections for automotive body parts without compromising passenger safety, which requires materials with a balance of high strength and ductility. Advanced high strength steels (AHSSs) have been meeting these demands since the 1970's [3]. Other materials such as aluminum and magnesium alloys are replacing some steel components in modern automotive designs. However, issues regarding cost and formability for aluminum and the relatively poor mechanical properties and poor corrosion performance for magnesium alloys have limited their applications [4], resulting in the extensive use of different AHSSs in the automotive Body-in-White (BIW), as shown in Figure 1.1.

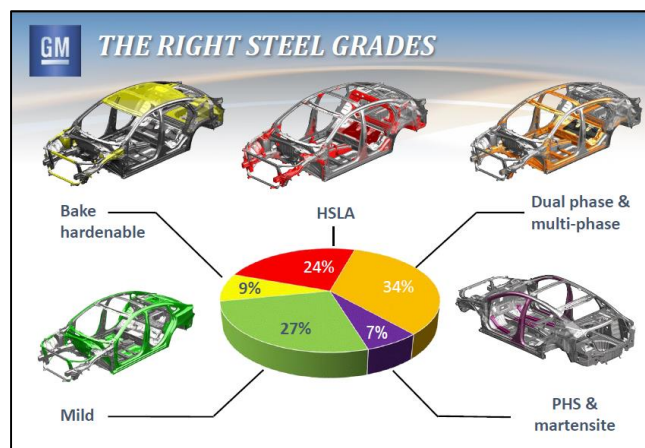


Figure 1.1: A schematic of different steel grades used in the construction of 2016 Chevrolet Malibu and 2017 Buick LaCrosse body-in-white [5].

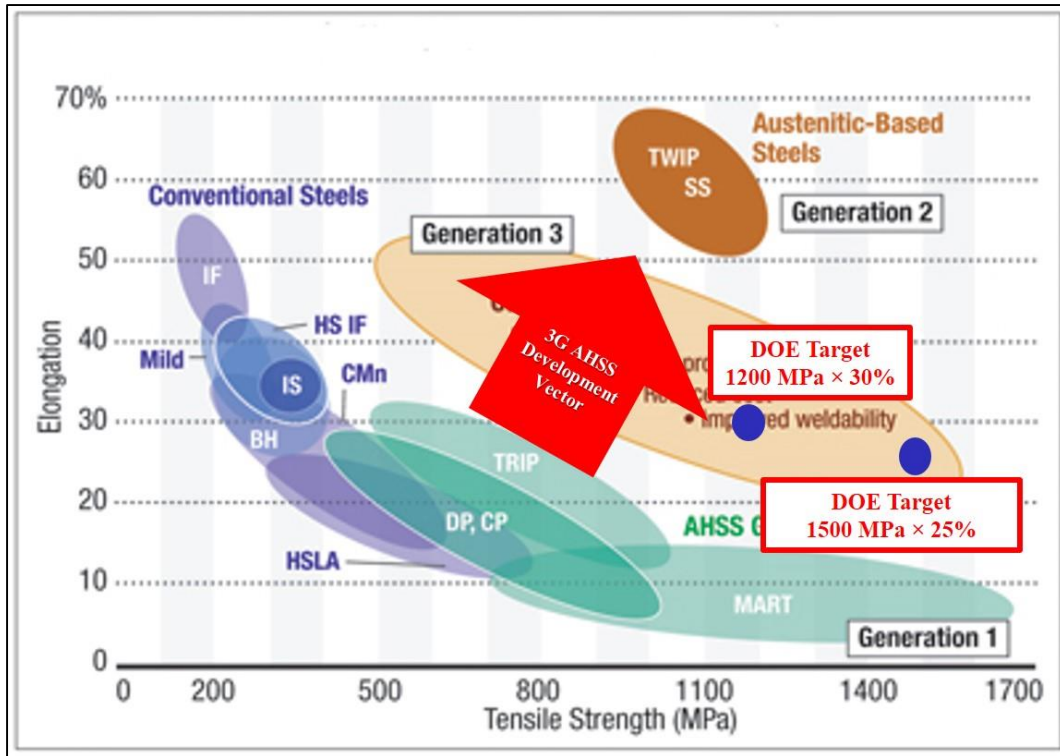


Figure 1.2: AHSS classification and U.S. D.O.E. target mechanical properties for 3G-AHSSs [6] [7].

Constant research to improve the strength/ductility balance of AHSSs has yielded different “generations” of advanced high strength steels. Figure 1.2 shows the different generations of advanced high strength steels with their respective mechanical property ranges in terms of total elongation and tensile strength. Dual phase (DP) steels, transformation induced plasticity (TRIP) steels and martensitic (MART) steels are some of the widely used first generation advanced high strength steels (1G-AHSSs) in modern automotive designs. These steels have a typical ultimate tensile strength  $\times$  total elongation (UTS  $\times$  TE) product of approximately 15,000 MPa% [8]. In particular, low alloy TRIP-assisted steels – which typically contain approximately 2wt.% Mn along with varying levels

of Si and Al –show an exceptional combination of strength and ductility owing to the stress-induced transformation of metastable retained austenite to martensite [9] [10]. In this process, the gradual transformation of metastable retained austenite delays the onset of necking by maintaining a high work hardening rate at higher strains [9]. This results in high strength as well as high ductility in these steels.

Further developments in ferrous physical metallurgy have resulted in the second generation advanced high strength steels (2G-AHSSs) (Figure 1.2). These steels typically contain high percentages of alloying elements compared to their first generation counterparts. Twinning induced plasticity (TWIP) steels are amongst the most widely researched 2G-AHSSs. These steels generally have 22-30 wt.% Mn along with significant C contents (0.4 – 0.6 wt.%) and relatively high concentrations of Al, Si and other alloying elements [11] [12]. Superior strength and ductility combination ( $UTS \times TE > 50,000$  MPa%) have been observed in these steels owing to twinning and transformation induced plasticity effects [13]. However, as these steels are highly alloyed, they are relatively expensive and can be difficult to galvanize due to the formation of external selective oxides of the alloying elements [12].

Significant research is now being focused on developing third generation advanced high strength steels (3G-AHSSs). The development vector for these steels, based on the properties of 1G-AHSSs, is shown in Figure 1.2. These steel grades have lower alloying element concentrations compared to 2G-AHSSs, making their alloying costs significantly less than the 2G-AHSSs. On the other hand, these steels can have a higher strength/ductility balance compared to their first generation counterparts. Target mechanical properties for

these steels have been set by the U.S. Department of Energy (D.O.E.), where the target  $UTS \times TE$  product of these steels is in the range of 36,000 – 37,500 MPa% with specific targets of 1200 MPa  $UTS \times 30\%$  TE and 1500 MPa  $UTS \times 25\%$  TE having been proposed [14].

Medium Mn TRIP steels are amongst the most researched 3G-AHSSs. These steels usually contain 5-10 wt.% Mn along with significant concentrations of alloying elements such as C, Si, Al, Cr, and microalloying elements such as Ti, Nb, V, etc. There are several approaches available to produce the target mechanical properties of 3G-AHSSs in medium Mn TRIP steels. One of the successful approaches is the TRIP/TWIP approach where these steels have exhibited excellent strength/ductility balances, meeting the target mechanical properties of 3G-AHSSs, owing to the presence of significant volume fraction of retained austenite in the microstructure that contributed to the occurrence of the transformation induced plasticity (TRIP) effect [15]. However, recent research [15] [16] [17] with medium Mn steels have found that the retained austenite volume fraction and its stability were sensitive to the intercritical annealing parameters as well as the starting microstructure of the steel substrate. Thus, proper heat treatment plays a critical part in the thermo-mechanical processing of these alloys.

## **1.2 CGL Compatible Thermal Processing Cycle**

All steels require some kind of corrosion protection before they can be used as autobody parts exposed to the external environment. Galvanizing/galvannealing is the most cost effective method that is used in the industry for this purpose. Hence, the continuous galvanizing/galvannealing line (CGL) has become an integral part of the automotive steel

manufacturing industry. Figure 1.3 shows a schematic of a typical radiant tube heated continuous galvanizing/galvannealing line (CGL). At the beginning of this process, the steel coils are welded and cleaned before they enter the radiant tube heating furnace. The steel strip is then heat treated in a controlled reducing atmosphere to reduce any surface FeO and obtain a metallic Fe surface as well as to obtain the desired microstructure and mechanical properties. The steel is then cooled to slightly above the molten Zn bath temperature ( $\sim 460^{\circ}\text{C}$ ) before it enters the molten Zn-Al-Fe bath. The strip then passes through gas-jet wiping upon exiting the Zn bath to control the coating weight or coating thickness. The Zn coating then solidifies by natural convection in the continuous galvanizing process. However, for the continuous galvannealing process, further annealing of the Zn coated steel strip takes place after gas-jet wiping to produce a coating comprising a series of Fe-Zn intermetallics. Finally, the steel sheet is sent to post galvanizing/galvannealing surface treatments and tension leveling followed by inspection and packaging [18].

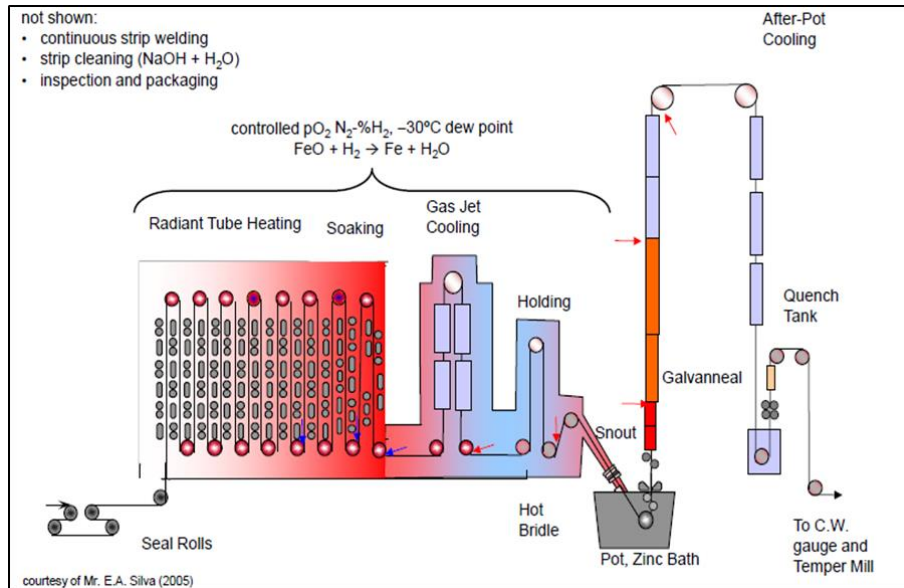


Figure 1.3: Schematic of a continuous galvanizing/galvannealing line [19].

The steel stays a relatively short time, usually 3-5 minutes depending on the line speed, in the radiant tube heating and soaking sections of the CGL for automotive steels. In order to maintain the desired productivity of the CGL, the annealing parameters have to be within these time limits while producing the desired microstructures and mechanical property balance. However, many recent studies [2] [15] [16] regarding the heat treatment of medium Mn steels have been confined to long soaking time, often in terms of hours. As a result, although those heat treatments yielded target strength and ductility balance of 3G-AHSSs, the long holding times render them incompatible with CGL processing windows. Thus, the objective of this research is to develop a CGL compatible thermal processing cycle for a prototype 0.2C-6Mn-1.5Si-0.5Al-0.5Cr (wt.%) medium Mn TRIP-assisted steel that will result in a desired 3G-AHSS microstructure containing high volume fractions of metastable retained austenite and whose mechanical properties are consistent with the target  $36,000 \leq \text{UTS} \times \text{TE} \leq 37,500 \text{ MPa}\%$  property window.

## **2 LITERATURE REVIEW**

### **2.1 Development of Third Generation Advanced High Strength Steels**

Third generation advanced high strength steels (3G-AHSSs) are ideal candidates to meet the automotive light-weighting demands to increase fuel efficiency and meet strict emission legislation requirements. The superior strength and ductility balance of these steels allows thinner cross-section automotive body parts to be designed without compromising passenger safety. U.S. DOE has set one of the target mechanical property ranges for these steels where the  $UTS \times TE$  product has to be in the range of 36,000 – 37,500 MPa% with specific targets being 1200 MPa UTS  $\times$  30% TE and 1500 MPa UTS  $\times$  25% TE [14]. There are several approaches available to produce these target mechanical properties in 3G-AHSSs. One of the successful approaches is the TRIP/TWIP approach based on the mechanical properties of 1G-AHSSs, more specifically low alloy TRIP-assisted steels. Low alloy TRIP-assisted steels exhibit high strength/ductility balance owing to the presence of significant volume fractions of chemically stable retained austenite in the microstructure that results in the occurrence of the transformation induced plasticity (TRIP) effect during deformation [20]. This delays the onset of necking resulting in high total elongation as well as high strength. Hence, the aim of this TRIP/TWIP approach in developing 3G-AHSSs is to produce significant volume fractions of chemically and mechanically stable retained austenite that will transform to martensite during deformation resulting in the desired TRIP/TWIP effect and target mechanical properties for 3G-AHSSs. The development vector based on this approach is marked in Figure 1.1 using a red arrow.

## **2.2 Medium Mn TRIP Steels**

Medium Mn TRIP steels are currently amongst the most researched 3G-AHSSs. Moreover, the TRIP/TWIP approach has also been successful in producing target mechanical properties for 3G-AHSSs in medium Mn TRIP steels [21][22]. These steels usually contain 5-10 wt.% Mn along with 0.1-0.4 C, 0.5-3 Al, 0.5-2 Si (wt.%) and trace amount of microalloying elements (Ti, Mo and V). The amount of C is important in these steels as welding is used extensively for joining the automotive body parts. This type of steel was first studied by Grange and Hribal [23] and then by Miller [24]. Their studies revealed that a 0.1 C - 6 Mn (wt.%), referred to in the recent literature as a so-called medium Mn steel [25][26], yielded martensitic microstructures even when cooled at a very slow rate of 1.7°C/min. Moreover, a tempering heat treatment (640°C for 1 hour) of this steel resulted in an excellent strength/ductility balance (1144 MPa UTS and 30.5% TE) owing to the presence of significant volume fractions of retained austenite in the microstructure that resulted in the transformation induced plasticity (TRIP) effect [24]. The retained austenite in these microstructures arose from the initial martensite via an Austenite Reversion Transformation (ART) reaction, where the intercritical austenite was chemically stabilized due to alloying element partitioning during the tempering treatment and was retained in the final microstructure.

However, recent research [17][25][26] has found that the retained austenite volume fraction and its stability as well as the resultant mechanical properties of medium Mn TRIP steels depended on the annealing parameters and starting microstructures. Moreover, some studies [21][27] with medium Mn steels have revealed that the heat treatment of these steels

produced ultrafine grained microstructure. Localized strain and yield point elongation were observed in these ultrafine grained steels which decreased the mechanical properties considerably. However, this can be avoided by sufficient plasticity enhancing mechanisms such as either the transformation induced plasticity (TRIP) or twinning induced plasticity (TWIP) effect [27]. Hence, proper heat treatment and starting microstructure play a critical part in the thermo-mechanical processing of these alloys.

Moreover, as mentioned in § 1.2, these steels require some kind of corrosion protection before they can be used as autobody parts exposed to the external environment. As a result, the continuous galvanizing/galvannealing line (CGL) has become an integral part of the automotive steel manufacturing industry. A recent study by Alibeigi et al. [28] showed that it is possible to have successful reactive wetting in a medium Mn steel during continuous hot-dip galvanizing. A well-developed Fe-Al intermetallic layer was observed after annealing a Fe-0.071C-5.1Mn-0.086Mo-0.030Si (wt.%) steel at 630°C for 120s and dipping it into a 0.20 wt.% dissolved Al continuous galvanizing bath at 460°C for 10s. However, the mechanical properties of the annealed steel were not determined in their study. Moreover, although many recent studies [16][17][22] reported that the heat treatment of medium Mn TRIP steels produced target strength and ductility balance for 3G-AHSSs, the long holding time at intercritical annealing temperature rendered them incompatible with CGL processing windows. Hence, it is necessary to develop CGL-compatible thermal processing cycles for medium Mn TRIP steels that would ensure both target mechanical properties for 3G-AHSSs and successful reactive wetting in the continuous galvanizing bath.

## **2.3 Strengthening Mechanisms**

TRIP steels have excellent strength and ductility balance owing to various strengthening mechanisms operating depending on the alloy composition and phase constituents in the microstructure. Different strengthening mechanisms include solid solution strengthening, composite strengthening, transformation induced plasticity and twinning induced plasticity effects. These mechanisms will be discussed in the following sections based on previous research on various TRIP-assisted steels.

### ***2.3.1 Solid Solution Strengthening***

TRIP steels usually contain various alloying elements in them in order to obtain the desired microstructure and mechanical properties after heat treatment. Some of these elements such as C, Si, Al and P are added for their solid solution strengthening effect along with some other benefits. These elements have different level of solid solution strengthening effect which is also a function of their concentration in the alloy. Pickering [29] studied the effect of various alloying elements on solid solution strengthening of ferrite and the results are shown in Figure 2.1.

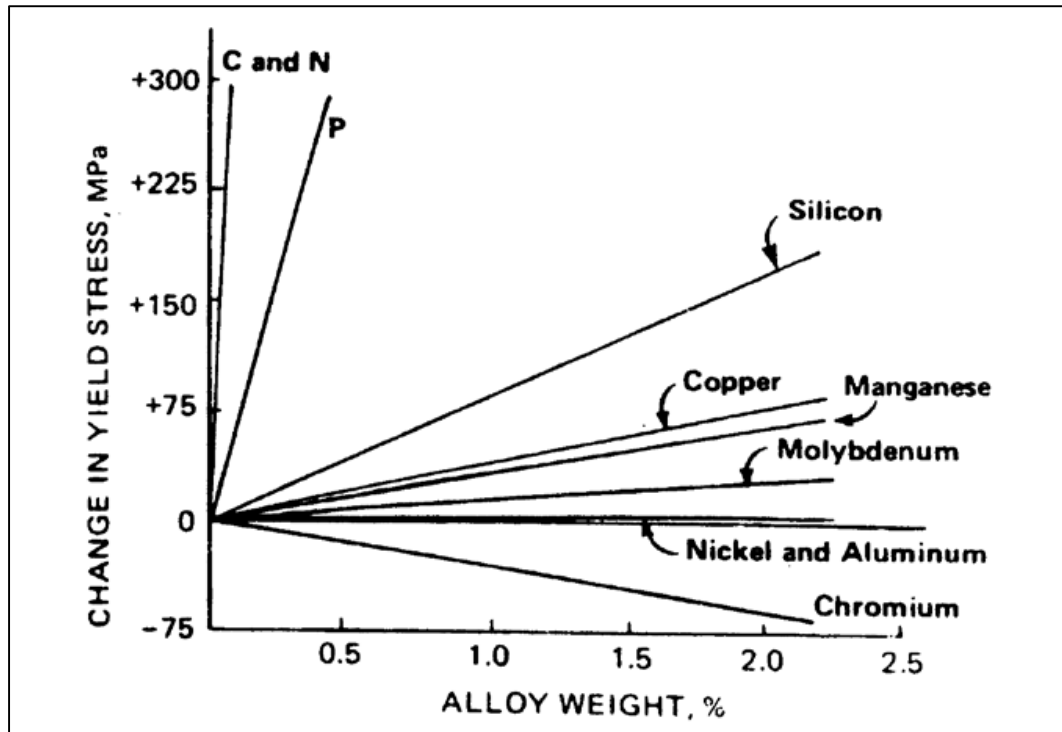


Figure 2.1: Effect of alloying elements on solid solution strengthening of ferrite [29].

It can be seen that C and N have the most pronounced solid solution strengthening effect. However, higher C content in steel can lead to poor weldability which tends to limit its concentration in steels. Si on the other hand, is slightly less effective as solid solution strengthener compared to the former two. Girault et al. [30] has confirmed the effect of solid solution strengthening effect of Si in TRIP-assisted steels. Moreover, Si plays a vital role in delaying carbide precipitation as it has negligible solubility in carbides. So, for carbide formation to take place, Si needs to be rejected from the carbide formation area which requires sufficient time. However, for short holding times at annealing temperatures, Si does not have enough time to diffuse out of the carbide forming area, resulting in significant delay in carbide precipitation. Hence, TRIP-assisted steels usually have some Si in them. However, it also has some demerits in terms of galvanizing. Si produces

detrimental film type oxides during annealing which reduce the wettability of the steels during galvanizing/galvannealing resulting in bare spot defects [31]. Recent research has focused in replacing Si with other elements such as Al or Al and P [32].

### ***2.3.2 Composite Strengthening***

Previous research [1][9][32] has revealed that the heat treatment of conventional low alloy TRIP-assisted steels produces a mixture of different phases such as ferrite, bainitic ferrite, athermal martensite and retained austenite. The harder phases were present as dispersed constituents in the softer ferrite matrix, similar to that observed in composite materials. Moreover, these phases have different yield strengths and hardnesses. Jacques et al. [33] reported the yield strengths of ferrite, bainitic ferrite, austenite and martensite measured by neutron diffraction to be 500, 650, 900 and 2000 MPa, respectively. Furnémont et al. [34] measured the hardnesses of these phase constituents with nanoindentation and the results are shown in Figure 2.2. This difference in hardness and strength of the phases resulted in stress and strain partitioning amongst the phases during deformation. Moreover, Jacques et al. [33] used neutron diffraction to measure the strains of different phases in a TRIP-assisted steel and used them to calculate the corresponding stresses. Jacques et al. [33] also reported that the stress partitioning between ferrite and austenite during deformation was smaller whereas in case of ferrite and martensite, it was much larger. Hence, the stronger phases i.e. martensite and austenite, carried higher stress similar to the case seen in composites and enhanced the overall strength of steel. Moreover, austenite transformed to martensite during deformation which dynamically changed the stress and strain partitioning. This was confirmed by Jacques [9] who calculated the global

stress of a TRIP-assisted steel based on stresses carried on by ferrite and bainitic ferrite (BCC lattice structure) and austenite (FCC lattice structure), measured by neutron diffraction, and by using the law of mixtures

$$\sigma(\varepsilon) = f_{\alpha+\alpha_b}(\varepsilon)\sigma_{\alpha+\alpha_b}(\varepsilon) + f_{\gamma}(\varepsilon)\sigma_{\gamma}(\varepsilon) + f_{\alpha'}(\varepsilon)\sigma_{\alpha'}(\varepsilon) \quad (1)$$

The contribution of martensite was ignored in the calculation. The calculated result was then compared with macroscopic stress measurements (as shown in Figure 2.3) revealing significant difference, marked by the shaded area. This was concluded to be resulting from continuously transformed martensite phase constituents that was ignored in the calculation.

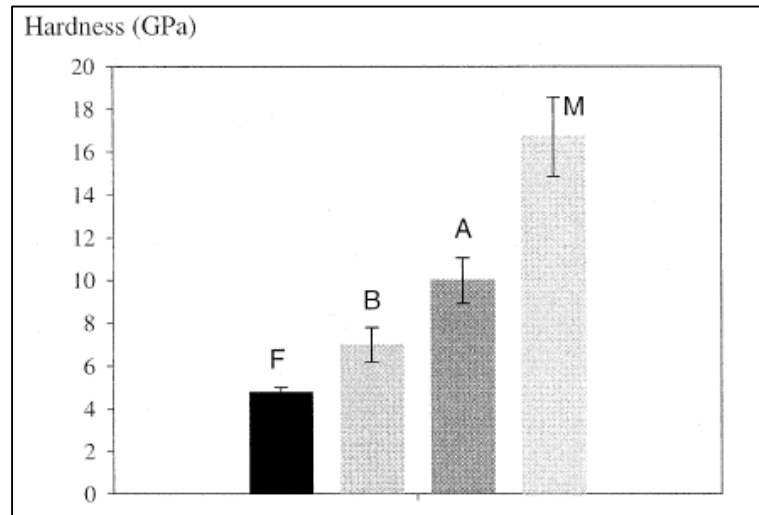


Figure 2.2: Nanohardness results for the different phases in a 0.29% C, 1.42% Mn and 1.41% Si TRIP-assisted steel where F = ferrite, B = bainitic ferrite, A = retained austenite and M = martensite [34].

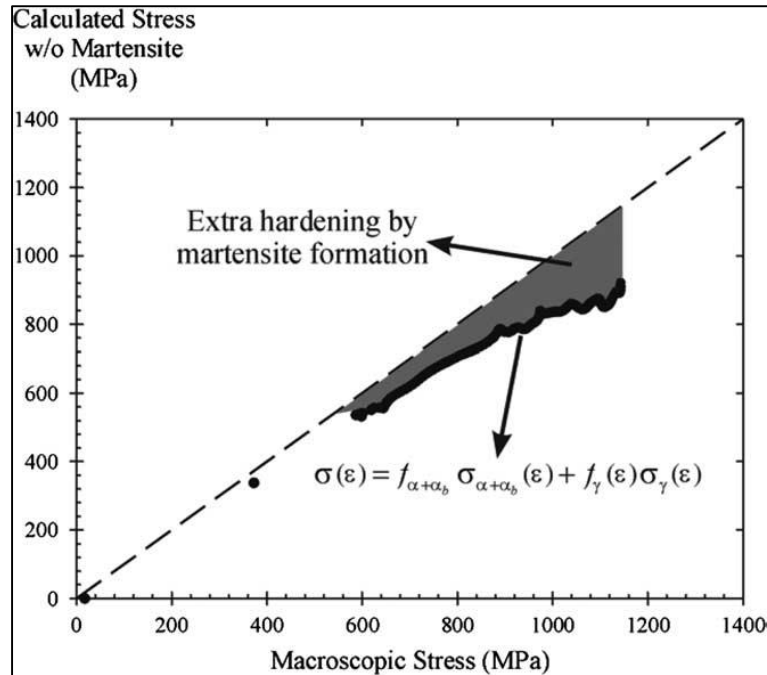


Figure 2.3: Comparison of the macroscopic stress and the stress calculated without taking the martensitic phase into account [9].

Medium Mn TRIP steels also produce ultrafine grained microstructures consisting of different phase constituents after heat treatment [2][22]. Complex microstructure consisting of ferrite, bainitic ferrite, martensite and retained austenite with different morphology have been reported by various researchers studying medium Mn TRIP steels. As a result, the composite strengthening effect would play a vital role in these steels along with other strengthening mechanisms.

De Moor et al. [35] used a simplified composite model to calculate the mechanical properties of martensite/ferrite and martensite/austenite microstructures with varying phase fractions. The authors used the UTS and uniform true strains of ferrite, austenite and martensite as the input parameters for the model. It was found that the property band of the

martensite/austenite mixtures corresponded within the 3G-AHSSs property regime. However, in these cases, the austenite was considered to be fully stable i.e. austenite would not transform to martensite during deformation. So for the next step of the modelling, the authors considered four different austenite stability and found that austenite stability had a significant effect on the predicted mechanical properties, as shown in Figure 2.4. Based on these model calculations, it seems that significant volume fractions (~40%) of austenite with moderate stability can result in target mechanical properties for 3G-AHSSs.

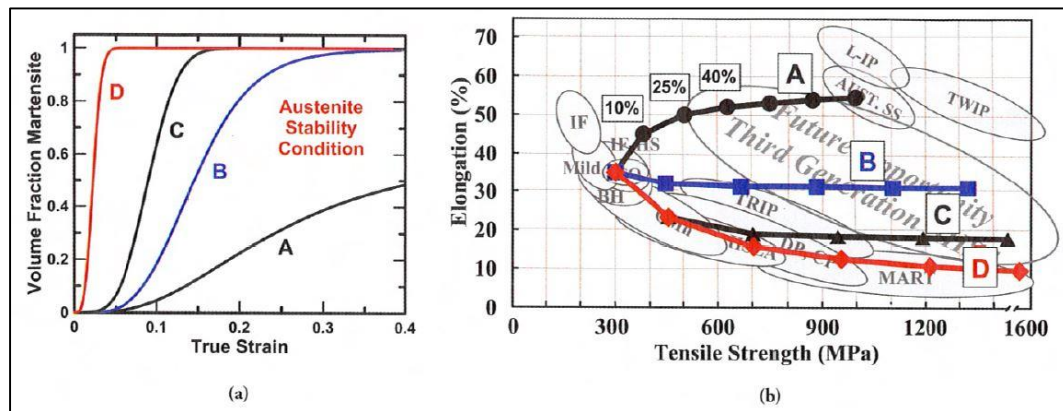


Figure 2.4: Effect of austenite stability on predicted mechanical property combinations: a) four different austenite stability and b) corresponding predicted mechanical property combinations where each data point corresponds to an initial austenite volume fraction [35].

### 2.3.3 TRIP Effect

The transformation induced plasticity (TRIP) effect is observed in steels which have sufficient amount of chemically stable retained austenite. Although Bhadeshia [36] has claimed that the role of the TRIP effect in low alloy TRIP-assisted steels was nothing but an exaggerated explanation and claimed composite strengthening was the main reason

behind their superior mechanical properties, it has been well established since as an important strengthening mechanism in TRIP steels by various researchers [9][10][32]. The chemically stable retained austenite transforms to martensite during deformation and this results in the maintenance of high work hardening rates at high strains. This delays the onset of necking during deformation, resulting in a superior strength-ductility balance. It has been proven that the TRIP effect brings about the high work hardening rate by two mechanisms. One is the formation of harder martensite particles from the retained austenite which provide composite strengthening as discussed in the previous section. Another is the formation of dislocations in the surrounding ferrite due to the volume expansion associated with martensite formation. These dislocations, called “geometrically necessary dislocations”, along with the dislocations in the ferrite grains, improve the local strength of the ferrite grains. Jacques [9] used transmission electron microscopy and confirmed the presence of newly formed “geometrically necessary dislocations” (Figure 2.5).

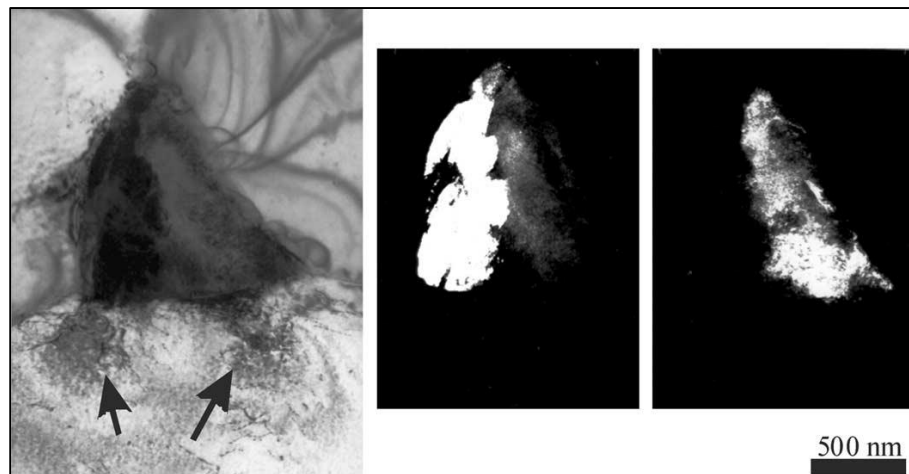


Figure 2.5: BF and DF TEM micrographs illustrating the dislocations generated in the ferrite at the tip of the strain-induced martensitic variants [9].

Jacques et al. [20] also conducted a study and confirmed the relationship between strain-induced retained austenite transformation rate and the strength-ductility balance of various TRIP steels. However, McDermid et al. [10] showed that it is possible to model retained austenite to martensite transformation kinetics of conventional low alloyed TRIP-assisted steels as a function of the normalized flow stress. The authors compared their model with the strain-based model of Olsen and Cohen [37], as shown in Figure 2.6, and suggested that retained austenite to martensite transformation is stress induced for temperatures above  $M_s^\sigma$  (the temperature at which the stress required to initiate martensite transformation equals the yield strength of parent austenite). Moreover, the stress-based model by McDermid et al. [10] was more accurate compared to the strain-based model as the stress-based model was independent of heat treatment parameters, retained austenite chemistry and relative stability of the austenite.

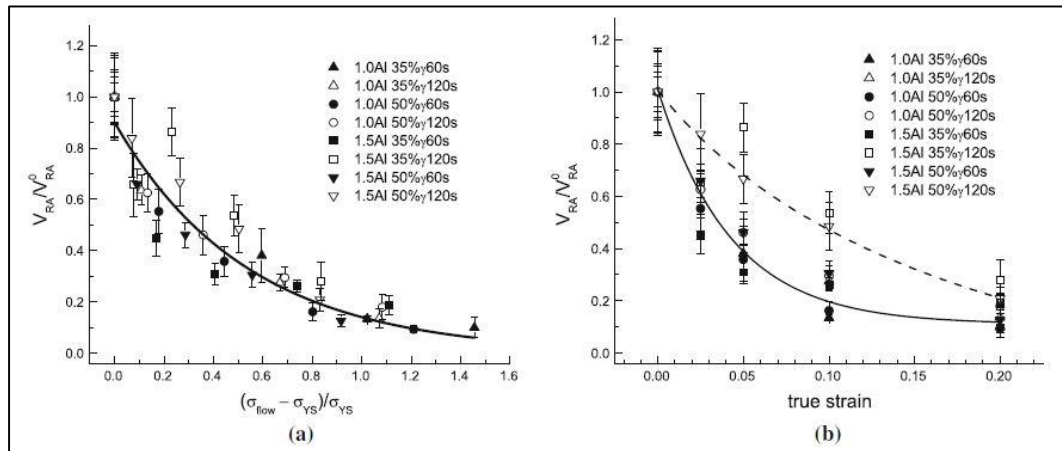


Figure 2.6: Fraction retained austenite vs a) normalized reduced stress and b) true strain

[10].

Lee and De Cooman [16] also proposed a model for selecting intercritical annealing temperatures for a Fe-0.3C-6Mn (mass %) medium Mn TRIP steel which would result in high volume fractions of chemically stable retained austenite. The model was based on the C and Mn content of the intercritical austenite at various intercritical annealing temperatures (600°C - 680°C) as these elements are known to stabilize the intercritical austenite chemically and prevent transformation to martensite during final cooling to room temperature [1][9]. The authors also considered austenite grain size for the model calculation as the austenite grain size significantly influenced the martensite start temperature ( $M_s$ ). This model calculation was also supported by experimental results. It was found that after a specific intercritical annealing temperature (which resulted in highest volume fractions of retained austenite), the retained austenite volume fractions decreased significantly with increasing intercritical annealing temperatures. The authors suggested that the intercritical austenite was no longer chemically stable and transformed to athermal martensite during final cooling to room temperature. Moreover, the tensile test results revealed that the annealed samples with high volume fractions (~0.50) of retained austenite had a high work hardening rate owing to significant TRIP effect which resulted in superior strength and ductility balance.

#### **2.3.4 TWIP Effect**

Medium Mn TRIP steels have another plasticity enhancing mechanism operating beside transformation induced plasticity, depending on the heat treatment parameters and alloy composition, as reported by some recent studies. Lee and De Cooman [38] investigated heat treated 10 wt.% Mn steel and found that some intercritical annealing

conditions resulted in an excellent mechanical property balance. High work hardening rates were observed in those conditions which were further analyzed with TEM to suggest that both the TWIP and TRIP effects worked in succession to result in such work hardening behaviour. Lee et al. [21] studied medium Mn steels with 6 wt.% Mn and varying C content (0.15-0.3 mass %) in order to achieve similar mechanical properties by utilizing more than one plasticity enhancing strengthening mechanisms. The authors selected intercritical annealing temperatures based on one of their previous proposed methods [16] as well as considering the stacking fault energy (SFE) of ultrafine grained austenite ( $> 20 \text{ mJ/m}^2$ ) as shown in Figure 2.7. The tensile properties of these annealed samples were analyzed along with the work hardening rates of these steels compared to some similar medium Mn steels (0.05C-6.15Mn-1.5Si wt.%) [39] (0.08C-6Mn-1.5Si-2Al-0.08V mass %) [40]. The work hardening rate analysis (Figure 2.8) revealed two maxima suggesting more than one plasticity enhancing mechanisms at work. This was further confirmed by TEM analysis which suggested that both the TWIP and TRIP effects operating in succession. The first maxima was from the TWIP effect, which saturated after a certain strain. This was followed by the TRIP effect where  $\alpha'$  martensite nucleated at the twin-twin intersections. Overall this resulted in excellent combination of strength and ductility ( $\sim 34,400 \text{ MPa}\%$ ).

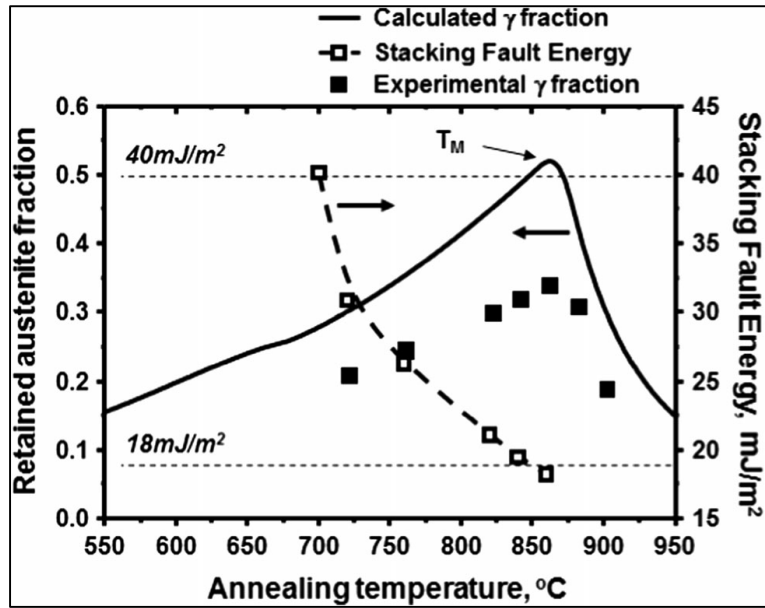


Figure 2.7: Intercritical annealing temperature diagram for a Fe-0.15 pct C-6.0 pct Mn-1.5 pct Si-3.0 pct Al steel [21].

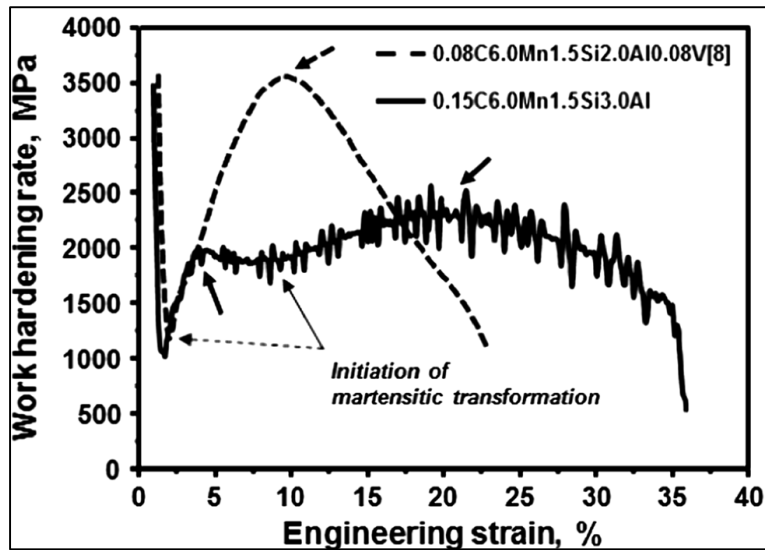


Figure 2.8: Comparison of the work hardening of 0.08 pct C-6 pct Mn-1.5 pct Si-2.0 pct Al-0.08 pct V steel (taken from [40]) and Fe-0.15 pct C-6.0 pct Mn-1.5 pct Si-3.0 pct Al steel [21].

## **2.4 Effect of Starting Microstructure**

The starting microstructure of medium Mn TRIP steels has a profound effect on the amount of retained austenite and resultant mechanical properties. Luo and Dong [22] studied the martensitic starting microstructure and as-received cold rolled microstructure of two different steel grades (0.11wt.%C-4.87wt.%Mn and 0.17wt.%C-4.72wt.%Mn) which were heat treated over a range of intercritical annealing temperatures (650°C - 710°C) followed by oil quenching. There was a distinct difference in the retained austenite volume fractions as well as the corresponding tensile properties of the steels with different starting microstructures (Figure 2.9). For each annealing temperature, the martensitic starting microstructure samples yielded higher volume fractions of retained austenite compared to the cold rolled starting microstructure samples. The morphology of the retained austenite was also different and depended on the starting microstructure. Lamellar shaped retained austenite was observed for the martensitic starting microstructure whereas equiaxed retained austenite was found in the case of the cold rolled starting microstructure samples. Previous research has suggested that the lamellar shaped retained austenite was more stable due to its finer size as it lowers the  $M_s$  temperature [41]. However, Luo and Dong [22] suggested the finer size affected the stability of retained austenite in a different way. TEM analysis confirmed that lath shaped austenite formed at 710°C IAT was retained whereas equiaxed austenite transformed to martensite during cooling. Based on this TEM analysis, the authors suggested more C and Mn accumulated in the retained austenite owing to short diffusion distance in lath shaped austenite grains compared to their equiaxed or blocky

counterparts. This increased the chemical stability of the lath shaped retained austenite resulting in their higher amount in the final microstructure.

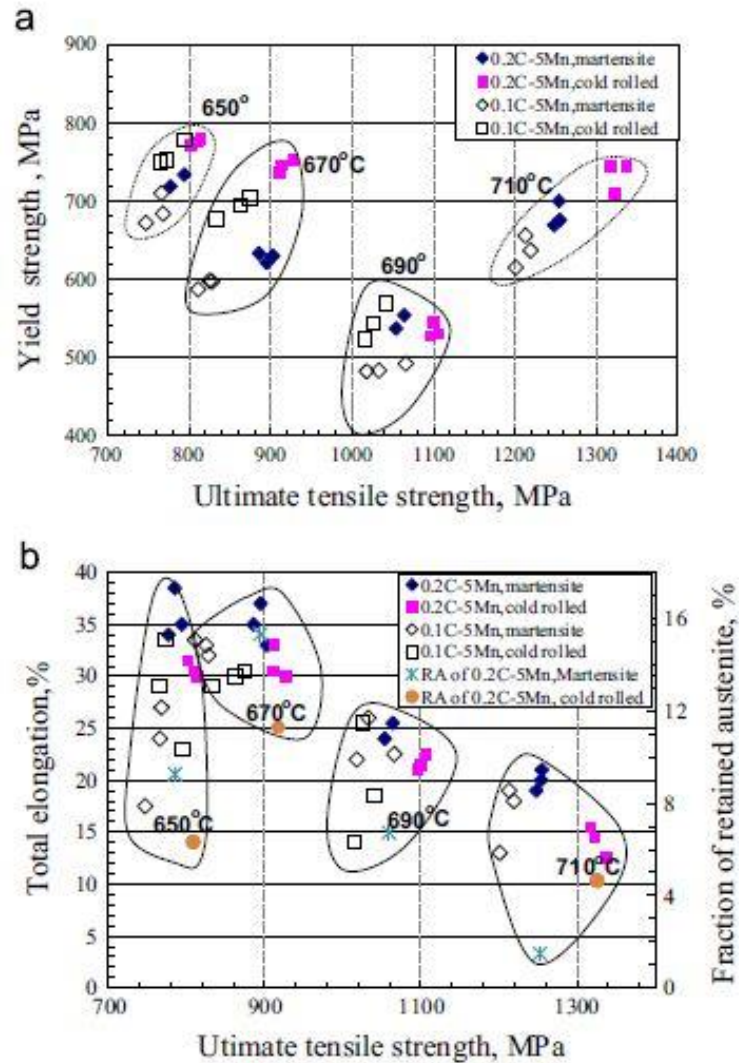


Figure 2.9: Dependence of tensile properties and retained austenite amount on starting microstructure, annealing temperature and carbon content of the steels [22].

Arlazarov et al. [2] studied the effect of martensitic treatment (prior to intercritical annealing) on the final microstructure and mechanical properties of a medium Mn steel (0.092C-4.6Mn wt.%). The medium Mn steel was subjected to an austenitizing heat

treatment for 30 min followed by water quenching. This resulted in a martensitic microstructure with a small volume fractions of retained austenite. The steel was then annealed at an intercritical temperature of 670°C for 1 hour to 30 hours. Although the soaking times were very long in terms of continuous galvanizing line (CGL), this study explained the different morphology of the phases observed as well as a detailed examination of Mn microsegregation via EPMA analysis.

Both lath and polygonal morphologies were observed in ferrite and retained austenite after intercritical annealing, however, the lath morphology decreased as the holding time at intercritical temperature increased. In order to discuss this behaviour, the authors first explained the classical theory of austenite formation from a martensitic steel without any deformation. It was suggested that martensite without any deformation did not have sufficient energy for ferrite recrystallization although martensite has a high dislocation density. During annealing, austenite tends to nucleate at the lath boundaries which afterwards grow. The growth rate is controlled by C diffusion. This results in lath like retained austenite with some non-polygonal ferrite [2]. However, as the annealing treatments were long in their study, Mn was also able to diffuse. The EPMA results (Figure 2.10) showed that martensite and austenite grains were rich in Mn whereas the ferrite grains were low in Mn. The authors suggested that the Mn rich and the Mn depleted areas in the microstructure had different transformation mechanisms. Austenite started to transform at a lower temperature preceding ferrite recrystallization. As a result, the dislocation density decreased which lowered the driving force for recrystallization meaning the absence of polygonal morphology in ferrite. In the Mn depleted zones, the austenite transformation

started at a higher temperature. The recovery and recrystallization process was hence less effected by the transformation and started almost at the same time as the austenite transformation. This resulted in the recrystallized equiaxed ferrite grains in the final microstructure.

The authors also concluded that the austenite stability depended not only on the C content in it but also on the grain size. It was calculated that for a  $M_s$  of  $0^\circ\text{C}$ , the grain size has to be below  $1.9\ \mu\text{m}$ . In their study the 7 hour annealing resulted in retained austenite of less than  $1\ \mu\text{m}$ . This suggested that apart from chemical enrichment of C, grain size also played a vital role in stabilizing the retained austenite.

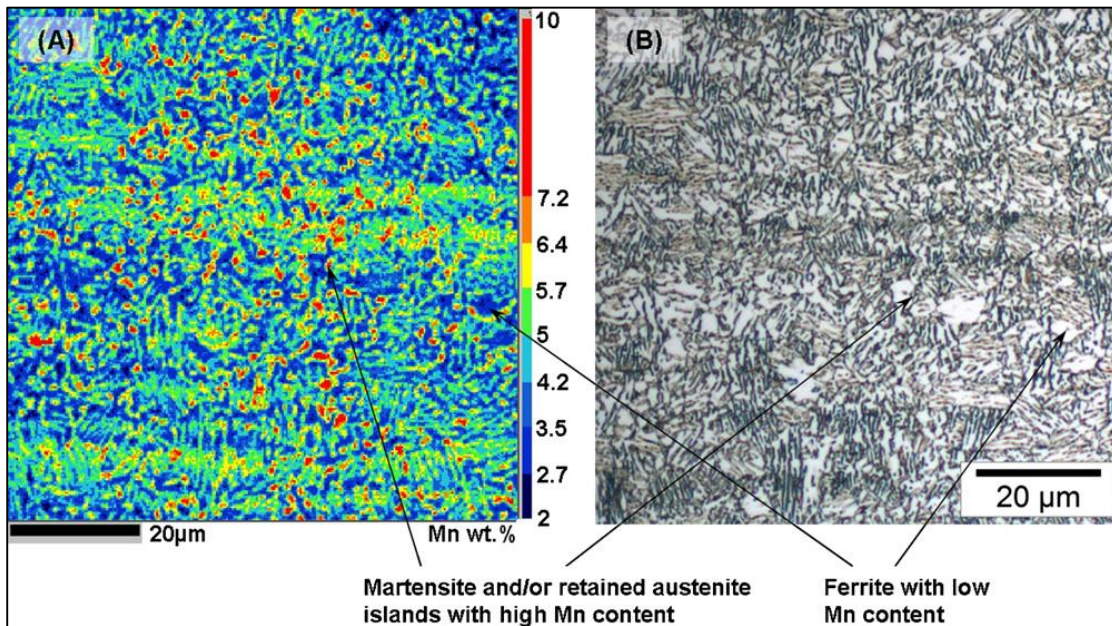


Figure 2.10: Comparison of EPMA Mn map (A) with the microstructure after Dino etching observed in OM (B) for the sample after second annealing at  $670^\circ\text{C}$  for 7 hr [2].

## **2.5 Austenite Reversion Transformation (ART)**

Intercritical annealing of martensitic steels results in an austenite reversion transformation (ART) for both conventional low alloy TRIP steels [42] and medium Mn TRIP steels [15]. Hence, the growth of austenite from martensite during intercritical annealing has been studied by various researchers with different steel grades to achieve superior mechanical properties via the TRIP mechanism [15][17]. For example, Nakada et al. [17] reported that the martensite to austenite transformation kinetics were faster compared to austenite to ferrite transformation kinetics in a medium Mn steel (0.1C-5Mn wt.%). Moreover, the retained austenite was mostly observed as fine austenite films along the martensite lath boundaries. It was concluded that the retained austenite was chemically stable owing to C and Mn partitioning during annealing at 909K for 50 hours. Based on DICTRA simulation, it was also confirmed that Mn diffusivity was higher in martensite matrix compared to austenite matrix, resulting in higher volume fractions of chemically stable retained austenite.

Moreover, Nakada et al. [43] investigated austenite nucleation behaviour from martensite laths in a martensitic stainless steel (Fe-13Cr-6Ni-0.012C-2.1Mo mass%) at various intercritical temperatures (873 K, 913 K and 953 K). Austenite reversion occurred during these intercritical annealing treatments. However, the morphology and the distribution of the austenite grains varied with the annealing temperature. Acicular austenite grains were observed at the lower intercritical temperatures (873 K and 913 K) which formed at the martensite lath boundaries. On the other hand, at high intercritical annealing temperature (953 K) granular austenite grains were observed at prior austenite

grain boundaries (PAGBs), as shown in Figure 2.11. Based on the classical nucleation theory and calculating the interfacial energy change and strain energy change for austenite nucleation at martensite lath boundary and PAGB, it was concluded that martensite lath boundaries were preferential nucleation sites at lower temperatures.

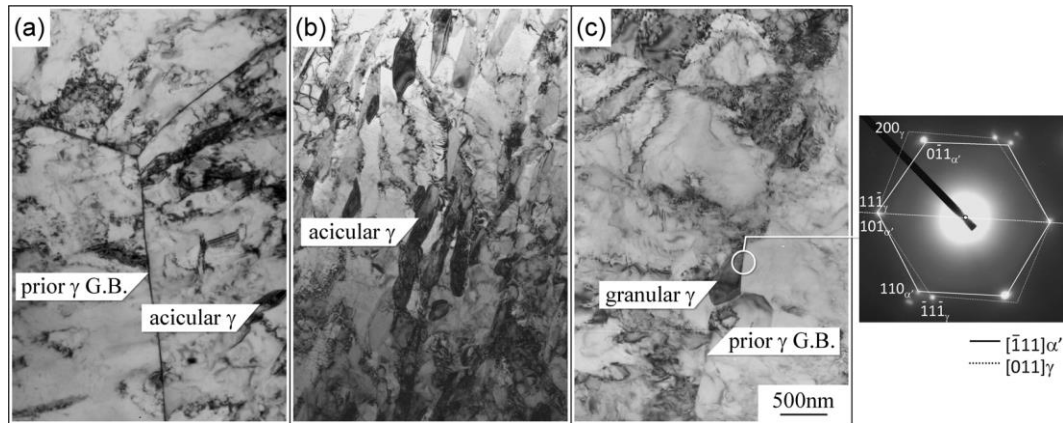


Figure 2.11: TEM micrographs showing morphology and distribution of austenite grains in the specimens reversion-treated at a) 873 K for 10.8 ks, b) 913 K for 1.8 ks and c) 953 K for 0.18 ks [43].

Moreover, previous research [42] has revealed that the formation and growth of austenite during intercritical annealing depends on the initial microstructure as well as the alloying elements. Miyamoto et al. [42] studied the effect of substitutional alloying element (Si, Mn and Cr) addition on the austenite reverse transformation kinetics in a Fe-0.6C (wt.%) alloy. The austenite reverse transformation (ART) annealing was conducted at 1073K for 3-100s (for 1 wt.% Si and 1-2 wt.% Mn addition) and for 10,000s (for 1-2 wt.% Cr addition). The authors reported that C activity gradient decreased with increasing alloying of substitutional elements. Moreover, as the growth of the reverted austenite was controlled by C diffusion, the austenite reverse transformation kinetics retarded with

increasing amount of Si, Mn and Cr. This retarding effect was greater in the alloy that had higher amount (1-2 wt.%) of Cr. STEM/EDS analysis also revealed that the austenite/cementite interface was found to be migrating without Mn partitioning during austenite growth as the austenite formed surrounding the cementite particle which had high Mn content. On the other hand, the austenite/cementite interface migrated along with Cr partitioning. This resulted in severe retardation in austenite reverse transformation kinetics as long range diffusion of Cr was necessary for that alloy system.

Wei et al. [44] studied the growth of austenite during intercritical annealing in an as-quenched martensitic Fe-0.1C-3Mn-1.5Si (mass %) alloy, with higher Mn content (~3 wt.% Mn) compared to conventional low alloy TRIP-assisted steels. Fine film-like austenite grains formed at the lath and martensite packet boundaries during intercritical annealing. Dilatometric analysis at different intercritical annealing temperatures (690°C, 720°C and 760°C) which showed strain contraction related to austenite formation, revealed that thin films of retained austenite might have started to grow without a nucleation barrier at martensite lath boundaries. Moreover, it was also reported that the martensite lath width limited the austenite grain size.

Wei et al. [44] also used DICTRA simulations to identify the growth mechanism of the austenite, as shown in Figure 2.12. It was concluded that the growth of the austenite grains consisted of three distinct stages. Initially, the growth was controlled by rapid C diffusion in ferrite followed by C diffusion in austenite. The intermediate slow growth stage, on the other hand, was controlled by diffusion of the substitutional elements (Mn and Si) in ferrite. The final stage was characterized by very slow growth which was controlled

by the diffusion of the substitutional elements (Mn and Si) in austenite. Moreover, excess austenite volume fraction was observed compared to calculated equilibrium amount which was linked to the slow diffusion of the substitutional elements in austenite relative to the grain boundary migration. This suggested that the retained austenite growth was controlled by solute drag effect which depended on the diffusivity ratio of the alloying elements in the parent and growing phases, intercritical annealing temperature and steel composition.

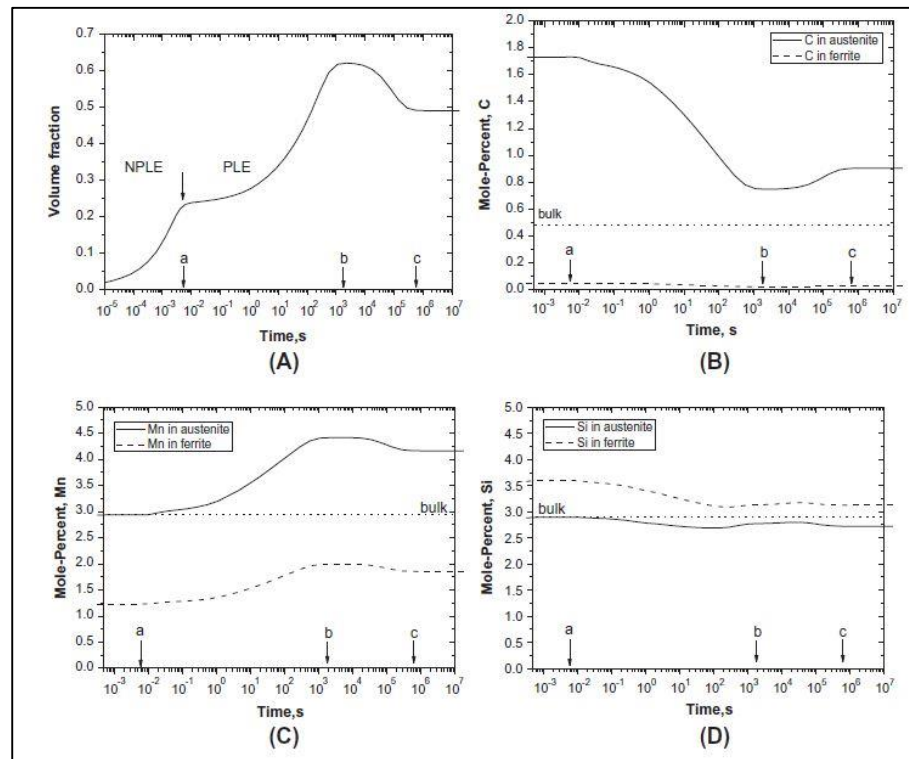


Figure 2.12: Variations of a) volume fraction of austenite, b) C concentration at the boundary in austenite (solid curve) and ferrite (dashed curve), c) Mn concentration and d) Si concentration during holding at 760°C [44].

Cao et al. [15] reported an excellent strength and ductility combination (~1000 MPa UTS and > 40% TE) for a medium Mn steel (Fe-0.2C-5Mn wt.%) which was processed by

ART annealing at 650°C for 6 hours. These mechanical properties were linked to a high austenite volume fraction (~34%) that reverted from the martensitic starting microstructure of the steel during the intercritical annealing stage. The annealing treatment resulted in ultrafine grained retained austenite and ferrite, with increasing holding time at the intercritical temperature resulting in coarser grains. The retained austenite transformed to martensite during deformation which delayed the onset of necking and resulted in high uniform elongation along with high strength.

Han et al. [45] studied the effect of martensitic starting microstructure of both hot rolled (HR) and cold rolled (CR) medium Mn steel (Fe-9Mn-0.05C wt.%) on the retained austenite volume fraction and its morphology. Both HR and CR steels were intercritically annealed at 620°C for 600s. The authors reported higher volume fractions (~37%) of retained austenite in CR steel samples compared to HR steel samples (~30%). It was concluded that the deformation by cold rolling has accelerated the austenite reversion transformation (ART) during intercritical annealing. Moreover, the morphologies of the retained austenite and ferrite were also different in those intercritically annealed HR and CR steel samples. The retained austenite and ferrite had globular morphology in the annealed CR steel samples whereas lamellar shaped retained austenite and ferrite were observed in annealed HR steel samples. Both annealed HR and CR steel samples had superior strength and ductility combination ( $UTS \times TE > 29,000 \text{ MPa}\%$ ). However, significant yield point elongation was observed in annealed CR steel samples. Total elongation also decreased in annealed CR steel samples (~25%) compared to annealed HR steel samples (~27%). It was suggested that the globular ferrite with low dislocation

densities, owing to active recovery, deformed prior to retained austenite to martensite transformation and resulted in the significant yield point elongation.

Shi et al. [46] studied the mechanical properties and work hardening behaviour of four different medium Mn steels (0.2C-5Mn, 0.26C-5Mn, 0.4C-5Mn and 0.2C-7Mn wt.%) with martensitic starting microstructure which were annealed at 650°C for 6 hours. High volume fractions (>30%) of retained austenite formed by austenite reversion transformation (ART) was observed in all four annealed steel grades. Moreover, tensile tests revealed excellent combination of strength and ductility balance ( $UTS \times TE > 38,000 \text{ MPa\%}$ ) in those annealed samples, with the highest  $UTS \times TE$  product (44,000 MPa%) being reported for the annealed 0.2C-7Mn (wt.%) medium Mn steel. It was concluded that the high volume fractions of ultrafine lath-shaped retained austenite which was mechanically stable, was the main reason behind such excellent mechanical properties. The mechanically stable retained austenite transformed gradually to martensite during deformation, resulting in maintaining high work hardening rate at high tensile strains. As a result, the onset of necking was delayed during deformation which resulted in high strength and ductility combination.

## **2.6 Effect of Intercritical Annealing Parameters**

Intercritical annealing is one of the most crucial steps of the thermal processing cycle in CGL. Proper intercritical annealing temperature and holding time at that temperature play an important role in determining the final retained austenite content and its morphology after the heat treatment cycle. The main goal in this stage is to have as much stable intercritical austenite as possible and try to prevent any premature transformation of austenite to martensite during the subsequent cooling stages.

The De Cooman [32] models showed that initially the C content of the intercritical austenite was higher than the equilibrium value. However, it reached the equilibrium within a short amount of time. The substitutional alloying elements Mn and Si diffused more sluggishly compared to C, and as a result these elements did not reach their equilibrium value within the time frame usually used in industry, especially in the continuous galvanizing line (CGL). The DICTRA simulation results shown in Figure 2.13 summarizes these findings which suggested that the intercritical austenite formation was mainly controlled by the diffusion of C.

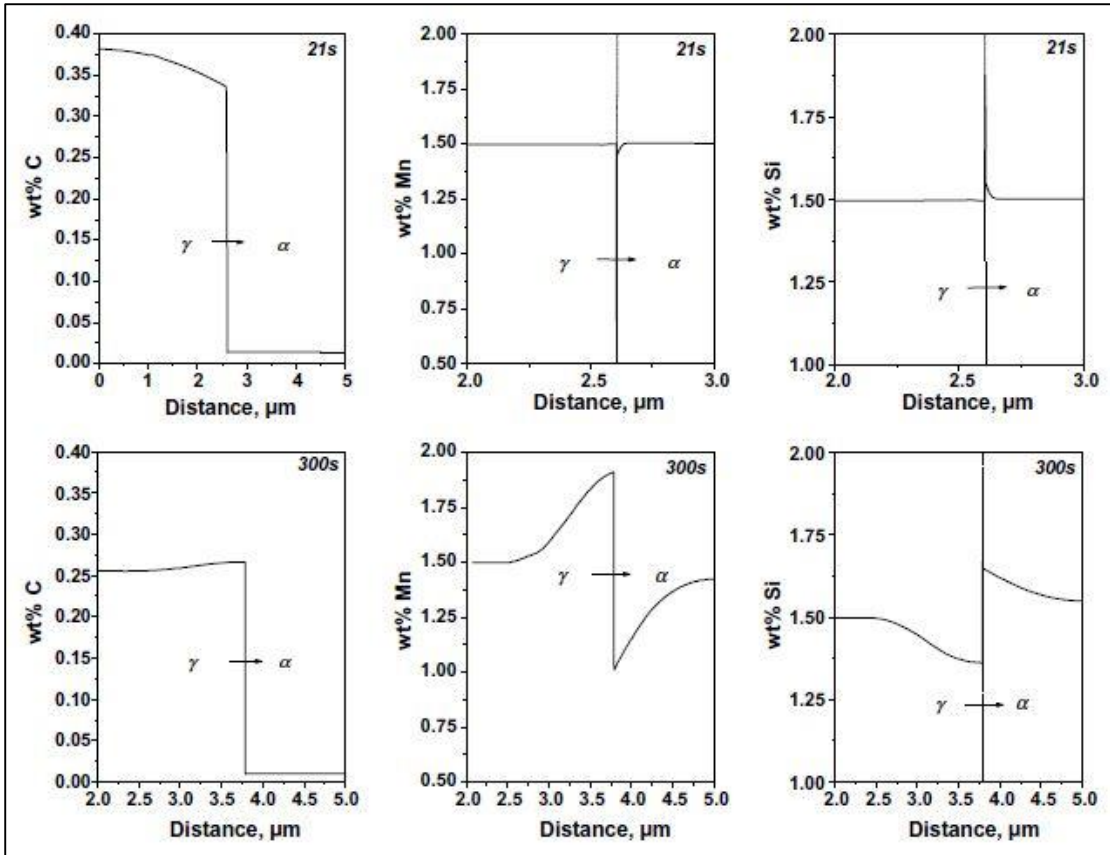


Figure 2.13: DICTRA calculation of C, Mn and Si profile across the ferrite-austenite phase boundary at different times during intercritical annealing; the arrow indicating the direction of the phase boundary movement [32].

Lee and De Cooman [16] proposed a model to predict the optimal intercritical annealing temperature for a 0.3C-6Mn (wt.%) steel to yield the highest volume fractions of stable retained austenite. They used ThermoCalc software to calculate the C and Mn content in intercritical austenite as a function of annealing temperature. However, it should be noted that the model was based on equilibrium conditions whereas the steel substrate only resides 3-5 minutes in an industrial CGL which is not enough to reach equilibrium conditions. The optimum intercritical annealing temperature was selected based on those

results (Figure 2.14). As previous studies [1][9][32][47] suggested that the austenite stability depended significantly on its C content, the annealing temperature that yielded highest C partitioning in the austenite resulted in the highest amount of stable retained austenite in the final microstructure.

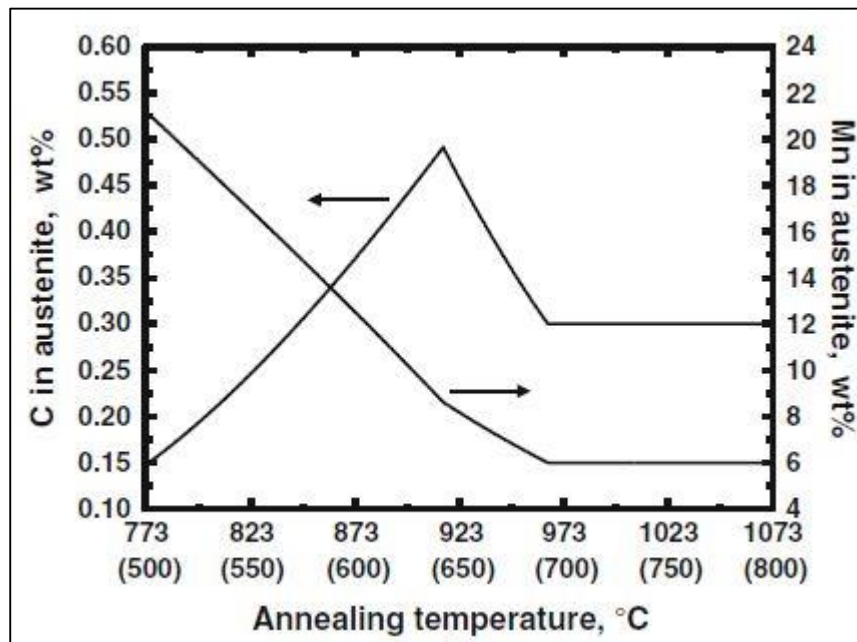
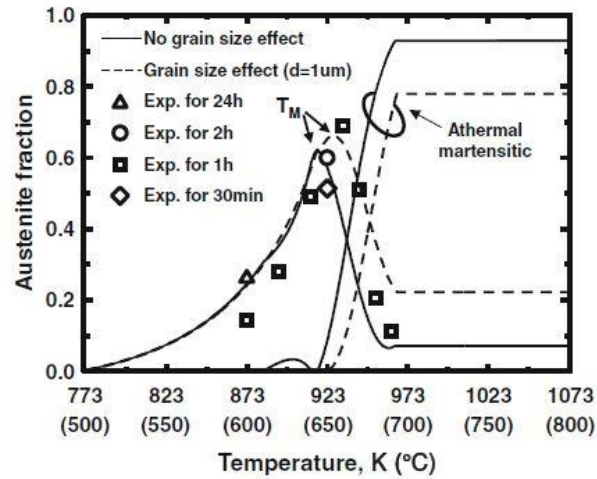


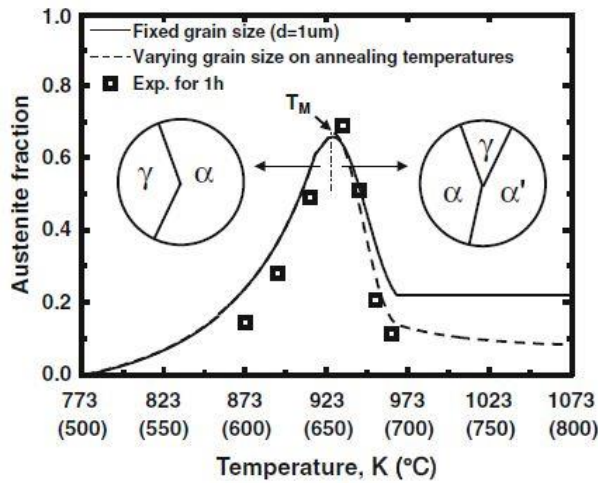
Figure 2.14: Calculated intercritical annealing temperature dependence of C and Mn content in austenite using ThermoCalc [16].

The steel substrate was annealed at different temperatures for various holding times and the experimental results were compared to the calculated results. After incorporating the grain size effect, the results were comparable (Figure 2.15). The retained austenite amount increased with annealing temperature supporting the hypothesis that the increased C partitioning with increased temperature stabilized more intercritical austenite. However, the retained austenite fraction started to decrease after 650°C IAT and the fraction of undesired athermal martensite increased. This suggested that the C content in the

intercritical austenite was not sufficient enough to stabilize it and prevent it from transforming to martensite during cooling.



a)



b)

Figure 2.15: a) Austenite vol. fraction as a function of the annealing temperature, b) austenite vol. fraction as a function of the annealing temperature assuming a single austenite grain diameter of 1  $\mu\text{m}$  (full line), and an annealing temperature-dependent austenite grain size (dotted line) [16].

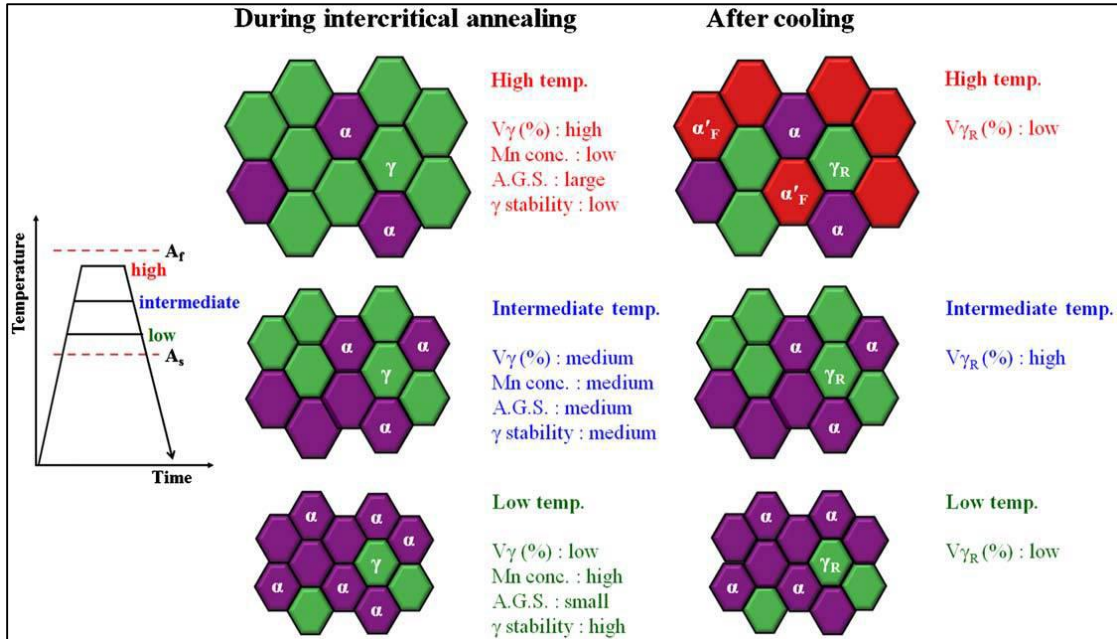


Figure 2.16: Schematic illustrations of microstructural evolution as function of intercritical annealing temperature:  $\alpha$  is ferrite,  $\gamma$  is reverted austenite,  $\gamma_R$  is retained austenite and  $\alpha'_F$  is fresh martensite; A.G.S. is average grain size of reverted austenite,  $V_\gamma$  is volume fraction of reverted austenite and  $V_{\gamma_R}$  is volume fraction of retained austenite [48].

A schematic illustration of the effect of intercritical annealing temperature on the microstructure and volume fraction of retained austenite is shown in Figure 2.16. It summarizes the fact that with increasing temperature more reverted austenite forms during intercritical annealing, however, high temperature also increases the grain size of the intercritical austenite. Luo [49] explained that grain growth of intercritical austenite resulted in lower mechanical stability of the austenite. The C content did not change much as it was already at equilibrium. However, the gradual loss of mechanical stability of growing the retained austenite was due to decreasing hydrostatic pressure from the

surrounding phases. This resulted in significant decrease in mechanical stability of the retained austenite as hydrostatic pressure hinders the austenite to martensite transformation. Mechanical stability of the retained austenite depended on the energy required to accommodate the austenite to martensite transformation strain. In case of larger retained austenite grains, less energy was required to generate dislocations which accommodated the transformation strains, resulting in significant decrease in mechanical stability of the retained austenite. Moreover, research [22] also suggested that grain refinement tends to improve the mechanical stability of the reverted austenite and lower the martensite start temperature ( $M_s$ ). The authors concluded that the higher hydrostatic pressure from the surrounding ultrafine phases increased the mechanical stability of the retained austenite. As a result, gradual transformation of retained austenite to martensite was observed which resulted in superior strength and ductility combination, with 31,000 MPa% UTS  $\times$  TE product being reported for a 0.2C-5Mn (wt.%) steel with martensitic starting microstructure that was annealed at 670°C for 10 minutes (Figure 2.9).

Gibbs et al. [25] investigated a Fe-7Mn-0.1C (wt.%) steel that was annealed at 600°C and 650°C for 168 hours. In situ neutron diffraction technique was used in order to study the change in mechanical properties based on strain partitioning in different phases. The authors reported a high UTS (1200 MPa) along with low total elongation (10%) for the steel samples annealed at 650°C for 168 hours. It was concluded that yielding in these annealed samples was controlled by stress induced austenite to martensite transformation. Moreover, this transformation was rapid and resulted in a high initial work hardening rate. However, as most of the retained austenite transformed at low strain, even before plastic

deformation of ferrite could begin, low work hardening rate at high strain was observed. This resulted in a high UTS with low total elongation. On the other hand, the samples annealed at 600°C for 168 hours, showed significant increase in total elongation (~41.5%) with a slight decrease in UTS (~870 MPa) compared to samples annealed at 650°C. In these annealed samples, the yielding was first controlled by localized plastic deformation of the strain aged recrystallized ferrite. This resulted in significant yield point elongation. After that, both austenite and ferrite deformed plastically and homogeneously. Moreover, gradual transformation of austenite to martensite was also observed in these samples which resulted in maintaining high work hardening rate at high strains. As a result, high strength as well as high total elongation was observed in these medium Mn TRIP steels annealed at 600°C for 168 hours.

Suh et al. [26] studied three different grades of medium Mn steels (Fe-0.11C-4.5Mn-0.45Si-2.2Al, Fe-0.075C-5.1Mn-0.49Si-2.1Al and Fe-0.055C-5.6Mn-0.49Si-2.2Al wt.%) which were annealed at 700°C - 780°C for 120s. High Al content (>2 wt.%) was used in order to reduce the holding time at intercritical annealing temperature owing to the fact that Al increases the  $Ac_1$  and  $Ac_3$  temperatures (i.e. intercritical annealing temperature range) where diffusion of solute is rapid compared to that in lower temperatures. The authors reported that the retained austenite volume fraction increased with increasing annealing temperature up to 760°C, followed by a significant decrease in retained austenite volume fraction at 780°C, as shown in Figure 2.17. It was suggested that the intercritical austenite transformed to martensite owing to less chemical stability (dilution of C and Mn content in larger grains) as well as mechanical stability (larger grain size reduced hydrostatic pressure

from surrounding phases). However, highest total elongation (~30%) was observed for samples annealed at 720°C suggesting that stability of the retained austenite also played a vital role along with retained austenite volume fraction in determining the mechanical properties of these annealed medium Mn steels. Moreover, significant yield point elongation was observed in all annealed samples. It was suggested that high Al content resulted in significant volume fractions of recrystallized coarse ferrite grains which deformed plastically prior to austenite to martensite transformation, resulting in significant yield point elongation.

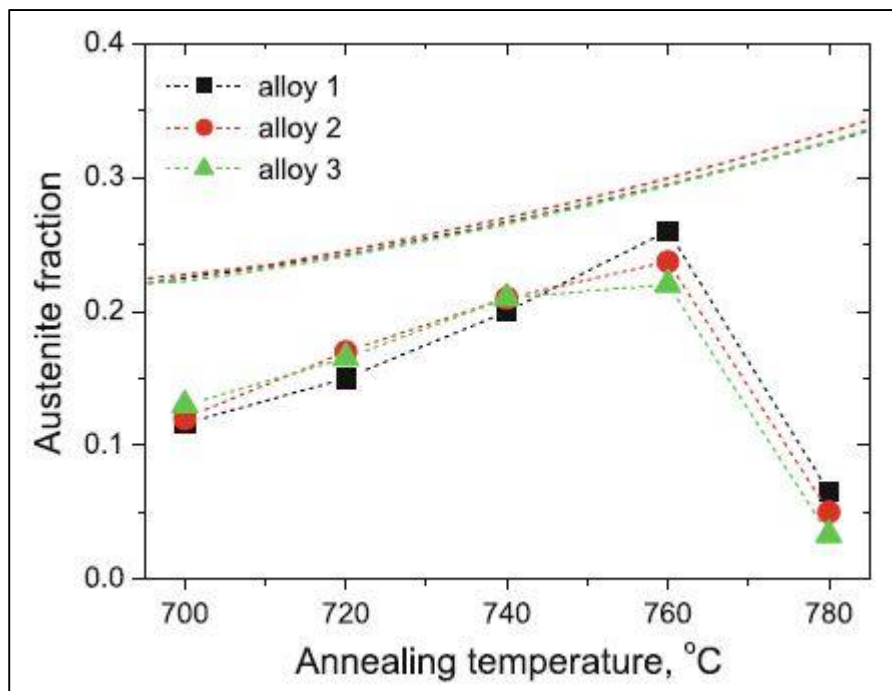


Figure 2.17: Austenite fraction as a function of annealing temperature where the lines represent the calculated equilibrium fractions [26].

## **2.7 Effect of Overaging Temperature (OT) Treatment Parameters**

Another important isothermal holding stage in continuous galvanizing line (CGL) is the overaging temperature (OT) treatment stage. The annealed steel substrate is cooled to an overaging temperature (OT) and held there for a certain amount of time in order to achieve thermal equilibration prior to dipping in the zinc bath (Figure 1.3). However, this isothermal hold also affects the final microstructure, more importantly the volume fractions and the stability of the retained austenite. Hence, it is necessary to determine the effect of overaging temperature (OT) treatment parameters on the microstructural evolution and the mechanical properties of the annealed steels.

This crucial stage is used in conventional low alloy TRIP-assisted steels to stabilize the austenite further more by transforming some of it to carbide free bainitic ferrite [1][32]. Bainitic ferrite transformation results in rejection of C from bainitic ferrite and these C diffuse into the remaining austenite owing to the alloying elements such as Si and Al which delay carbide precipitation. As a result, the remaining austenite become more chemically stable during the final cooling to room temperature and yield high volume fractions of retained austenite.

Overaging temperature (OT) has a completely different effect on medium Mn steels compared to that observed in conventional low alloy TRIP-assisted steels [1]. Xu et al. [50] studied the effect of tempering temperatures (100°C - 600°C) on the stability of retained austenite in a 0.2C-5Mn (wt.%) medium Mn steel with martensitic starting microstructure. The 0.2C-5Mn (wt.%) steel was first annealed at 675°C for 30 minutes followed by oil quenching, resulting in a martensitic microstructure. Afterwards, it was subjected to an

ART-annealing treatment at 650°C for 6 hours. This resulted in ultrafine microstructure consisting of lamellar austenite, ferrite and some cementite precipitates. The ART-annealed steel samples were then tempered at different temperatures (100°C-600°C) for 1 hour followed by air cooling to room temperature. The authors reported that retained austenite volume fractions initially decreased with increasing tempering temperature up to 200°C followed by an increase in retained austenite volume fraction up to 400°C (Figure 2.18). However, the retained austenite volume fraction decreased again for samples tempered at 500°C, suggesting 400°C to be the optimum tempering temperature. It was concluded that significant cementite precipitation occurred during the tempering treatment which resulted in lower C content in the retained austenite, making them chemically less stable. This chemically less stable retained austenite transformed to martensite during cooling to temperature. However, the dissolution of these cementite particles in retained austenite at 400°C resulted in more chemical stability in the austenite and prevented premature austenite to martensite transformation during final cooling. Moreover, high UTS (~1000 MPa) and ductility (~40%) were reported for the samples tempered at 400°C owing to significant volume fraction (~35%) of chemically stable retained austenite which gradually transformed to martensite during deformation.

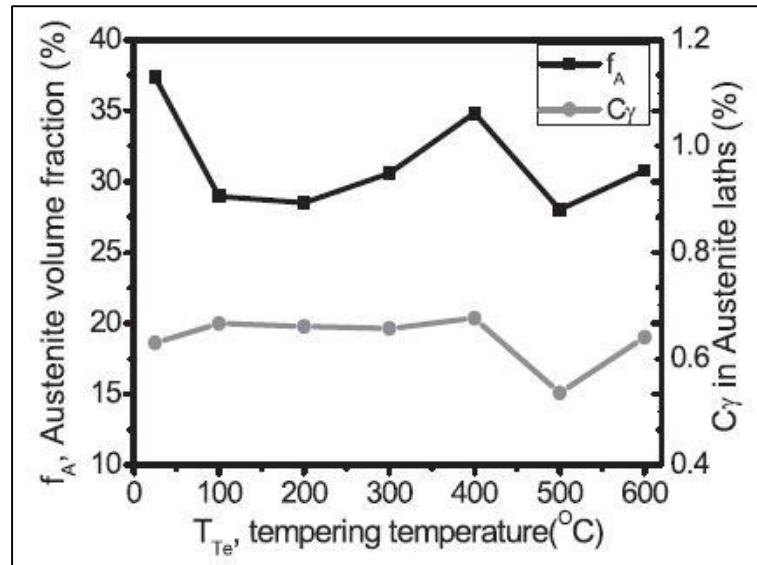


Figure 2.18: Variation of volume fractions and C content of retained austenite as a function of tempering temperature [50].

However, the effect of overaging temperature (OT) holding time on the microstructure, especially on the stability of the retained austenite, has not been studied extensively for medium Mn TRIP steels. Detailed study on the microstructural evolution during this stage is hence necessary as this stage is an integral part of the CGL processing cycle.

## 2.8 Effect of Heating Rate

De Cooman [32] reported that low alloy TRIP steel with a cold rolled starting microstructure consisting of ferrite, cementite and pearlite usually went through various changes during the rapid heating stage of the heat treatment. In particular, ferrite tended to recrystallize whereas cementite tended to dissolve first in ferrite and then in austenite. Austenite starts to form when the temperature crosses the  $A_{c1}$ .

However, medium Mn TRIP steels have higher alloy content which results in a different microstructure after hot and cold rolling. For example, Han et al. [45] showed that a hot rolled medium Mn (Fe-9Mn-0.05C wt.%) steel had a fully  $\alpha'$  martensitic microstructure. In this case, the high Mn content increased the hardenability of the steel which tended to result in martensitic microstructure even when the cooling rate was quite low [23]. Han et al. [45] also documented the microstructure of the cold rolled medium Mn steel which showed deformed  $\alpha'$  martensitic microstructure. The observed microstructures are shown in Figure 2.19. Lee and De Cooman [16] also reported similar microstructure for a Fe-0.3C-6Mn (mass %) TRIP steel after hot rolling and subsequent cold rolling. Hence, rapid heating to the intercritical annealing temperature for cold rolled medium Mn steels will have a different sequence of microstructural changes compared to low alloy TRIP steels. A recent study by Han and Lee [51] showed that the heating rate had a profound effect on the reverted austenite ( $\gamma$ ) phase stability, morphology as well as on cementite precipitation of Fe-(5-9)Mn-0.05C (wt.%) medium Mn steels. The authors used dilatation curves for a range of heating rate (1.5– 60°C/s) to observe the  $A_s$  ( $\alpha'$  to  $\gamma$  reverse transformation start temperature),  $A_f$  ( $\alpha'$  to  $\gamma$  reverse transformation finish temperature) and  $T_0$  (cementite precipitation start temperature). Their results showed that these three critical temperatures increased with heating rate up to 15°C/s, indicative of a diffusive reverse transformation which also resulted in the cementite precipitation.

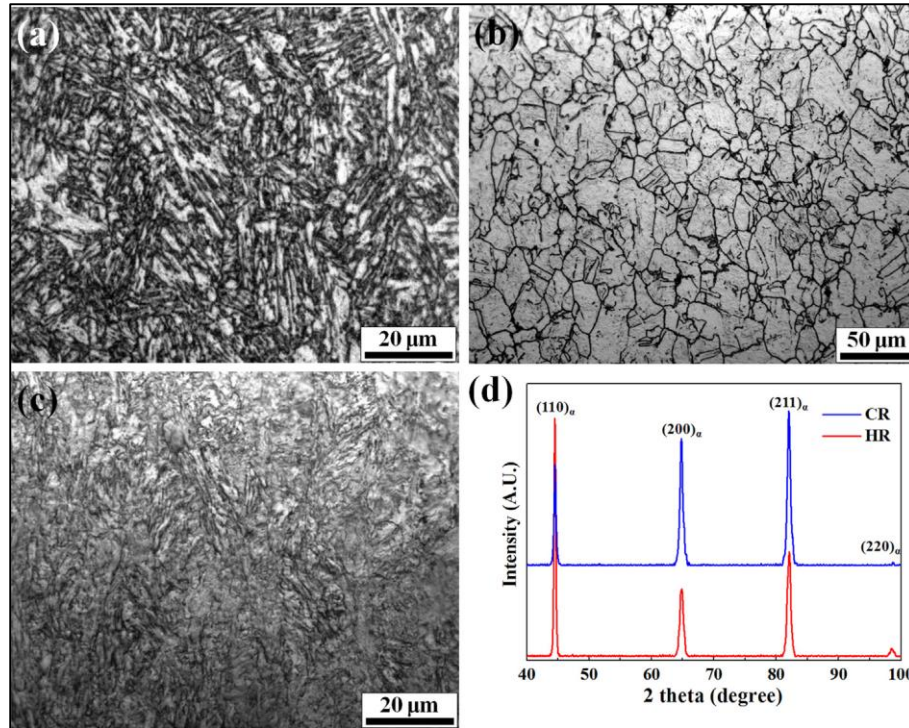


Figure 2.19: OM micrographs of Fe-9Mn-0.05C steel a)  $\alpha'$  martensite and b) prior austenite grain boundaries for hot rolled specimen and c) deformed  $\alpha'$  martensite for the cold rolled specimen and d) XRD patterns of hot and cold rolled specimens [51].

For heating rate above 15 °C/s, however, it was proposed that the reverse transformation of  $\alpha'$  to  $\gamma$  was diffusionless as cementite precipitates were absent. The diffusionless reverse transformation was confirmed as the critical temperatures  $A_S$  and  $A_f$  were almost constant with increasing heating rate up to 60°C/s, as shown in Figure 2.20. However, as this is a kinetic process, cementite nucleation might not have started where diffusionless reverse transformation occurred (>15°C/s heating rate). The morphology of the retained austenite also changed as the reverse transformation changed from diffusion based to diffusionless. Fine globular grains of reverted austenite with a low dislocation density were observed for the diffusion based reverse transformation at heating rate lower than 15 °C/s. On the other

hand, lath shaped reverted austenite grains with high dislocation density were observed in the case of diffusionless reverse transformation at heating rate greater than 15 °C/s.

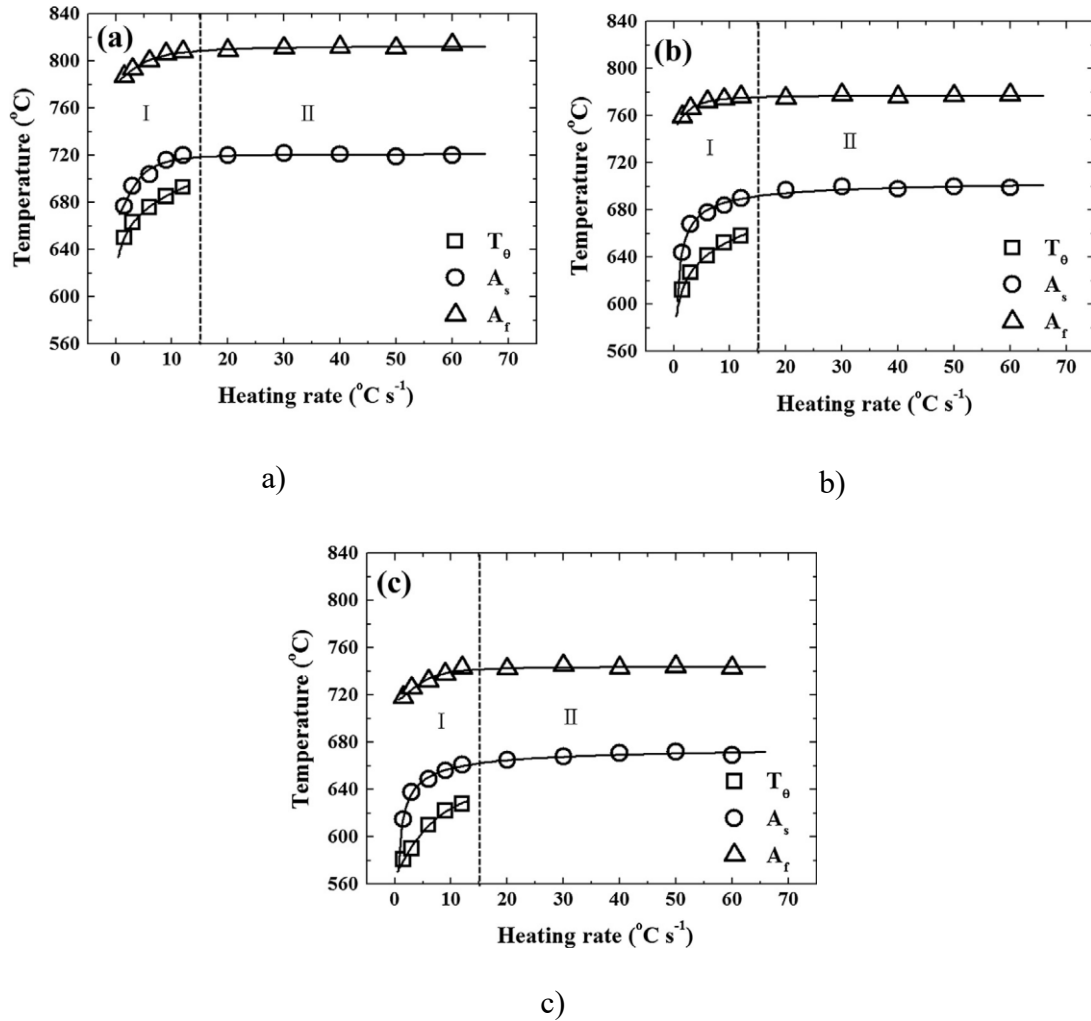


Figure 2.20: Change in critical temperatures as a function of heating rate for a) 5Mn, b) 7Mn and c) 9Mn steel specimens [51].

Lee and De Cooman [21] studied a Fe-10Mn-0.3C-3Al-2Si (wt.%) medium Mn steel which was annealed at 800°C for 10 minutes. A 4 K/s heating rate was used in their study. Cementite precipitation was observed at the low angle martensite lath boundaries during heating. It was also confirmed that intercritical austenite nucleated at ferrite/cementite

interface during intercritical annealing. This intercritical austenite grew and gradually replaced the cementite particles, resulting in a carbide free ultra-fine grained microstructure consisting of retained austenite and ferrite. It was suggested that the C content in the intercritical austenite was not due to C partitioning from ferrite but resulted from this cementite dissolution.

## **2.9 Effect of Cooling Rate**

Rapid cooling from the intercritical annealing temperature (IAT) is required in order to avoid the transformation of intercritical austenite to ferrite and pearlite. Although it is relatively easy to avoid pearlite formation, new ferrite tends to form even at higher cooling rates in case of conventional low alloy TRIP steels. A cooling rate of 120 °C/s was required to avoid new ferrite formation for a 1.2 wt.% Mn TRIP steel as reported by Garcia-Gonzalez [52]. However, previous study [53] has shown that increasing the Mn content from 1.2 wt.% to 2.4 wt.% can result in less drastic cooling rate requirements. A cooling rate of 50 °C/s was sufficient to avoid significant transformation of intercritical austenite to ferrite. This suggests that in case of medium Mn TRIP steels which have higher alloying elements in them, a moderate cooling rate would be sufficient enough to avoid ferrite formation during this stage.

Furukawa et al. [54] studied the effect of C content in the steel composition as well as the final cooling rate to room temperature of a hot rolled 5 wt.% Mn steel. The steel substrate was cooled by both furnace cooling and water quenching method. Although the amount of retained austenite and the corresponding mechanical properties were insensitive to the cooling rate for the steel with low carbon (0.1 wt.%) content, a marked dependence

on cooling rate were reported for higher carbon (0.3 wt.%) steel (Figure 2.21). Water quench or faster cooling yielded more retained austenite and hence better mechanical properties compared to that observed for furnace cooling or slower cooling. The reason for this type of behaviour was explained in terms of carbide precipitation associated with the different mode of cooling. The furnace cooled high carbon steel had a carbide network formed in the final microstructure. This suggested that the slower cooling promoted the growth of the carbide by diffusion of C from the adjacent intercritical austenite which resulted in austenite with lower chemical stability. This austenite with lower chemical stability then transformed to martensite during the slow furnace cooling. As a result, lower retained austenite volume fractions (Figure 2.21) and poor mechanical property balance was reported for the furnace cooled steel samples. On the other hand, the water quenched samples had some carbide precipitation, however, they did not grow into a network. This meant that the adjacent austenite had sufficient C in them to make them chemically stable during the cooling stage resulting in more retained austenite in the final microstructure.

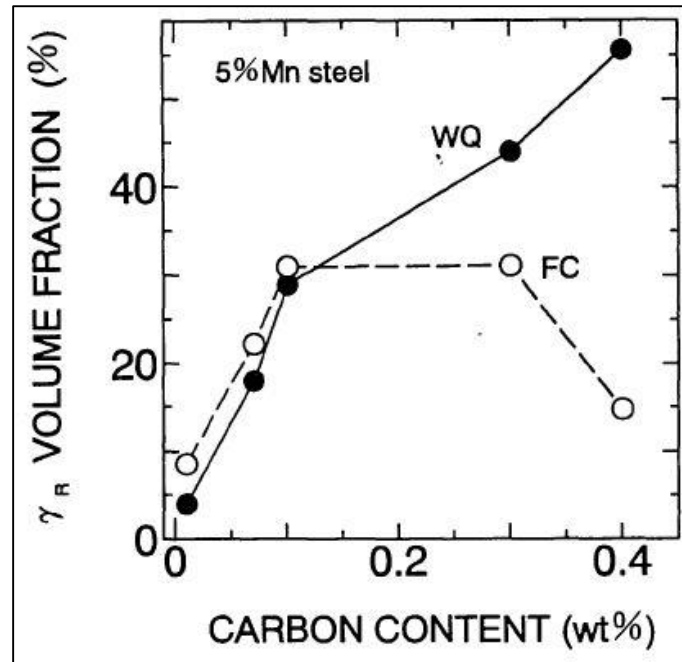
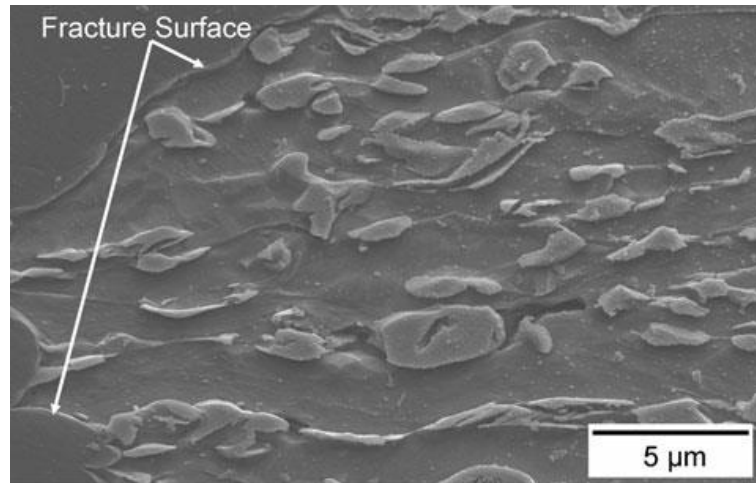


Figure 2.21: Effect of cooling rate and carbon content on the retained austenite volume fraction [54].

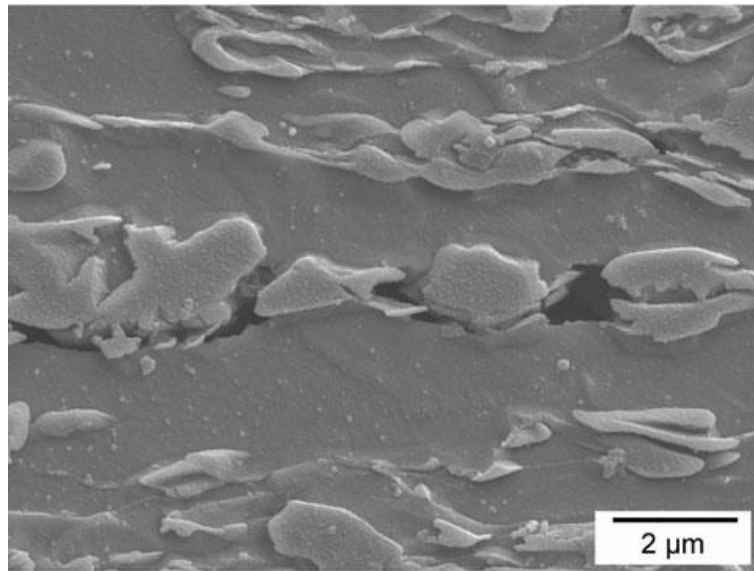
## 2.10 Fracture Mechanisms

There has not been any study which investigates the fracture mechanisms operating in medium Mn TRIP steels. However, fracture surface analysis of conventional low alloy TRIP-assisted steels might suggest some possible fracture mechanisms as transformation induced plasticity effect is observed in both type of steels. Previous research [1][32][55] has revealed that ductile type fracture mode operated in annealed low alloy TRIP-assisted steels. However, the damage processes leading to fracture varied depending on the steel chemistry, especially C content, and retained austenite amount as suggested by various researchers [55][56]. Zheng et al. [55] as well as Bellhouse and McDermid [1] observed microvoid formation at the interface boundary of ferrite and other harder phases. This likely

occurred due to significant strain accumulation in the ferrite during deformation. These microvoids coalesced and formed cracks that propagated through the ferrite and moved around the harder phases like martensite, bainitic ferrite and untransformed retained austenite. Figure 2.22 shows the SEM of the fractured surfaces of a TRIP steel analyzed by Bellhouse and McDermid [1]. Microvoid formation was observed at the interface between the softer ferrite and the harder martensite phase which suggested decohesion between the phases during the damage accumulation stage of deformation. The cracks were reported to have propagated along the martensite and ferrite interfaces and along the tensile axis. Similar fracture mechanisms were also reported by De Cooman [32] and Yu et al. [57]. However, Furnémont et al. [56] reported cracking of the martensite phase during the damage accumulation stage which suggested that the local strain was too high (Figure 2.23).



(a)



(b)

Figure 2.22: SEM images of cross section of fractured tensile samples showing preferential sites for void formation and crack propagation (untempered): (a) 1.5 Al (35 pct  $\gamma$ ) steel and IBT time = 60s, (b) 1.5 Al (35 pct  $\gamma$ ) steel and IBT time = 90s [1].

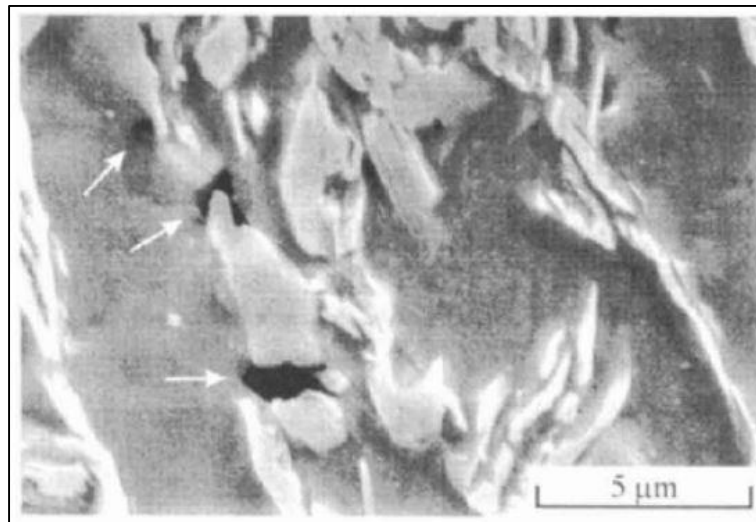


Figure 2.23: Fracture mechanism in TRIP-assisted steel showing cracking of martensite

[56].

### **3 RESEARCH OBJECTIVES**

The heat treatment of medium Mn TRIP steels plays a vital role in determining the microstructure and the corresponding mechanical properties, as the literature review suggests. Most of the previous investigations [2] [15] employed a long holding time at the intercritical annealing temperature, which makes them incompatible with the CGL process regardless of their superior mechanical property balance, meeting the target mechanical properties for 3G-AHSSs. Thus, the main goal of this research is to develop a processing window for a prototype medium Mn TRIP steel that is compatible with the constraints associated with the continuous galvanizing line and produces the desired 3G-AHSS microstructure and meets the mechanical property targets. In that regard, the research objectives of this investigation are:

- Develop a heat treatment profile for a prototype medium Mn TRIP steel.
- Determine the effect of intercritical annealing parameters (temperatures and holding times), starting microstructure, overaging temperature (OT) holding time on the microstructure and mechanical properties of the annealed steels.
- Determine microstructure evolution and microstructure-mechanical property relation.
- Determine retained austenite to martensite transformation kinetic during straining.
- Assess the mechanical properties with respect to target mechanical properties of 3G-AHSSs and determine optimal CGL compatible thermal processing conditions for the prototype steel.

## 4 EXPERIMENTAL

### 4.1 Material Chemistry and Sample Preparation

The composition of the prototype medium Mn TRIP steel is given in Table 4.1. Si and Al were added in order to delay carbide precipitation during annealing and also for solid solution strengthening with the former having a more pronounced effect [29]. Mn, on the other hand, acted as austenite stabilizer whereas the C content of the steel was carefully selected keeping the weldability of the steel in mind. Cr was added to achieve better hardenability during heat treatment. Armco Fe, electrolytic Mn, ferrosilicon and ferrochromium were used as the raw materials for the alloy, where all alloys were melted in a vacuum induction furnace which was backfilled with Ar. The steel was cast as an ingot of 230 kg with ingot dimensions being (18 cm × 30 cm × 56 cm). The ingot was then reheated to 1260°C and hot rolled. The hot roll finishing temperature was 906°C and the final hot rolled thickness was 4.6 mm. The hot rolled steel sheet was then ground to a thickness of 3 mm and martempered at 415°C for 6 hours prior to cold rolling. Finally, the steel was cold rolled to a thickness of 1.4 mm.

Table 4.1 Chemical Composition of the Prototype 3G-AHSS (wt.%)

C	Mn	Si	Al	Cr	Mo	Ti	S	C.E.
0.21	6.12	1.69	0.42	0.50	0.07	0.009	0.0056	1.4

Two types of heat treatment samples were used in this study. Smaller samples comprising 10 mm × 50 mm coupons were used for X-ray Diffraction (XRD), Scanning

Electron Microscopy (SEM) and Transmission Electron Microscopy (TEM) analysis after heat treatment. Larger samples, consisted of 120 mm × 200 mm panels, were used for the tensile tests after cutting the tensile specimens out of the panels by Electric Discharge Machining (EDM).

#### **4.2 McMaster Galvanizing Simulator (MGS)**

All heat treatments were carried out in the McMaster Galvanizing Simulator (MGS, Iwatani-Surtec), shown in Figure 4.1. A detailed schematic diagram of the MGS is shown in Figure 4.2. The MGS has two main sections, where the top and bottom section are separated by a gate valve (Figure 4.2). The top section includes the upper chamber, which is used for sample loading and unloading as well as for cooling the samples at a controlled rate, and the annealing furnaces. There are two furnaces in the MGS, used to simulate annealing heat treatments; a quartz-tube infrared furnace (IR) and a high frequency induction furnace (IH). Only the IR furnace was used in this study. The bottom section is used for simulating the galvanizing of steel samples by dipping them into liquid zinc after annealing. This section also has a nitrogen gas jet wiping system that controls the coating thickness. However, this section was not used in this study as no zinc coatings were applied.

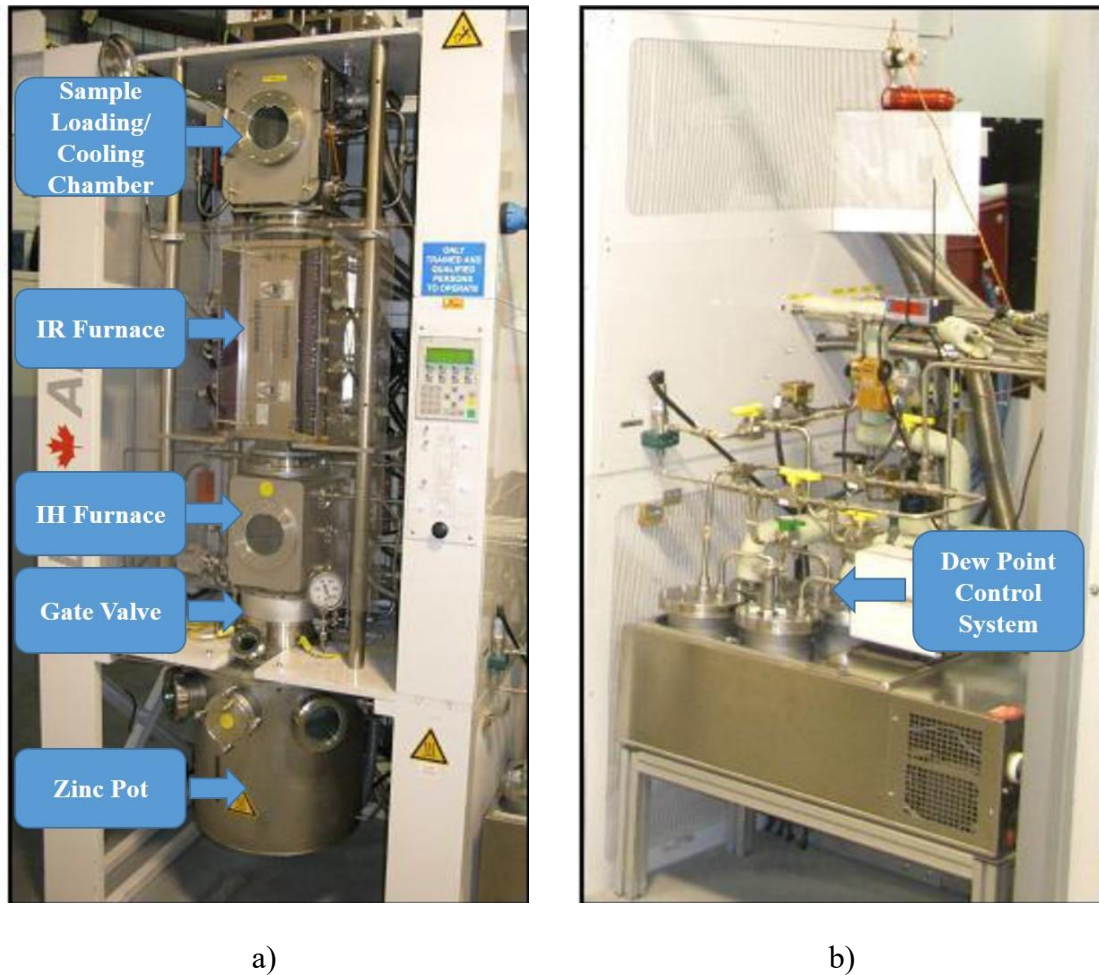


Figure 4.1: a) McMaster Galvanizing Simulator (MGS) main column and b) gas mixing system.

All samples were cleaned using an 80°C 2% NaOH aqueous solution and a nylon brush followed by rinsing using water, ultrasonic cleaning in isopropanol and drying using a warm air stream. The temperature of the steel samples was monitored by using a type K thermocouple that was spot welded to the sample prior to heat treatment. Figure 4.3 shows the two different sample types used in this investigation along with the corresponding thermocouple positions. The cooling rate of the annealed samples was controlled by N<sub>2</sub> gas

flow which was adjusted accordingly to conform with the target cooling rates via feedback control as determined using the sample thermocouple readings.

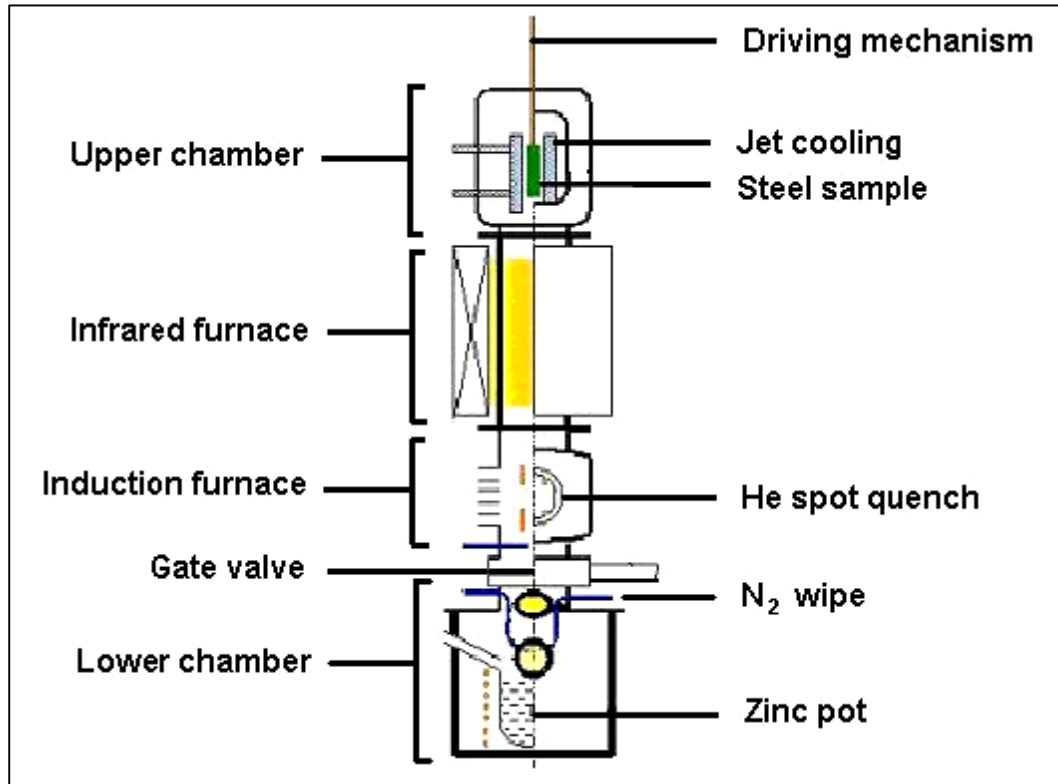


Figure 4.2: Schematic diagram of the McMaster Galvanizing Simulator (MGS) [58].

All sections of the MGS were atmosphere controlled such that the process atmosphere oxygen partial pressure was reducing with respect to FeO. This was done through the introduction of controlled amounts of water vapour into the N<sub>2</sub>-5H<sub>2</sub> (vol.%) atmosphere, where the water vapour partial pressure was characterised using the atmospheric dew point. The dew point of the process atmosphere was controlled by mixing saturated water vapour and dry N<sub>2</sub>-5H<sub>2</sub> gas streams where the relative proportions of the wet and dry N<sub>2</sub>-5H<sub>2</sub> flow rates were controlled by a system of mass flow controllers. All gas streams were then mixed using a conventional a gas mixing chamber to achieve the

desired atmosphere during annealing. It should be mentioned that the process gas entered the MGS column immediately above the gate valve (Figure 4.1) and exited the MGS column immediately below the sample chamber.

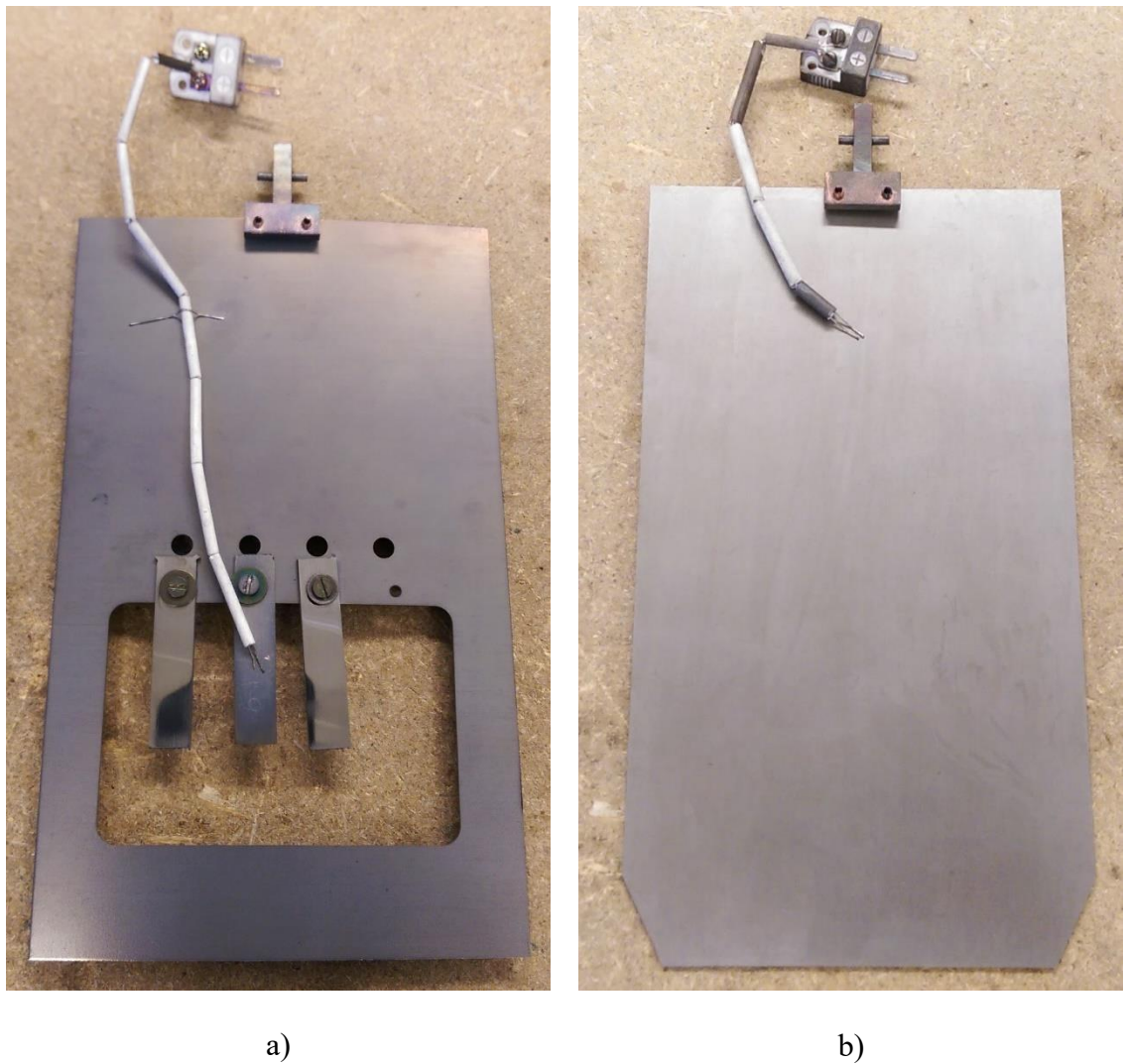


Figure 4.3: a) Microstructural examination sample coupons and b) panel samples for mechanical property testing, showing corresponding thermocouple positions.

### 4.3 ThermoCalc Calculations

ThermoCalc software with the TCFE 6 database was used in order to determine the equilibrium austenite volume fraction as a function of annealing temperature, as shown in Figure 4.4. Equilibrium C and Mn partitioning were also calculated as a function of annealing temperature. The results of these calculations are shown in Figure 4.5. This was done to identify the temperature that resulted in the highest amount of C partitioning with an acceptable Mn partitioning to the austenite, as proposed by Lee and De Cooman [16], to select the optimal annealing temperature which would yield the highest volume fractions of retained austenite. However, it should be kept in mind that Mn does not partition significantly whereas C partitioning was more likely to reach equilibrium within a relatively short time [32].

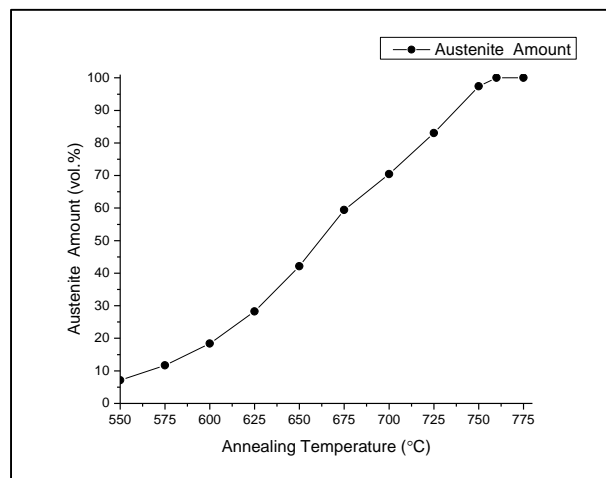


Figure 4.4: Austenite volume fraction as a function of annealing temperature.

Within the context of the present study, it should be noted that the steel strip is usually in the heat treatment section of the CGL for few minutes only, which is not sufficient to reach equilibrium conditions, especially for the substitutional elements. As a result,

ThermoCalc calculations, which represent equilibrium conditions, are often not completely suitable for developing CGL compatible thermal processing cycles and must be supplemented with kinetic data. Dilatometry can provide data regarding phase transformation kinetics and temperatures under non-equilibrium conditions. Hence, it was used to supplement the equilibrium calculations in this investigation. The following section discusses the method in detail.

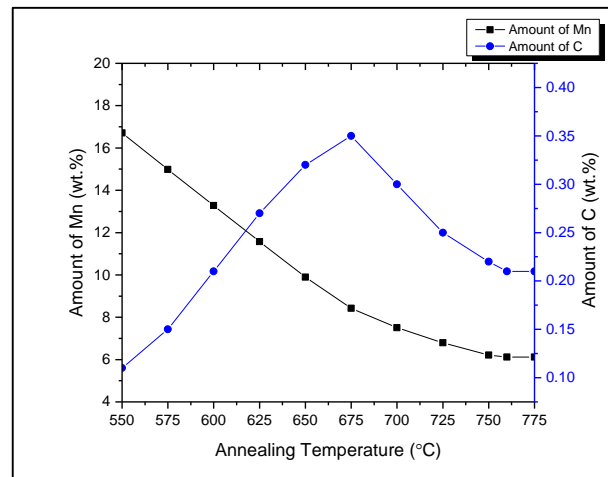


Figure 4.5: C and Mn partitioning in austenite as a function of annealing temperature.

#### 4.4 Dilatometry and Starting Microstructures

Dilatometry was done to determine the Ac1 and Ac3 temperatures of the steel as a function of CGL compatible heating rates. The results of this investigation are shown in Figure 4.6. It was revealed that the Ac1 and Ac3 temperatures for the as-received tempered martensite microstructure changed significantly with the heating rate. A heating rate of 5°C/s was chosen for this study considering known parameters for typical CGL processing windows. The Ac1 and Ac3 temperatures were determined to be 520°C and 765°C, respectively, for this heating rate.

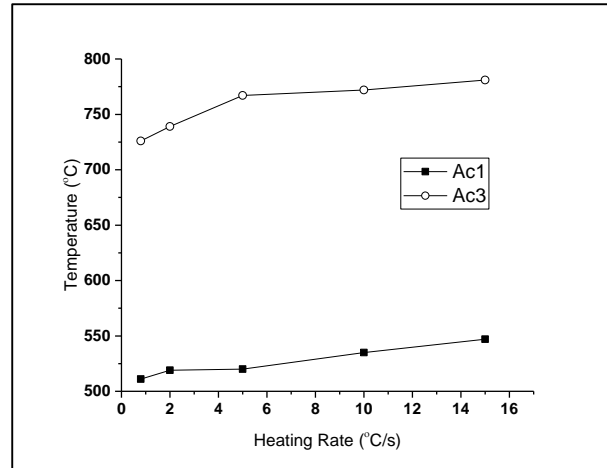


Figure 4.6: Ac1 and Ac3 temperatures versus heating rate.

Starting microstructure was one of the variables in this study. In this regard, selected samples of the as-received tempered martensite starting microstructure (S-TM) were subjected to a 600s austenitizing heat treatment at 775°C followed by gas quenching (-30°C/s) to room temperature, as shown in Figure 4.7. This resulted in a martensitic microstructure (S-M), confirmed by SEM characterization and microhardness test. Figure 4.8 shows the SEM micrographs of the as-received S-TM sample and the heat treated S-M sample with the martensitic microstructure. Microhardness tests were done which revealed an increase in hardness after the austenitizing heat treatment. The as-received S-TM sample had a hardness of HV 460 ± 23 whereas the S-M sample had a hardness of HV 570 ± 28.5.

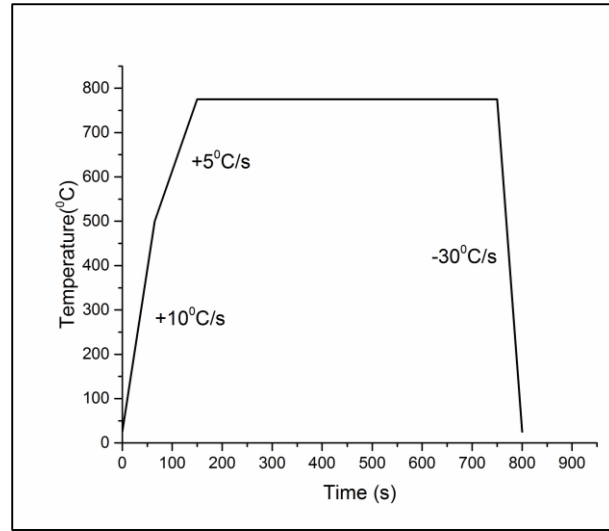
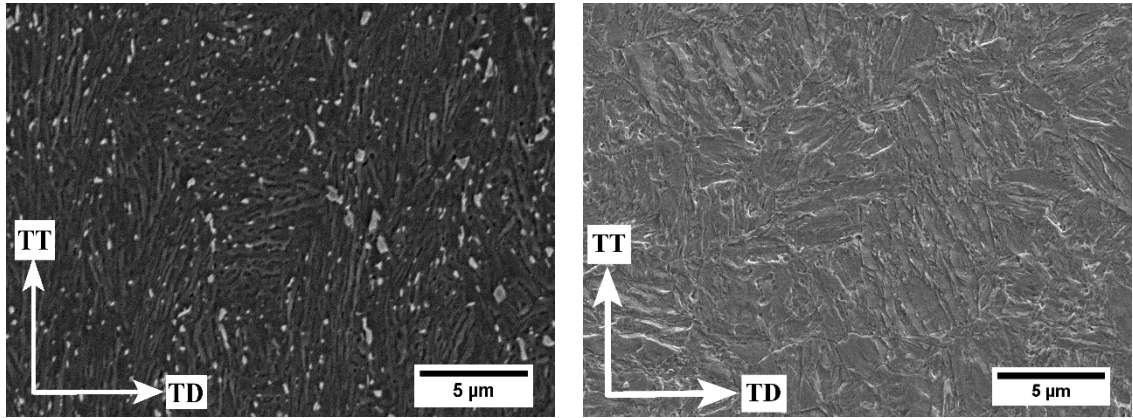


Figure 4.7: Schematic diagram of the austenitizing heat treatment.



a)

b)

Figure 4.8: SEM micrographs of a) as-received S-TM samples with tempered martensite and b) heat treated S-M samples with martensite.

#### 4.5 Thermal Processing Cycle

Based on the dilatometry results and the known industrial CGL practice, a two stage heat treatment profile was designed for the experimental medium Mn TRIP steel. The steel

samples were first heated to an intercritical annealing temperature (IAT) and were then cooled at  $-10^{\circ}\text{C/s}$  to an overaging temperature (OT). Finally, the samples were cooled to room temperature at  $-10^{\circ}\text{C/s}$ . The samples were held for variable times at both the IAT and OT. All experiments were carried out in a  $\text{N}_2$ -5vol%  $\text{H}_2$  process atmosphere with a  $-30^{\circ}\text{C}$  dew point. A schematic diagram of the heat treatment profile is shown in Figure 4.9.

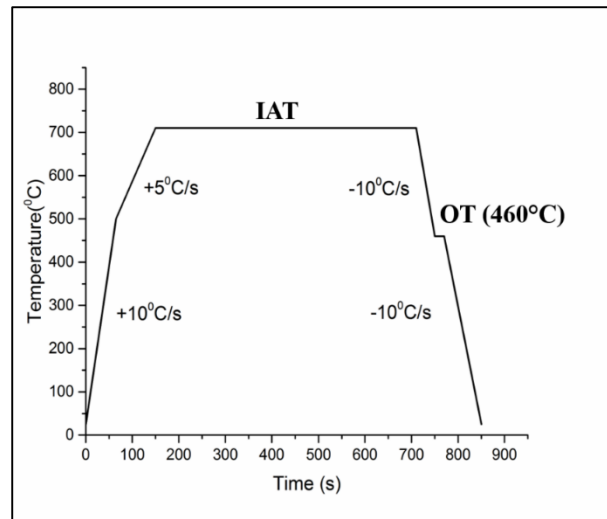


Figure 4.9: Schematic diagram of the experimental heat treatment.

The intercritical annealing temperatures were chosen from the dilatometry results such that they would result in high volume fractions of intercritical austenite. For this study, the chosen IATs were  $675^{\circ}\text{C}$  and  $710^{\circ}\text{C}$  which would yield 50% and 75% intercritical austenite, respectively, according to the dilatometry results. An overaging temperature (OT) heat treatment was used in an effort to form chemically stable retained austenite at room temperature. The OT temperature was selected considering CGL compatibility. The zinc pot is generally kept at  $460$ - $465^{\circ}\text{C}$ , so the temperature in the isothermal hold prior to dipping is usually in this range to promote thermal stability of the Zn pot. Bellhouse and

McDermid [1] were successful in obtaining the desired microstructure and mechanical properties for a series of Al-Si low alloy TRIP-assisted steels using an IBT temperature of 465°C. In this study, an OT of temperature of 460°C was chosen and the holding time at OT was varied to determine its effect on the microstructure, stability and mechanical properties of the heat treated substrate. Table 4.2 shows a summary of the heat treatment parameters used in this study and includes the oxygen partial pressure for each IAT for the N<sub>2</sub>-5H<sub>2</sub> (vol.%) and –30°C dew point process atmospheres employed.

Table 4.2 Summary of Heat Treatment Parameters

Sample ID	IAT (°C)	Holding Time (s)	OT (°C)	Holding Time (s)	pO <sub>2</sub> at IAT (atm)
S-TM	675	60, 120, 240, 300, 480, 600	460	20	2.879 × 10 <sup>-26</sup>
	710	60, 120, 240, 300, 480, 600	460	20	2.695 × 10 <sup>-25</sup>
		60, 120, 240, 300, 480, 600		120	
S-M	675	60, 120, 240, 300, 480, 600	460	20	2.879 × 10 <sup>-26</sup>
		60, 120		120	
	710	60, 120, 240, 300, 480, 600	460	20	2.695 × 10 <sup>-25</sup>

## 4.6 Analysis Techniques

### 4.6.1 X-ray Diffraction

The annealed steel samples were analyzed using X-ray Diffraction (XRD) in order to measure the retained austenite, ferrite and martensite volume fractions. The cross-sections of the annealed steel samples were analyzed after grinding using a series of SiC papers, 4000 grit SiC being the final polishing step, to remove approximately 500  $\mu\text{m}$  from the cross-section to eliminate any effects arising from cutting the samples using the precision cutter.

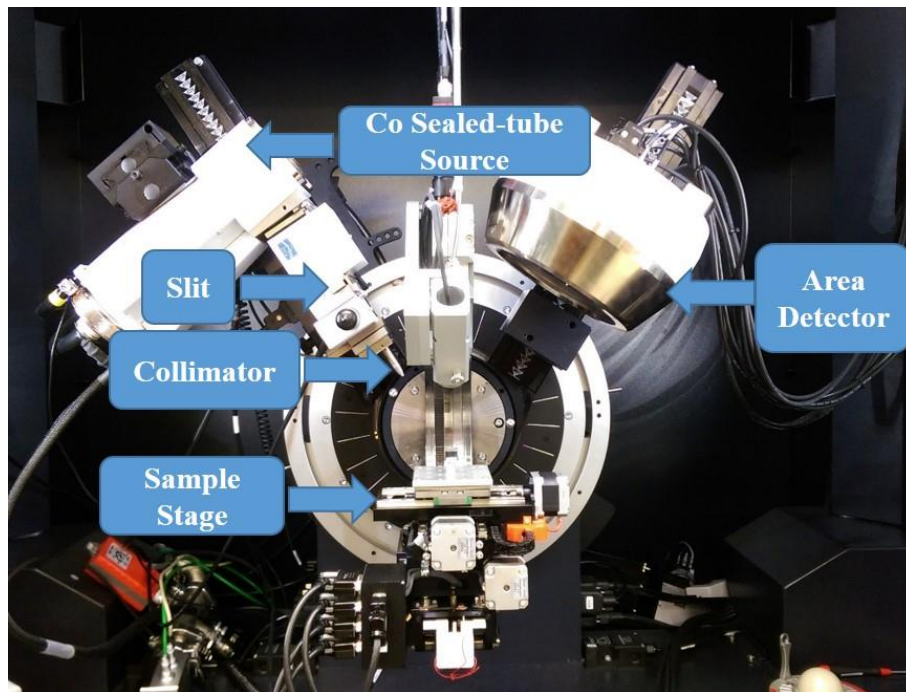


Figure 4.10: XRD apparatus with Co  $K\alpha$  radiation source.

A D8 DISCOVER with DAVINCI X-ray system was used in this study. The system used a Co  $K\alpha$  ( $\lambda = 1.79026 \text{ \AA}$ ) radiation source. Figure 4.10 shows the different components of the XRD machine. The collimator and slit were both 0.5 mm and the sample was rotated

during data acquisition to minimize any texture effect. The data acquisition time was 1200s per frame and four frames were taken per sample in the  $2\theta$  range of  $37^\circ$  to  $115^\circ$  with a  $19.5^\circ$  increment per frame. DIFFRAC.EVA v.4.0 software was used to process the diffraction data and obtain an intensity vs.  $2\theta$  plot. TOPAS v.4.2 software was used to analyze the intensity vs.  $2\theta$  plot. The measured intensity was normalized with respect to the calculated structure factor for each phase and then the entire diffraction pattern was used to determine the volume fraction of the different phases. It also calculated the analysis error based on the calculated and measured diffraction patterns. The ASTM E975-13 [59] standard was used to determine the retained austenite volume fraction in the annealed steel samples, where the (111), (200) and (220) austenite peaks were used whereas the (110), (200) and (211) peaks were used for the ferrite volume fraction calculation.

The C content in the retained austenite, which is partially indicative of the chemical stability of the retained austenite, was also calculated from the XRD data. The austenite lattice parameter ( $a$ ) was calculated by the TOPAS v.4.2 software. This was used to determine the C content in the retained austenite by using the combined equations of Ruhl and Cohen [60] for C, Mn and Si and Dyson and Holmes [61] for Al:

$$a(\text{\AA}) = 3.572 + 0.0012 (\text{wt pct Mn}) - 0.00157 (\text{wt pct Si}) + 0.0056 (\text{wt pct Al}) + 0.033 (\text{wt pct C}) \quad (2)$$

#### **4.6.2 Scanning Electron Microscopy**

The microstructure of annealed steel sample cross-sections was analyzed using a JEOL 7000F field emission scanning electron microscope (FEG-SEM). The samples were coated with carbon in order to eliminate charging. Samples were prepared using standard

metallographic techniques and were etched using 2% nital prior to metallographic examination.

The fracture surface of selected tensile samples tested to failure was analyzed using a JEOL 6610-LV scanning electron microscope. This SEM was chosen for fractography due to its high depth of focus at lower magnifications. The samples were tilted at an angle of 5° to enhance the contrast of the features of the fractured surfaces. The parameters used for SEM analysis are given in Table 4.3.

Table 4.3 Summary of SEM Parameters

Sample Condition	SEM	Acceleration Voltage (keV)	Working Distance (mm)	Tilt (°)
As-received	JEOL 7000F	10	10	-
Annealed	JEOL 7000F	10	10	-
Fracture Surfaces	JEOL 6610-LV	5	20	5

#### 4.6.3 Transmission Electron Microscopy

Fine scale microstructural analysis was done using transmission electron microscopy (TEM) for determining phase distribution and morphology in annealed steel samples. Two different TEMs were used in this study: a PHILIPS CM12 and a JEOL 2010F TEM with an Oxford INCA Pentafet energy dispersive X-ray (EDX) spectrometer. TEM samples

were prepared using a twin jet electro-polisher with a voltage of 16 V and an electrolyte containing 10% perchloric acid and methanol at -40°C.

The PHILIPS CM12 was used for microstructural analysis using an acceleration voltage of 120 keV. The JEOL 2010F TEM/STEM was used to do EDX analysis. EDX was performed in scanning transmission electron microscopy (STEM) mode with a probe size of 1 nm and acceleration voltage of 200 keV. Quantitative point analysis was carried out in order to characterize the carbide chemistry and other microstructural features.

#### ***4.6.4 Tensile Testing***

Uniaxial tensile tests were carried out for annealing conditions that resulted in higher volume fractions of retained austenite in the microstructure, as determined using XRD. An Instron 100 kN tensile frame was used for all tensile tests. All the tests were done at room temperature with a crosshead speed of 1 mm/min. Steel panels (120 mm × 200 mm) were annealed in the MGS and ASTM E8M- 01ε2 [62] subsize tensile specimens were cut from the uniform heating area of the annealed panels using electrical discharge machining (EDM) where the tensile direction of all samples was parallel to the rolling direction (RD) of the steel sheet. EDM was used in order to avoid any strain-induced transformation of retained austenite present prior to tensile testing. The dimensions of the tensile specimens are shown in Figure 4.11.

Interrupted tensile tests were also conducted for selected annealing conditions in order to determine the retained austenite to martensite transformation kinetics during deformation. In that regard, samples were subjected to different level of engineering tensile strain (5%, 10%, 15%, etc.). The samples were then cut using a precision cutter. The cross

section of these samples was analyzed using XRD and the previously documented procedure to determine the retained austenite volume fraction.

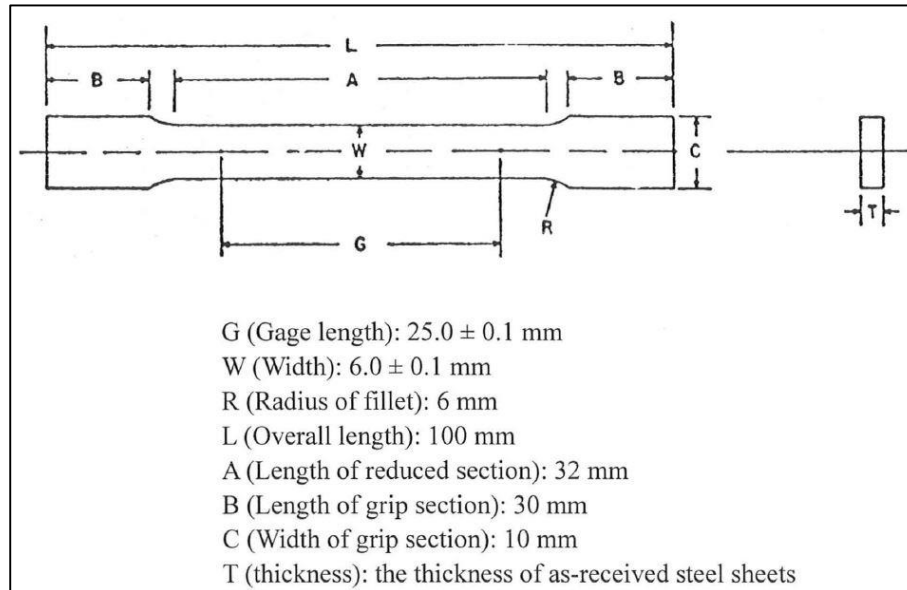


Figure 4.11: ASTM E8M- 01ε2 [62] tensile specimen dimensions.

## **5 RESULTS**

The results are divided into two subsections. The first discusses results related to the effect of intercritical annealing (IA) parameters (e.g. temperature and holding time) with different starting microstructures. In these cases, the overaging temperature (OT) was 460°C and the OT holding time was 20s. The effects of OT holding time were determined in the second part of this chapter, where the OT holding time was varied from 20-120s in order to determine its effect on retained austenite stability and mechanical properties of the experimental medium Mn TRIP steel.

### **5.1 Effect of Intercritical Annealing Temperature and Holding Time**

#### **5.1.1 XRD Results**

The volume fraction of retained austenite and retained austenite C content for the tempered martensitic (S-TM) and martensitic (S-M) samples annealed at the 675°C and 710°C intercritical annealing temperature (IAT) for a variety of holding times were determined using X-ray diffraction (XRD) and the results are shown in Figure 5.1 and Figure 5.2 for the S-TM and S-M starting microstructures, respectively. The retained austenite volume fraction increased with holding time for both IATs for the S-TM samples (Figure 5.1). The higher IAT (710°C) and longest holding time (600s) were necessary to yield the highest volume fraction of retained austenite (~0.37) for the S-TM samples. This was consistent with the results observed by De Moor et al. [63] and Lee et al. [64]. On the other hand, the volume fraction of retained austenite was approximately 0.10 for the lower IAT (675°C) with a 600s holding time. The C content in the retained austenite did not

change significantly regardless of the IAT or the holding time at IAT for the S-TM samples (Figure 5.1).

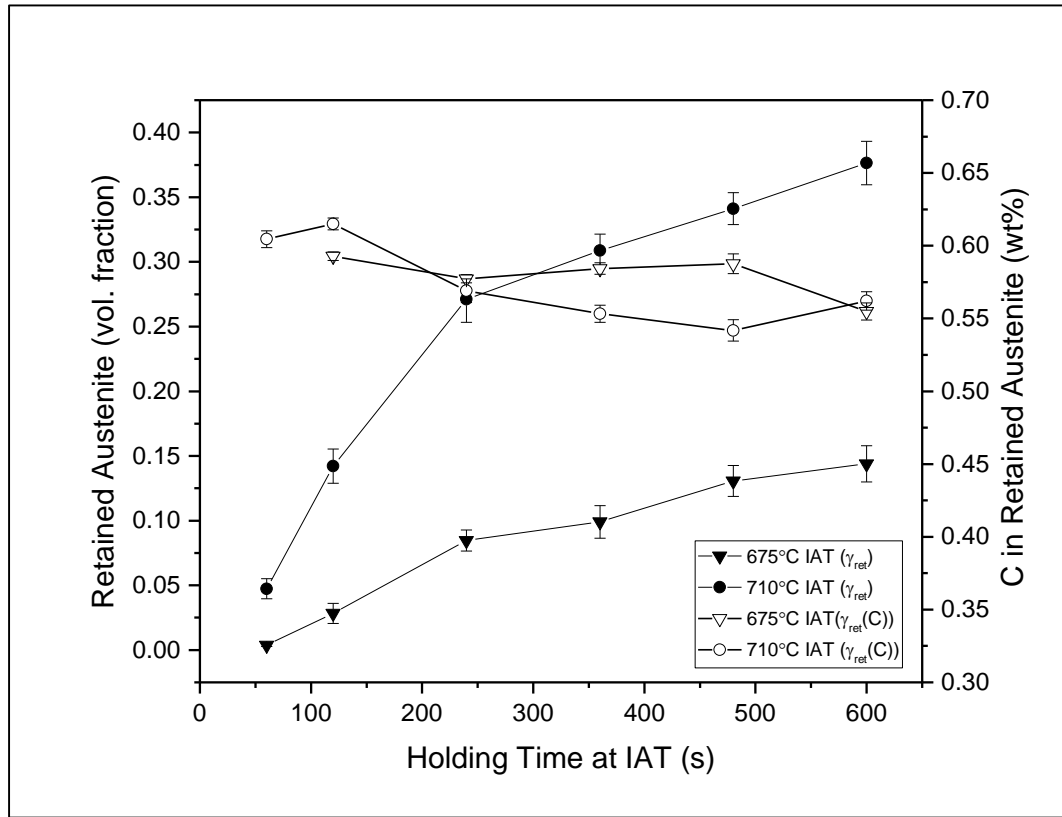


Figure 5.1: Retained austenite volume fraction and C content as a function of intercritical annealing temperature and holding time for S-TM samples.

XRD results for the S-M samples showed a different trend in retained austenite volume fraction evolution (Figure 5.2). The retained austenite volume fraction increased with holding time at the 675°C IAT up to 360s and then decreased significantly with increasing holding time. This decrease in retained austenite fraction started much earlier at the 710°C IAT, in this case, for the 60s holding time. The lowest retained austenite volume fraction for the 710°C IAT was observed for the 600s holding time, approximately 0.10. This can

likely be attributed to chemically unstable intercritical austenite which transformed to martensite during cooling. This hypothesis is supported by the martensite volume fraction increasing significantly with increasing holding time at the intercritical annealing temperature for the S-M samples, as shown in Figure 5.3. The C content in the retained austenite for the 710°C IAT also followed a similar decreasing trend. This also suggests that the intercritical austenite may not have been sufficiently stable during the final cooling owing to its lower carbon content and decreased chemical stability of the retained austenite.

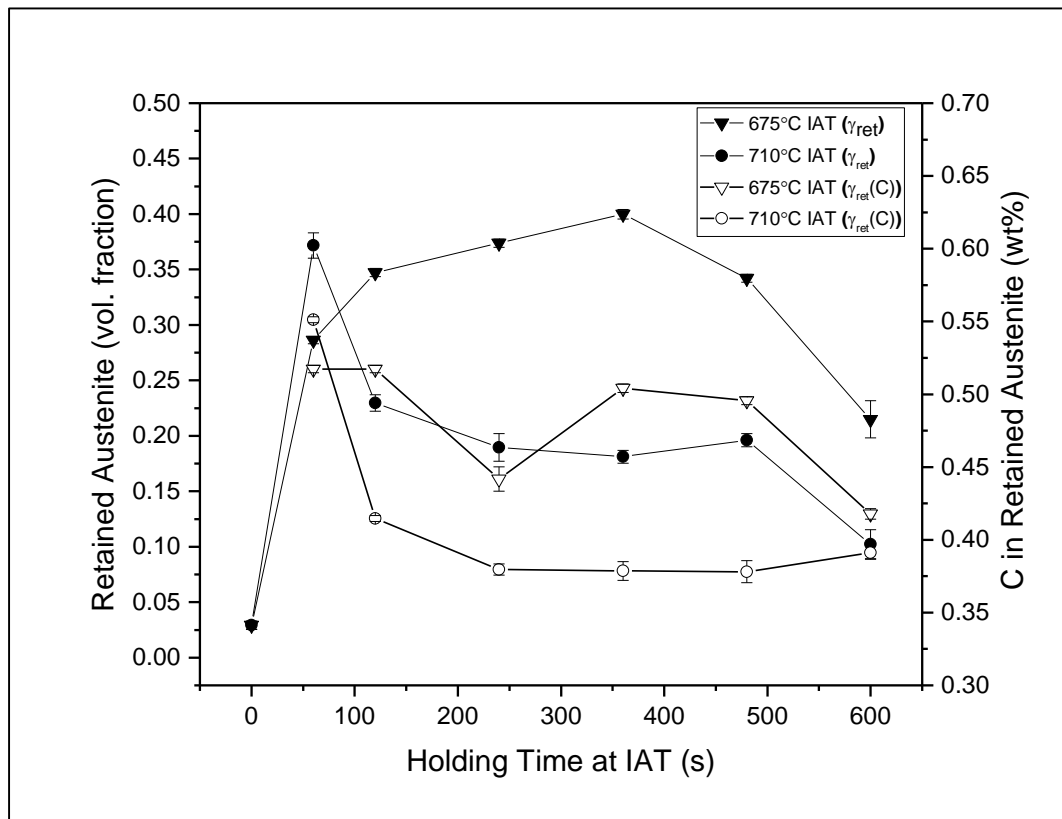


Figure 5.2: Retained austenite volume fraction and C content as a function of intercritical annealing temperature and holding time for S-M samples.

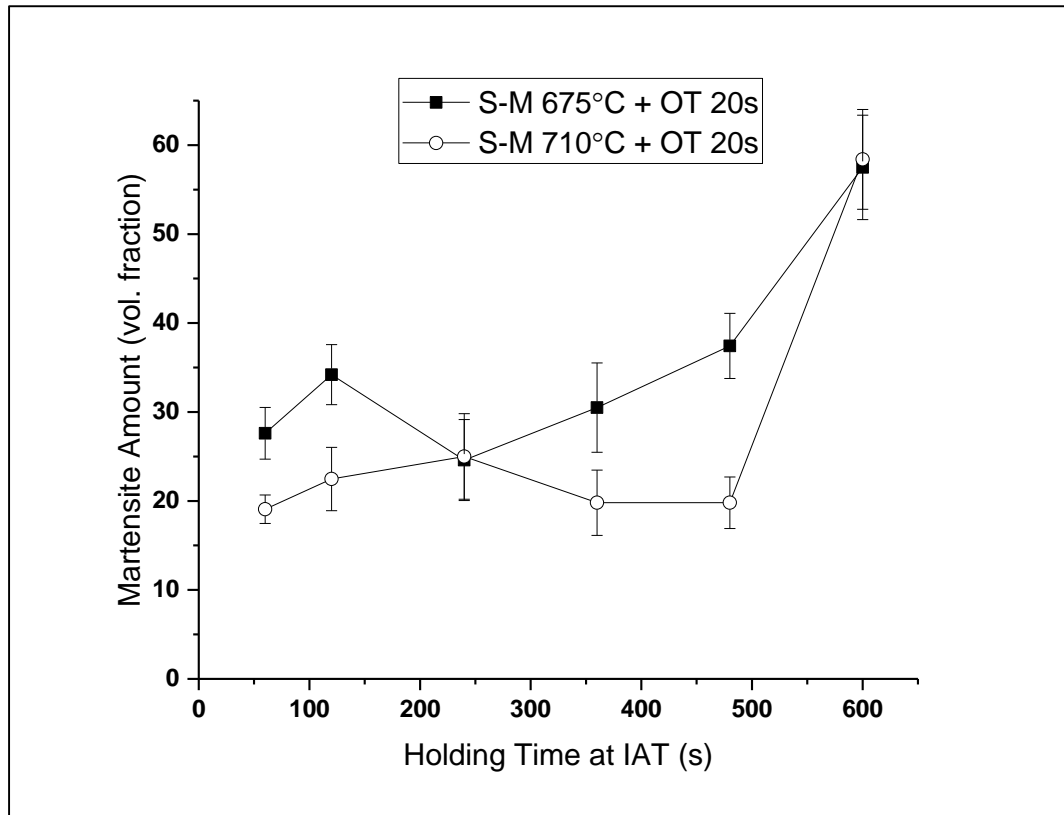


Figure 5.3: Martensite volume fraction as a function of holding time at 675°C and 710°C IATs for S-M samples.

### 5.1.2 Microstructural Characterization by SEM

The microstructures of the annealed samples were analyzed using scanning electron microscopy (SEM). Figure 5.4 and Figure 5.5 show the microstructures of the annealed S-TM samples for the 675°C and 710°C IAT as a function of holding time, respectively. It should be noted that in the micrographs F = Ferrite, M = Martensite and A = Austenite. The microstructures were a mixture of ferrite/bainitic ferrite, retained austenite and athermal martensite. The micrographs correlated well with the XRD results discussed in the previous section. The retained austenite fraction increased significantly with holding time at the

710°C IAT (Figure 5.5). Both lamellar and block shaped retained austenite were identified in the 710°C IAT S-TM samples. However, it was difficult to identify retained austenite in the 675°C IAT samples as the retained austenite volume fraction was low.

SEM microstructures of the S-M samples are shown in Figure 5.6 and Figure 5.7 for the 675°C and 710°C IAT samples, respectively. The retained austenite volume fraction was higher for all S-M samples compared to the S-TM samples; thus, it was easier to identify it in the micrographs. Both blocky and lamellar retained austenite were observed in these samples. The retained austenite volume fraction increased to IAT holding times of 360s and then decreased for the longer 675°C IAT holding time samples (Figure 5.6), correlating with the XRD results. For the 710°C IAT samples (Figure 5.7), athermal martensite gradually increased and retained austenite decreased with increasing holding time.

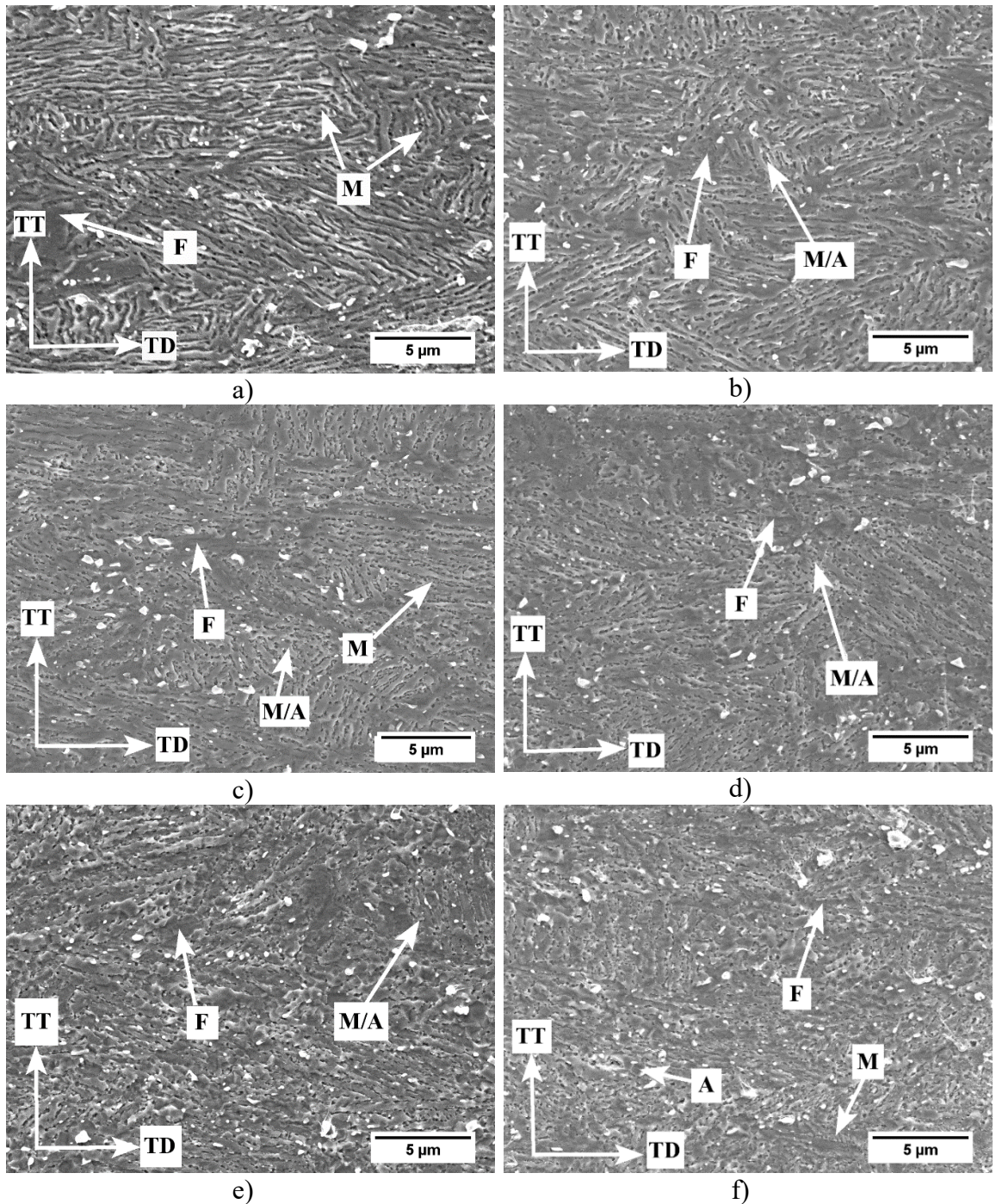


Figure 5.4: SEM micrographs of S-TM samples subjected to 675°C IAT for a) 60s, b)

120s, c) 240s, d) 360s, e) 480s and f) 600s.

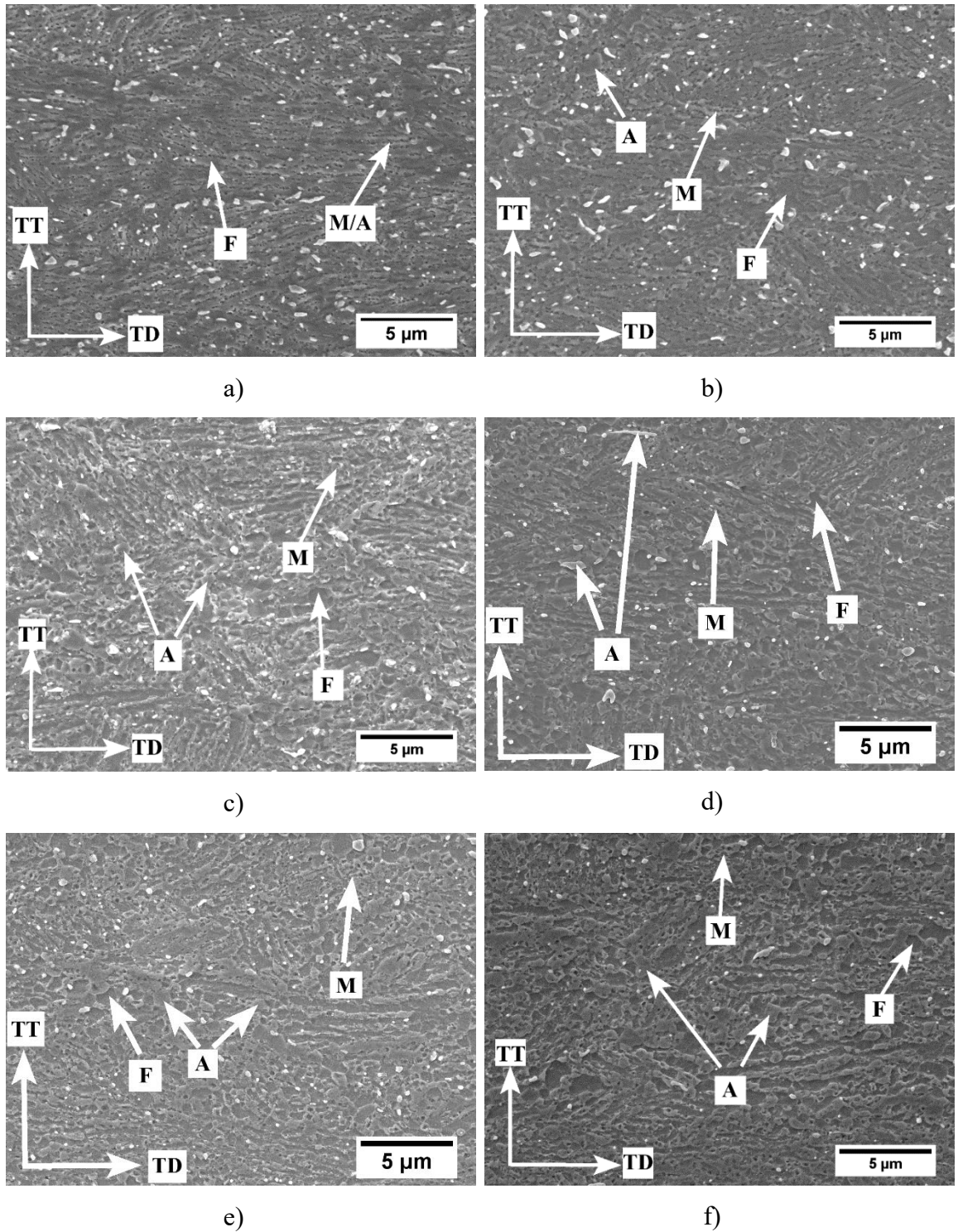


Figure 5.5: SEM micrographs of S-TM samples subjected to 710°C IAT for a) 60s, b) 120s, c) 240s, d) 360s, e) 480s and f) 600s.

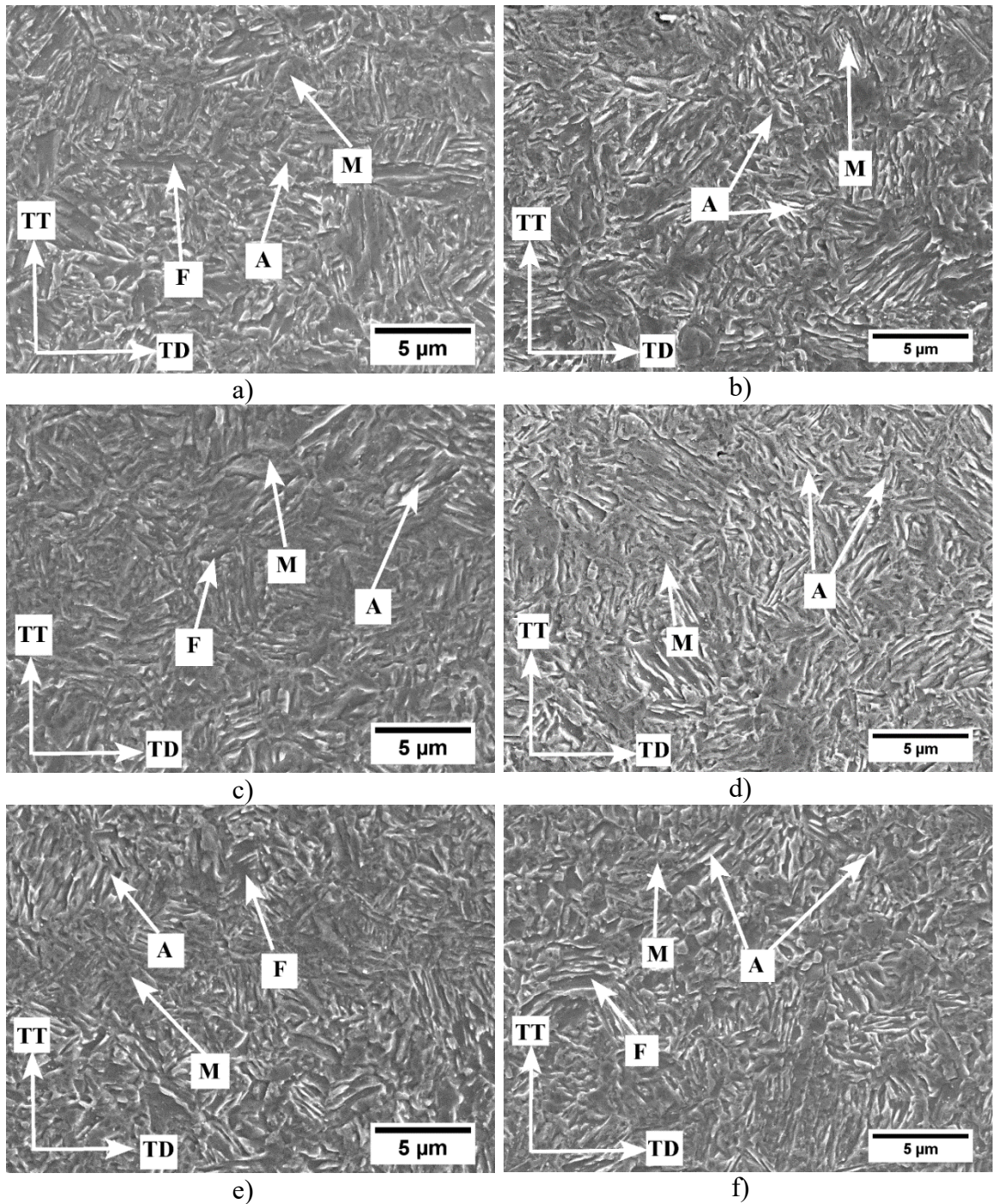


Figure 5.6: SEM micrographs of S-M samples subjected to 675°C IAT for a) 60s, b)

120s, c) 240s, d) 360s, e) 480s and f) 600s.

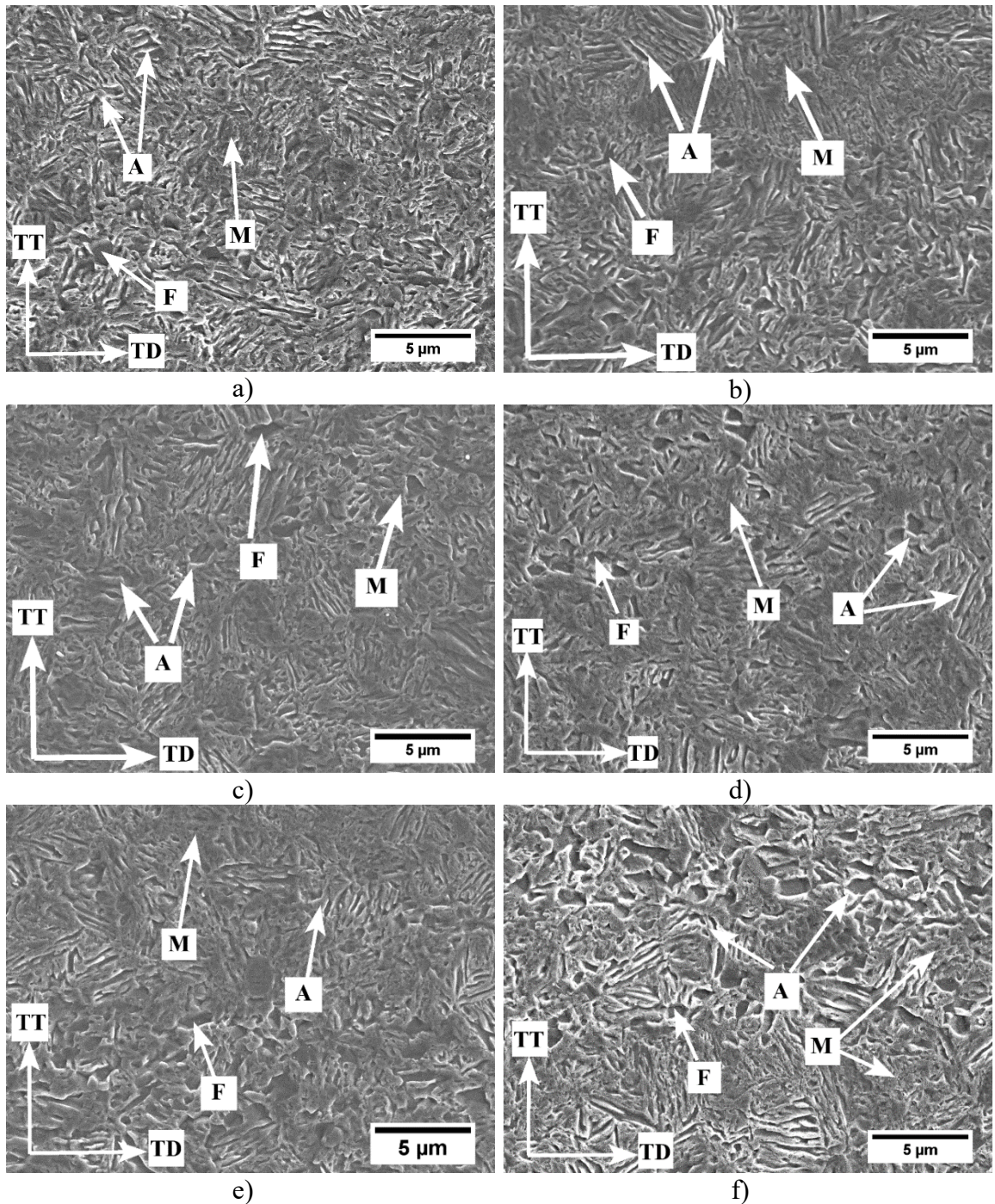


Figure 5.7: SEM micrographs of S-M samples subjected to 710°C IAT for a) 60s, b)

120s, c) 240s, d) 360s, e) 480s and f) 600s.

### 5.1.3 Microstructural Characterization by TEM

Fine scale microstructural analysis was conducted for selected S-M samples using transmission electron microscopy (TEM). Both bright and dark field images provided a better insight regarding the ultrafine grained microstructures of the annealed samples.

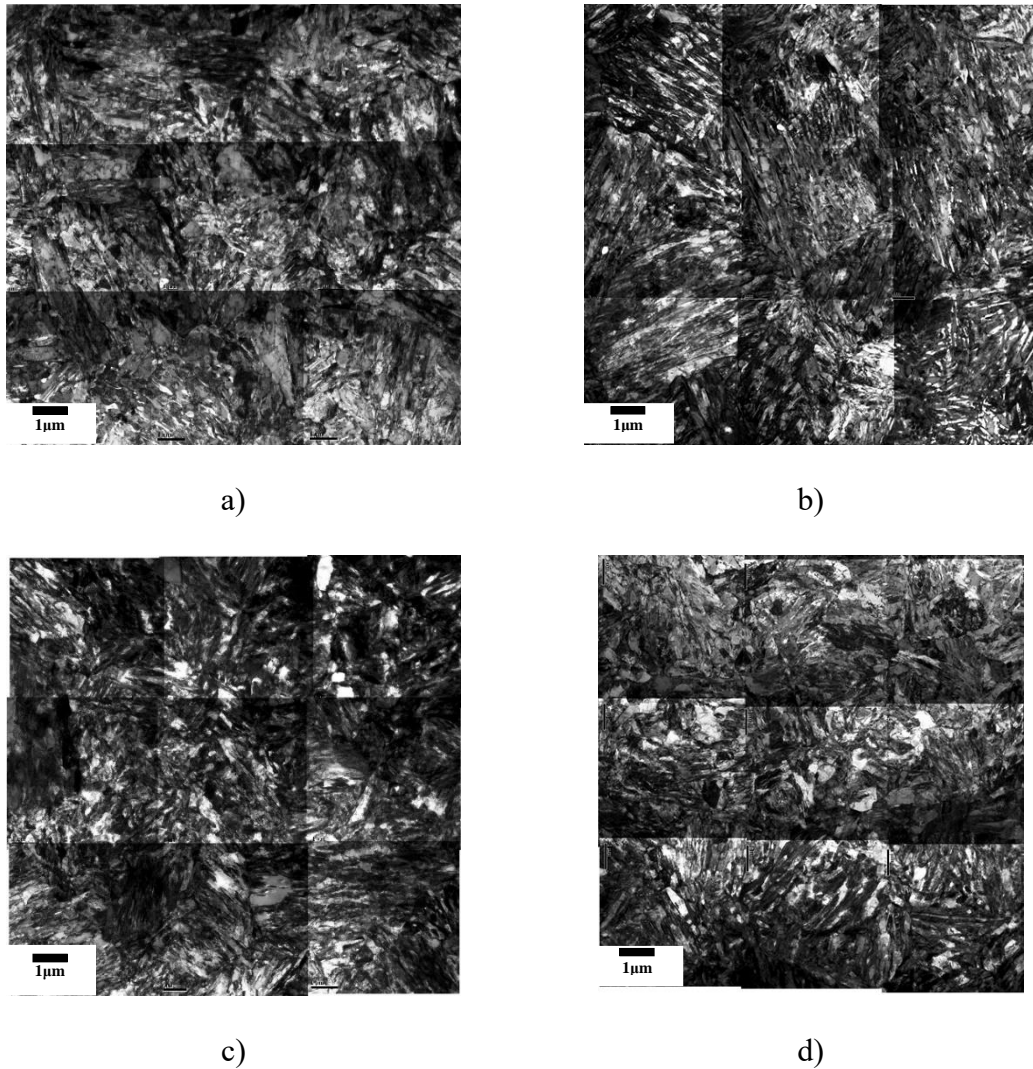
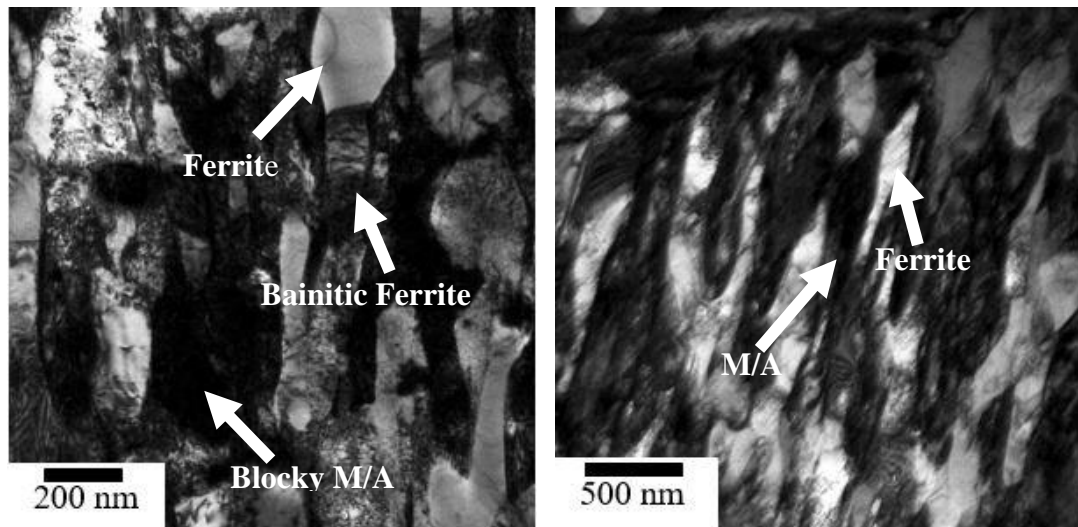


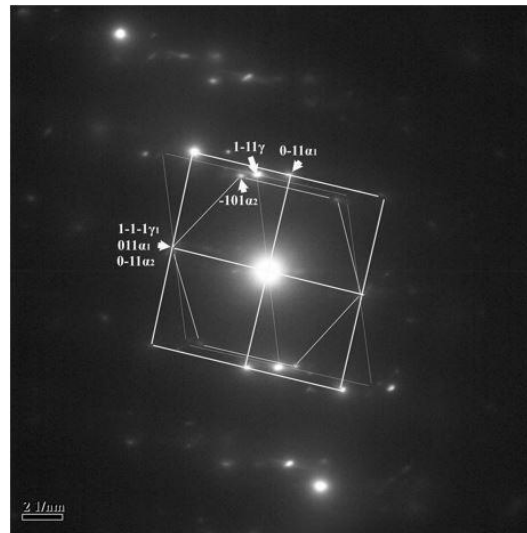
Figure 5.8: Montage of bright field (BF) TEM micrographs at lower magnification for S-M samples annealed at the 675°C IAT for a) 120s, b) 480s and at the 710°C IAT for c) 60s, d) 360s.

A low magnification montage of multiple bright field (BF) images for various annealing conditions is shown in Figure 5.8. A complex mixture of different ultrafine grained phase constituents as well as particles was observed in these microstructures.



a)

b)



c)

Figure 5.9: Bright field TEMs showing different morphologies of ferrite/bainitic ferrite, martensite and retained austenite in S-M 675°C + 600s sample.

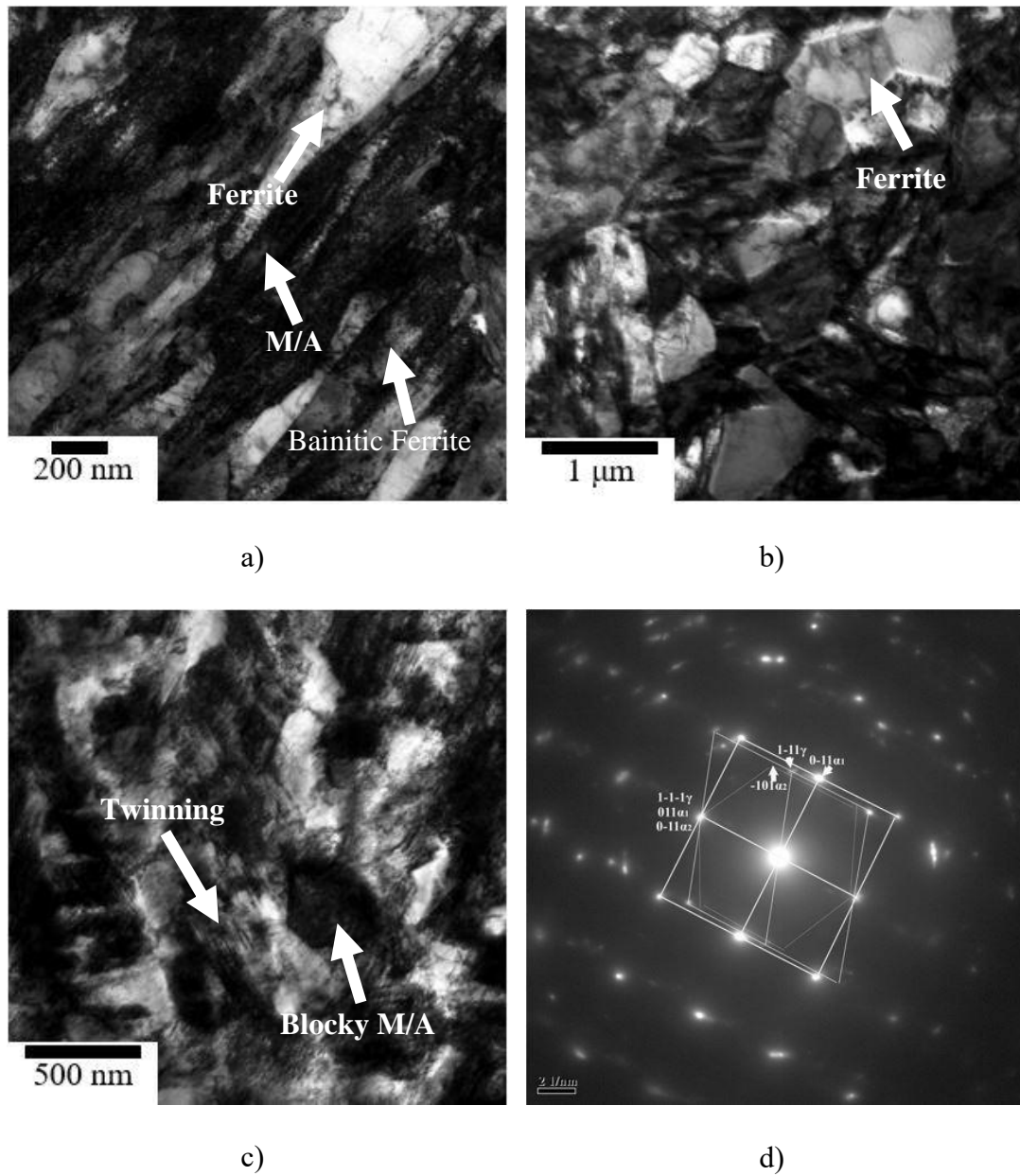


Figure 5.10: Bright field TEMs showing different morphologies of ferrite/bainitic ferrite, martensite and retained austenite in S-M 710°C + 600s sample.

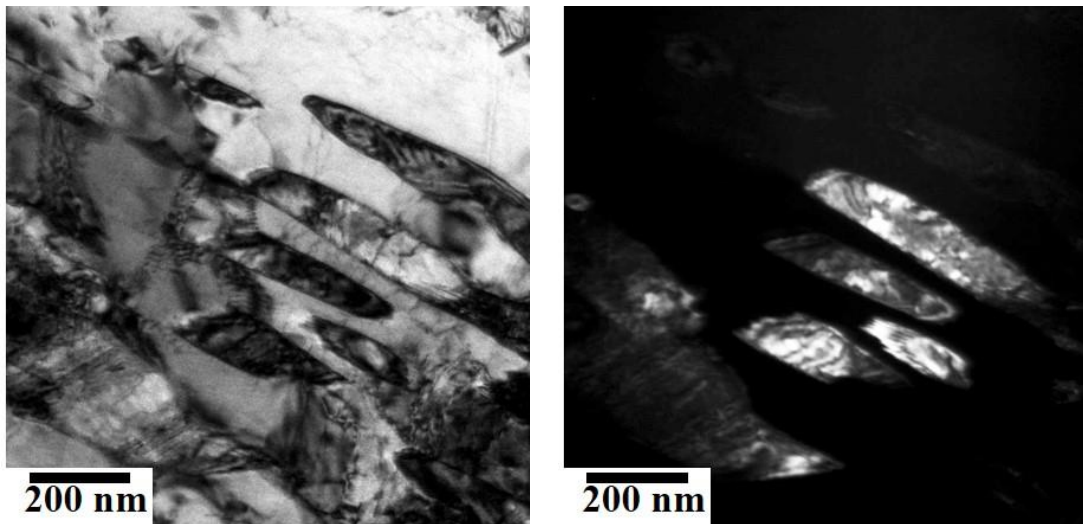
Bright field (BF) TEM micrographs at higher magnification revealed various microstructural constituents. TEM micrographs of S-M samples annealed at the 675°C IAT for 600s and at the 710°C IAT for 600s are shown in Figure 5.9 and Figure 5.10,

respectively, which highlight the different morphologies of various phases. Figure 5.9 shows a series of multiphase microstructures mainly consisting of lath-shaped ferrite that had a lower dislocation density and bainitic ferrite which had a higher dislocation density alongside martensite/austenite (M/A) phases that were also present as laths (Figure 5.9 a) and b)) in S-M sample annealed at the 675°C IAT for 600s. A small fraction of irregular (or quasi-polygonal) non-parallel shaped ferrite was also observed (Figure 5.9 a)). Moreover, M/A was also observed as dispersed block shaped islands in some of the S-M samples, as shown in Figure 5.9 a).

For the S-M samples which were annealed at 710°C for 600s, similar microstructures were observed, as shown in Figure 5.10. However, some minor differences were noted. The amount of martensite was higher in the samples annealed at the 710°C IAT (Figure 5.10 a)), consistent with the XRD results (Figure 5.3). Some equiaxed ferrite grains were also observed, as shown in Figure 5.10 b). Moreover, internally twinned martensite blocks were identified in these S-M samples (Figure 5.10 c)).

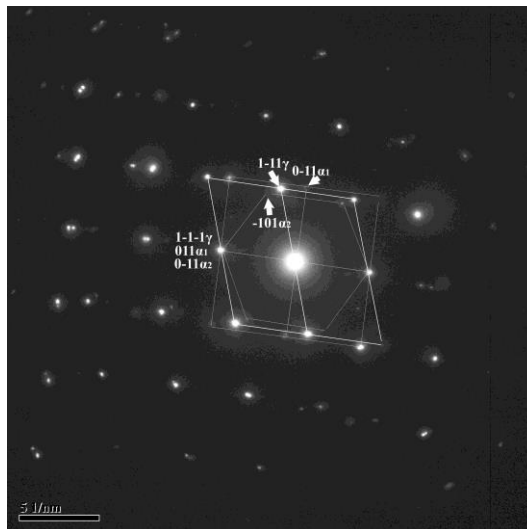
Dark field (DF) and selected area diffraction (SAD) were carried out in order to identify the phases based on their crystal structures. The  $\langle 111 \rangle \alpha$ ,  $\langle 100 \rangle \alpha$  ferrite and  $\langle 110 \rangle \gamma$  austenite diffraction patterns were taken from the annealed samples. The S-M sample annealed at 675°C IAT for 120s consisted of lath-shaped retained austenite, as shown in Figure 5.11b). This type of retained austenite is known to be more chemically stable compared to blocky retained austenite [10] [65]. Figure 5.12 and Figure 5.13 show the results for S-M samples annealed at 675°C IAT for 480s and 710°C IAT for 360s, respectively. It was determined by DF imaging that some laths exhibited  $\langle 111 \rangle \alpha$  orientation

whereas other laths had  $\langle 100 \rangle \alpha$  orientation. M/A constituents in the form of thin films were observed between ferrite laths or acicular shaped grains as the diffraction and DF image suggested.



a)

b)



c)

Figure 5.11: a) Bright field (BF) TEM, b) dark field (DF) TEM corresponding to  $\langle 110 \rangle \gamma$  and c) SAD patterns of S-M 675°C + 120s sample.

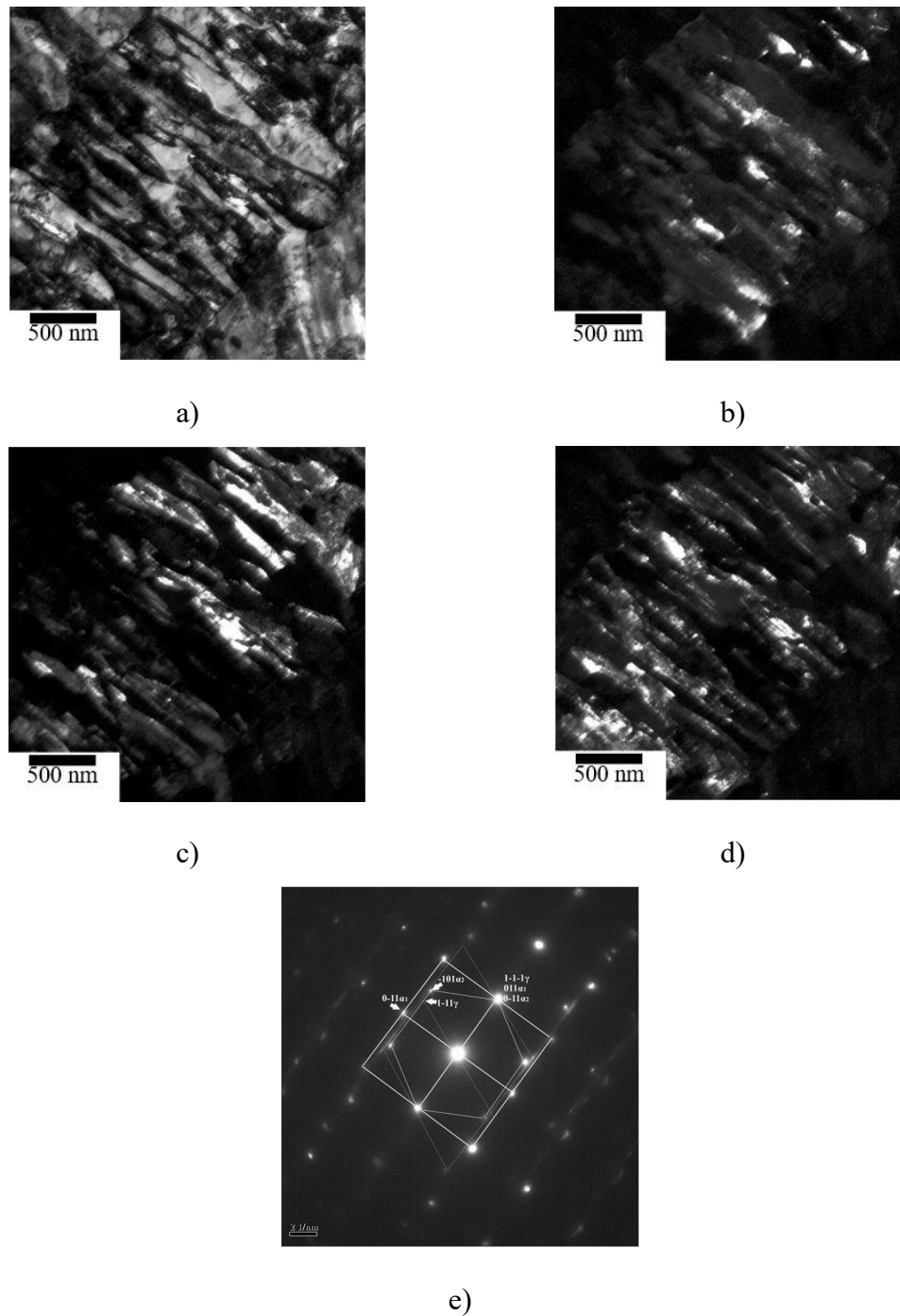


Figure 5.12: a) Bright field (BF) TEM; dark field (DF) TEM corresponding to b)  $\langle 111 \rangle \alpha$ , c)  $\langle 100 \rangle \alpha$ , d)  $\langle 110 \rangle \gamma$  and e) SAD patterns of S-M 675°C + 480s sample.

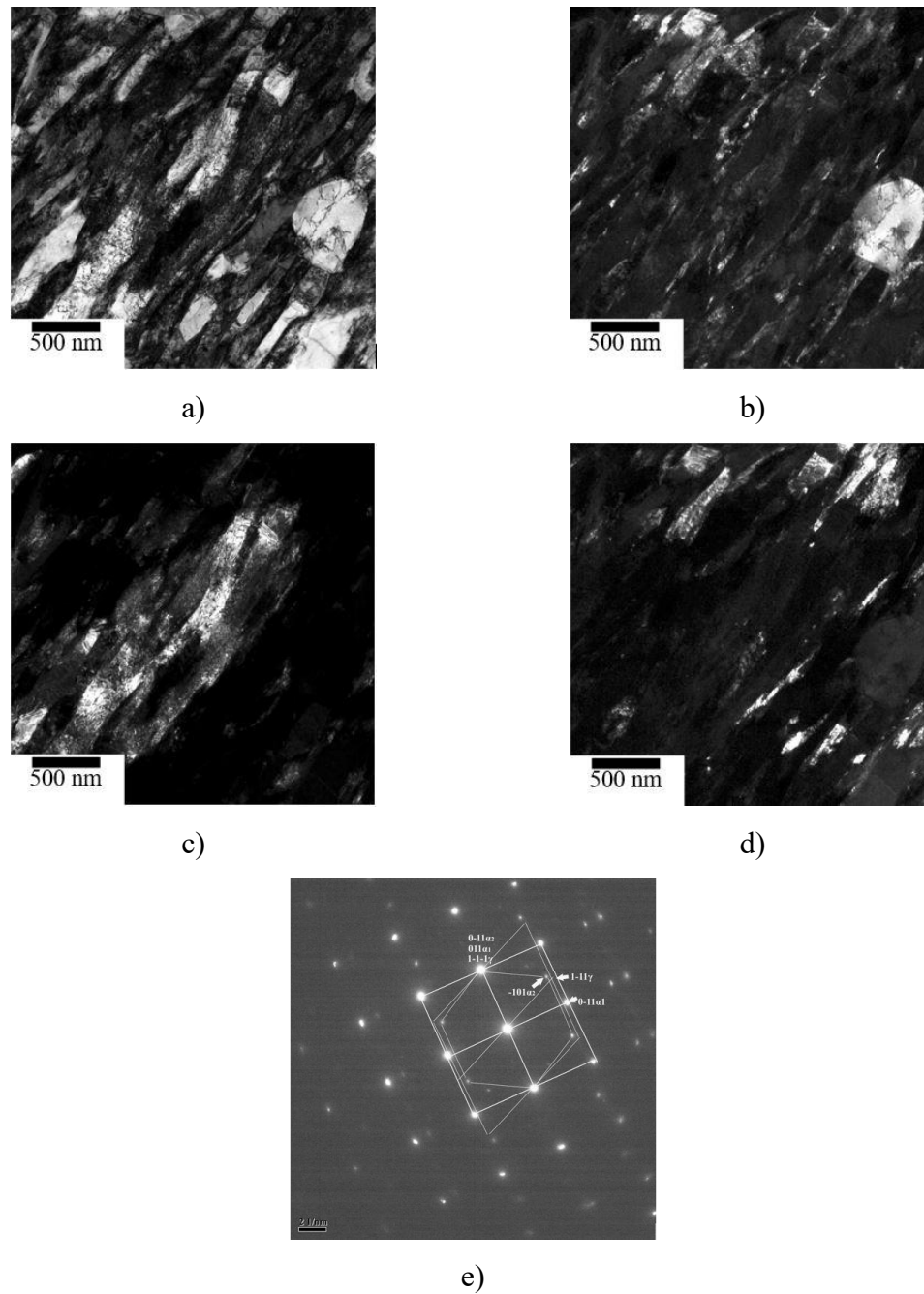


Figure 5.13: a) Bright field (BF) TEM; dark field (DF) TEM corresponding to b)  $\langle 111 \rangle \alpha$ , c)  $\langle 100 \rangle \alpha$ , d)  $\langle 110 \rangle \gamma$  and e) SAD patterns of S-M 710°C + 360s sample.

DF and SAD pattern in Figure 5.12 indicated that there were two ferrite zone axes,  $\langle 100 \rangle \alpha_1$  and  $\langle 111 \rangle \alpha_2$ , and a single retained austenite  $\langle 110 \rangle \gamma$  zone axis. Hence, two different orientation relationships were observed, as shown in Figure 5.14. The OR between  $\alpha_1$  ferrite and retained austenite, which was  $[100] \alpha_1 \parallel [110] \gamma$  and  $(011) \alpha_1 \parallel (1\bar{1}\bar{1}) \gamma$ , closely corresponds to the Nishiyama-Wasserman (N-W) orientation relationship (Figure 5.14b)). On the other hand, the OR for  $\alpha_2$  ferrite and retained austenite, which was  $[111] \alpha_2 \parallel [110] \gamma$  and  $(011) \alpha_2 \parallel (1\bar{1}\bar{1}) \gamma$ , corresponded to the Kurdjumov-Sacks (K-S) orientation relationship (Figure 5.14c)).

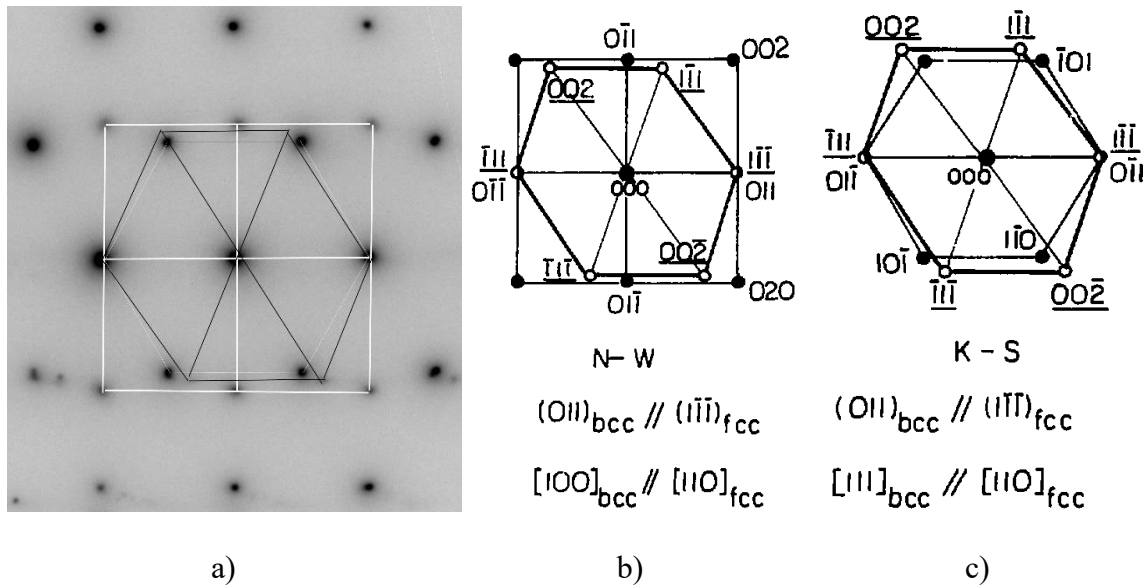


Figure 5.14: SAD pattern (a) and schematic representation of SAD patterns for b) N-W and c) K-S orientation relationship [66].

Another important observation of the TEM micrographs was the presence of carbide particles in the microstructures. Figure 5.15 shows typical carbide particles present in the S-M 675°C + 480s sample with their corresponding SAD patterns. SAD pattern analysis

[67] of the carbide particles indicated that they had a face centered cubic (FCC) structure with a lattice parameter of approximately 1.062 nm. Based on this analysis, it was concluded that the particles were  $M_{23}C_6$ -type carbides. STEM + EDS in the JEOL 2010F TEM were utilized for chemical analysis of the carbides. Multiple (at least 15) particles were analyzed to determine an average composition of the carbides. It was determined that the particles were Cr- and Mn-rich with some Fe, Si and Al, as identified by EDS. Figure 5.16 and Figure 5.17 show the EDS spectra of the particle and the adjacent matrix for two S-M samples annealed at an IAT of 675°C for 480s and 710°C for 360s, respectively. By comparing the results from these two spot analyses, an approximate particle composition was obtained. The particle analysis had higher concentrations of Cr and Mn. On the other hand, the Cr and Mn concentrations decreased significantly and the concentration of Fe increased for the adjacent matrix analysis. Thus, it was concluded that the particles were Cr and Mn-rich carbides, consistent with the SAD-based identification of  $M_{23}C_6$  type, as shown in the previous section. The composition of the particles and the matrix are listed in Table 5.1. Moreover, high concentrations of Ti with some Mo were observed in some particles, as shown in Figure 5.18.

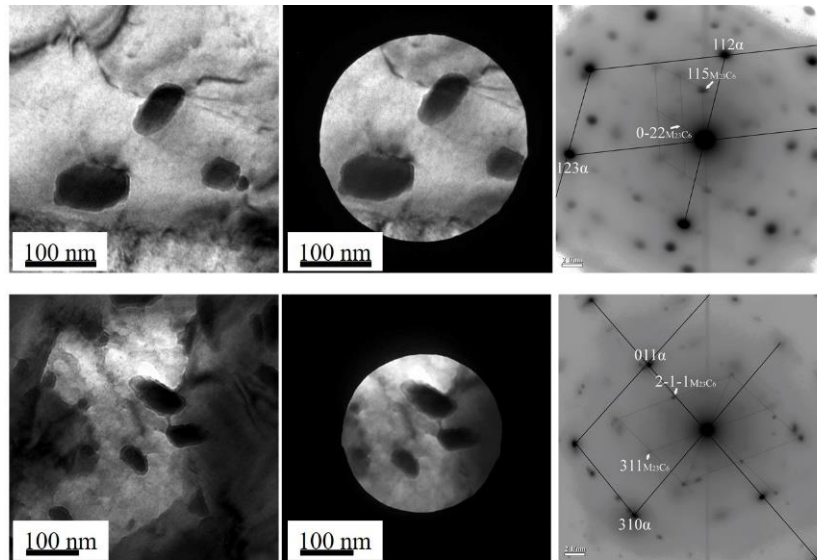


Figure 5.15: Particles and their corresponding SAD patterns of S-M sample annealed at 675°C IAT for 480s.

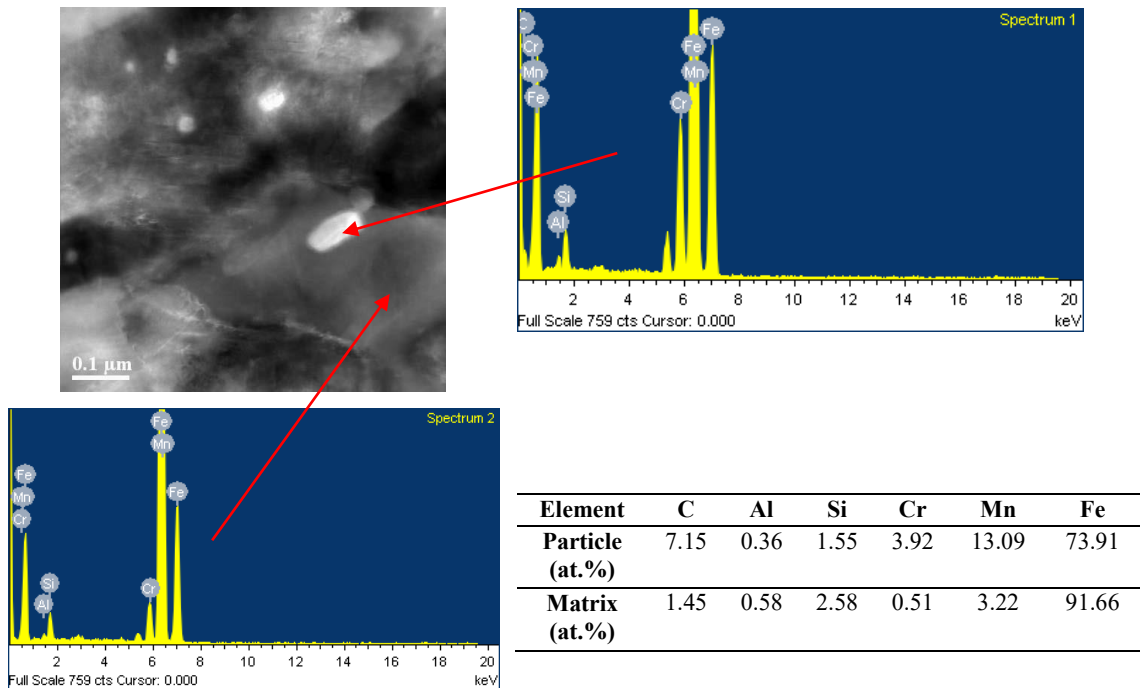


Figure 5.16: EDS spectra of the particle and the matrix of the S-M 675°C + 480s sample.

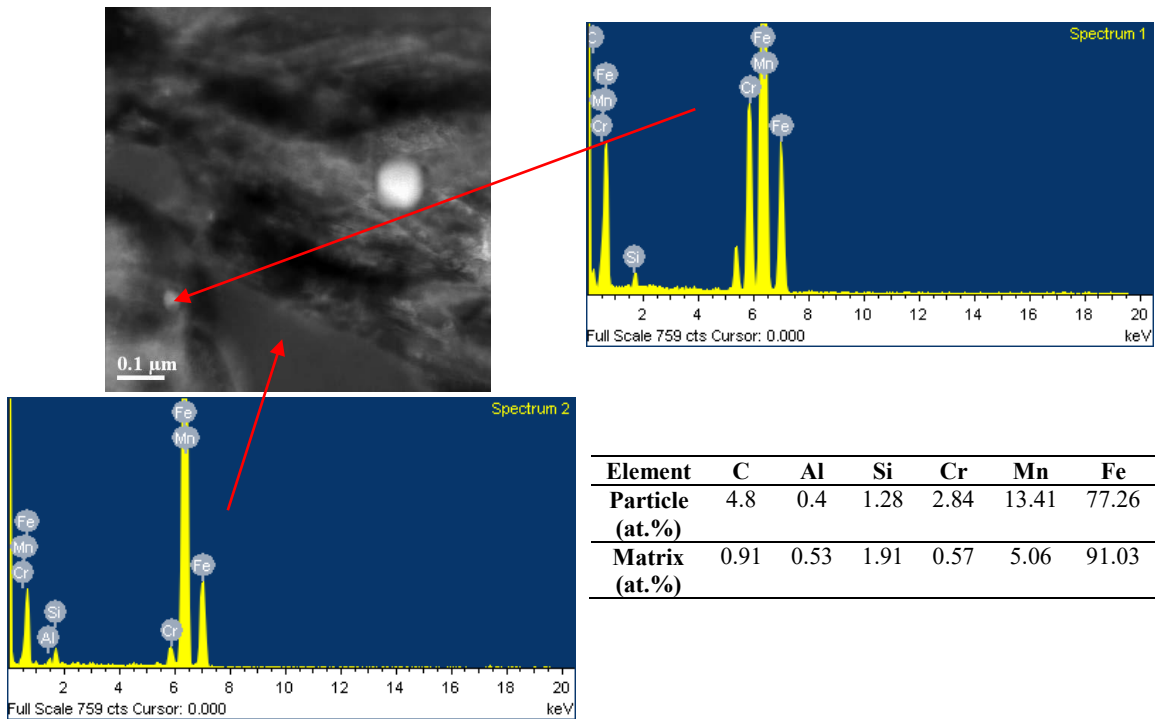


Figure 5.17: EDS spectra of the particle and the matrix of the S-M 710°C + 360s sample.

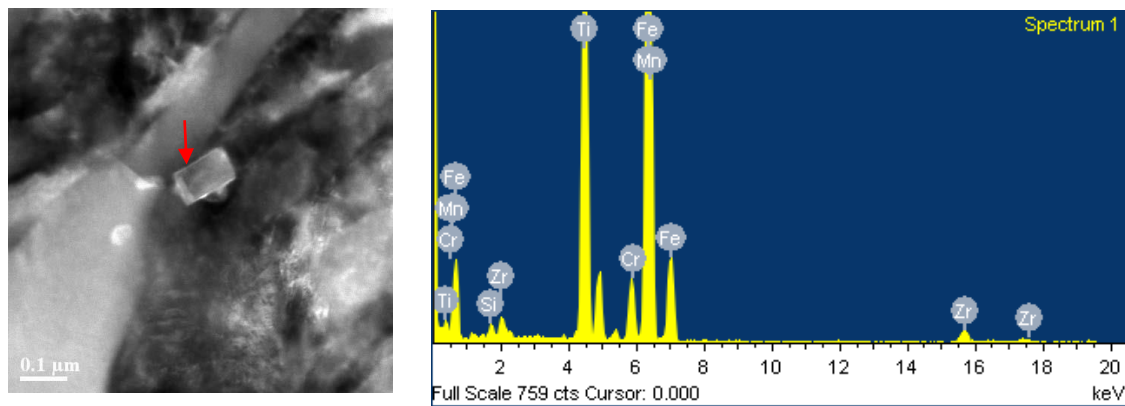


Figure 5.18: EDS spectra of a titanium-rich particle of an S-M 710°C + 600s sample.

Table 5.1 Average Particle and Matrix Composition from EDS Spot Analysis (at.%)

<b>Element</b>	C	Al	Si	Ti	Cr	Mn	Fe	Ratio of (Cr+Mn)/ C
<b>Sample</b>								
<b>Particle</b>								
675°C for 480s	4.79	0.55	1.78	0.04	<b>2.84</b>	<b>12.98</b>	77.02	3.31
675°C for 600s	7.99	1.85	2.43	0.03	<b>2.33</b>	<b>11.43</b>	73.93	1.72
710°C for 360s	3.18	0.57	1.48	0.02	<b>3.03</b>	<b>11.25</b>	80.47	4.48
710°C for 600s	7.93	0.47	1.98	0.03	<b>2.79</b>	<b>12.16</b>	74.67	1.88
<b>Matrix</b>								
675°C for 480s	0.32	0.67	2.71	0	0.60	3.80	91.90	
675°C for 600s	1.44	0.68	3.67	0	0.57	5.22	88.42	
710°C for 360s	0.91	0.53	1.98	0	0.51	5.06	91.03	
710°C for 600s	1.04	1.04	3.16	0	0.48	4.32	89.96	

The ratio of (Mn + Cr)/C in the carbide particles of the samples annealed for 675°C for 480s and 710°C for 360s (Table 5.1) is reasonably close to the theoretical ratio  $M_{23}/C_6 = 23/6 = 3.8$ . However, the ratio of M/C was less consistent with the theoretical ratio in the carbides of the samples annealed for longer times (e.g. 675°C for 600s and 710°C for 600s). The errors associated with EDS analysis of light elements, particularly C, are large. This might be the reason for inconsistent ratio of (Mn + Cr) to C in those carbides.

#### 5.1.4 Mechanical Properties

Tensile tests were conducted on the as-received and annealed samples which contained significant volume fractions of retained austenite. The resultant engineering stress-engineering strain and true stress-true strain curves are shown as a function of IA temperature and holding time in Figure 5.19 and the tensile property results are summarized in Table 5.2. In all cases, the UTS × TE product was assessed with respect to target

mechanical properties for 3G-AHSSs [14] to determine the optimal heat treatment conditions.

The as-received samples had a high ultimate tensile strength (UTS) and a low total elongation (TE) which resulted in a low  $UTS \times TE$  product of 10,933 MPa% (Table 5.2). However, a decrease in yield and ultimate tensile strength and an increase in total elongation with increasing holding time at 710°C IAT were observed for the annealed S-TM samples, as shown in Figure 5.20. The highest total elongation was observed for the sample annealed at 710°C IAT for 600s, which was over 20%. This was probably due to plasticity enhancing effect (TRIP/TWIP) that resulted from the significant volume fraction of retained austenite in this sample (i.e. 0.37 vol. fraction, as shown in Figure 5.1). The  $UTS \times TE$  product for this sample was 30,456 MPa%. However, the relatively long IA holding time of 600s required to produce these properties is not consistent with desired CGL thermal processing conditions as the steel substrate usually resides only a total of 3-5 minutes in the CGL furnace.

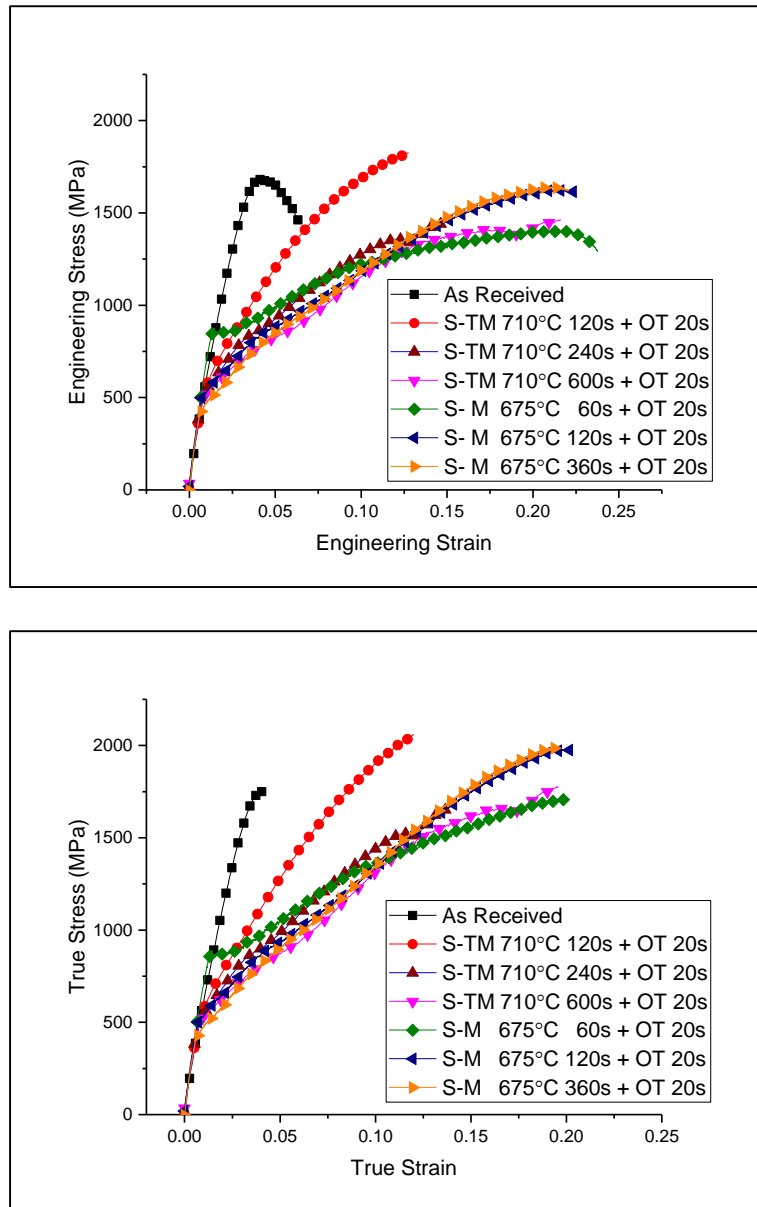


Figure 5.19: Engineering stress vs engineering strain and true stress vs true strain curves for selected as-received and heat treated S-TM and S-M samples.

Table 5.2 Summary of the Mechanical Properties (Engineering Stress vs Strain)

Sample ID	Yield Strength, YS (MPa)	Ultimate Tensile Strength, UTS (MPa)	Total Elongation, TE (%)	UTS×TE (MPa %)
As Received	1100	1682	6.5	<b>10,933</b>
S-TM 710°C + 120s	600	1828	11.4	<b>20,839</b>
S-TM 710°C + 240s	540	1458	13.6	<b>19,828</b>
S-TM 710°C + 600s	480	1410	21.6	<b>30,456</b>
S-M 675°C + 60s	850	1390	22.2	<b>30,858</b>
S-M 675°C + 120s	490	1640	22.6	<b>37,064</b>
S-M 675°C + 360s	410	1590	21.8	<b>34,662</b>

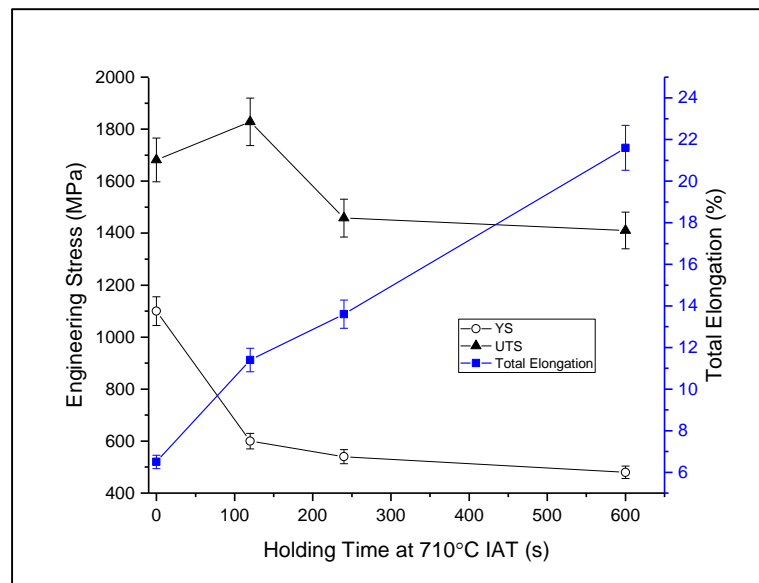


Figure 5.20: Summary of S-TM sample engineering stress-strain mechanical properties as a function of 710°C IAT time.

However, in the case of the martensitic starting microstructure (S-M) samples, 3G-AHSS compatible properties were achieved using the lower 675°C IAT at much shorter times (Figure 5.19 and Table 5.2) versus the S-TM microstructures. This might be attributed to faster austenite reversion transformation kinetics with a martensitic starting microstructure at the IAT. These results are also consistent with the results observed by Luo and Dong [22] for their TRIP steels with martensitic starting microstructure. From Figure 5.21, it can be seen that the yield strength decreased whereas the UTS increased with increasing holding time at 675°C IAT for these S-M samples. However, it can also be seen that the total elongation did not change significantly with increasing holding time at IAT and remained over 20% for all of the selected S-M samples (Figure 5.21). This resulted in a high UTS × TE product (> 30,000 MPa%) in these S-M samples (Table 5.2). The highest UTS × TE product was observed for the S-M 675°C + 120s samples with 20s OT time, which was 37,064 MPa% (Table 5.2).

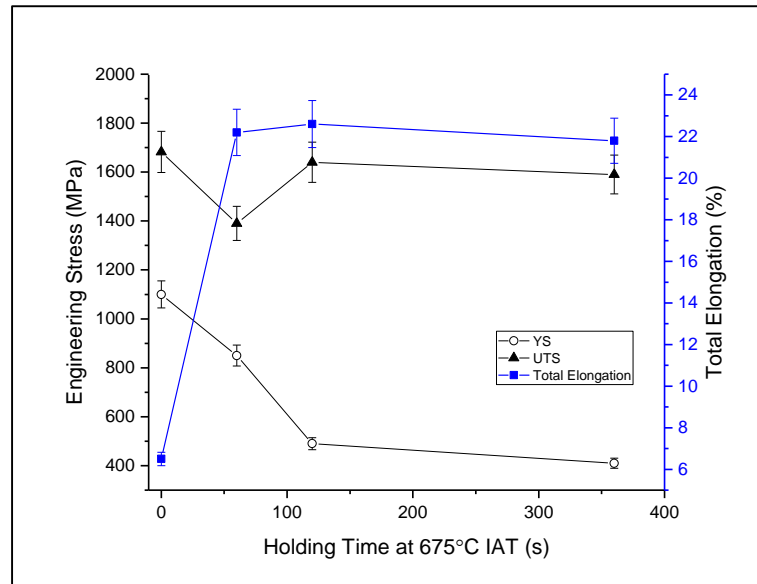
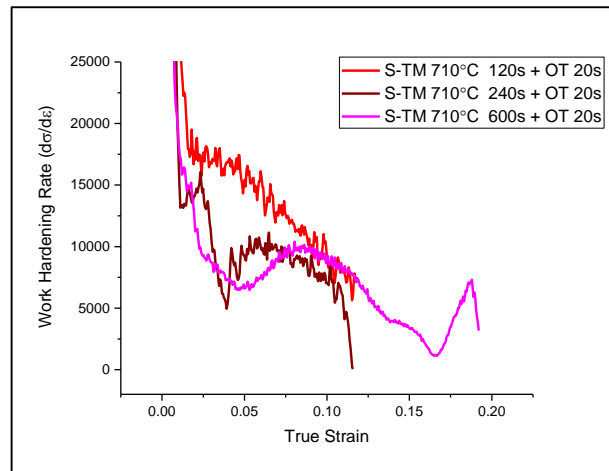


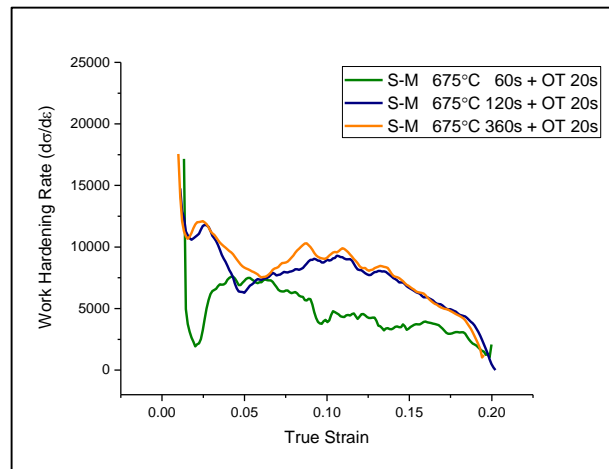
Figure 5.21: Summary of S-M sample engineering stress-strain mechanical properties as a function of 675°C IAT time.

The true stress-true strain results were used in determining the instantaneous work hardening rate ( $d\sigma/d\varepsilon$ ) during the tensile tests, which was then plotted as a function of true strain. The results are shown in Figure 5.22. Two different trends were observed in Figure 5.22. One was for the S-TM 710°C + 120s sample where the work hardening rate decreased with increasing strain to failure, as shown in Figure 5.22a). This is a typical work hardening curve for a dual phase (DP) steel which does not exhibit the transformation induced plasticity (TRIP) effect [20]. However, the S-TM 710°C + 240s and S-TM 710°C + 600s samples showed a different trend (Figure 5.22 a)). The work hardening rate initially decreased followed by a gradual increase in work hardening rate with increasing strain up to a certain strain ( $\varepsilon = 0.08$  and  $\varepsilon = 0.10$  for the S-TM 710°C + 240s and S-TM 710°C + 600s samples, respectively). Finally, the work hardening rate decreased with further increases in strain to failure. This type of work hardening rate trend is consistent with steel

which has sufficient amount of stable retained austenite that exhibits the TRIP effect during deformation [10] or an austenitic steel that shows the Twinning Induced Plasticity (TWIP) effect [11]. The XRD analysis of these annealed samples (Figure 5.1) have revealed a sufficient amount of retained austenite in them which gradually transformed to martensite during deformation and maintained a high work hardening rate at high strains.



a)



b)

Figure 5.22: Work hardening rate vs true strain for selected a) S-TM and b) S-M samples.

The S-M samples, as shown in Figure 5.22 b), also followed a similar trend as the annealed samples had more than 0.30 volume fraction retained austenite (Figure 5.2) which resulted in the TRIP or TWIP effect that delayed the onset of necking during deformation by maintaining high work hardening rate at high strains. This is consistent with the results observed by Lee et al. [21] and Shi et al. [46].

Another important feature of the work hardening curves, as shown in Figure 5.22, was the Portevin-Le Chatelier (PLC) effect which suggests dynamic strain aging after elastic deformation. Unstable plastic flow results in such deformation and is known to originate from the interaction between dislocations and solute (interstitial and substitutional) atoms. Ghasri-Khouzani [68] observed similar PLC effect in high Mn TWIP steel with high (0.4-0.6 wt.%) C content. The XRD results (Figure 5.1 and Figure 5.2) showed that retained austenite C content was approximately 0.45 – 0.60 (wt.%) for the annealed S-TM and S-M samples which was sufficient to result in the observed PLC effect.

### ***5.1.5 Interrupted Tensile Tests***

Interrupted tensile tests were conducted on the S-M samples annealed at the 675°C IAT for 60s and 120s. The results are shown in Figure 5.23. These two conditions were chosen as they are compatible with normal CGL processing parameters and yielded a >30,000 MPa% UTS × TE product from mechanical testing. The retained austenite transformation kinetics followed the same trend in both S-M samples. From Figure 5.23, it can be seen that the retained austenite transformation rate was rapid at lower strains, however, in both cases a relatively gradual transformation of retained austenite was observed with increasing strain to failure. A similar gradual transformation of retained

austenite was observed by McDermid et al. [10] for a low-alloy TRIP-assisted steel. This suggested that most of the retained austenite was chemically and mechanically stable, which resulted in gradual transformation to martensite with increasing strain.

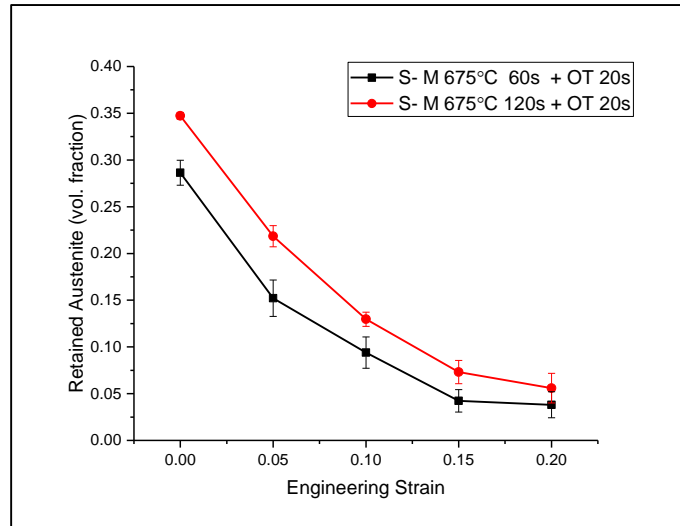


Figure 5.23: Retained austenite transformation kinetics of S-M 675°C IAT samples with 20s OT holding time.

### 5.1.6 Fractography

Fracture surfaces of selected S-TM and S-M tensile samples was analyzed using the JEOL 6610-LV SEM to determine the mode of fracture. SEM micrographs of the fracture surface are shown in Figure 5.24. Ductile tearing and significant grain pull-out were observed in the as-received sample (Figure 5.24a)), which suggested that the fracture mechanism was classic void nucleation and coalescence along the grain boundaries. In addition, multiple microvoids and microcracks formed in all of the fractured samples, circled in red in Figure 5.24, supporting this hypothesis. Microvoids generally form at the interface of a softer and a harder phase in multi-phase ferrous alloys such as dual phase

steels. In this case, the softer phase might be ferrite/bainitic ferrite or softer martensite (lower hardness) while the harder phase might have been martensite (higher hardness). These microvoids likely subsequently coalesced and formed microcracks to result in sample failure.

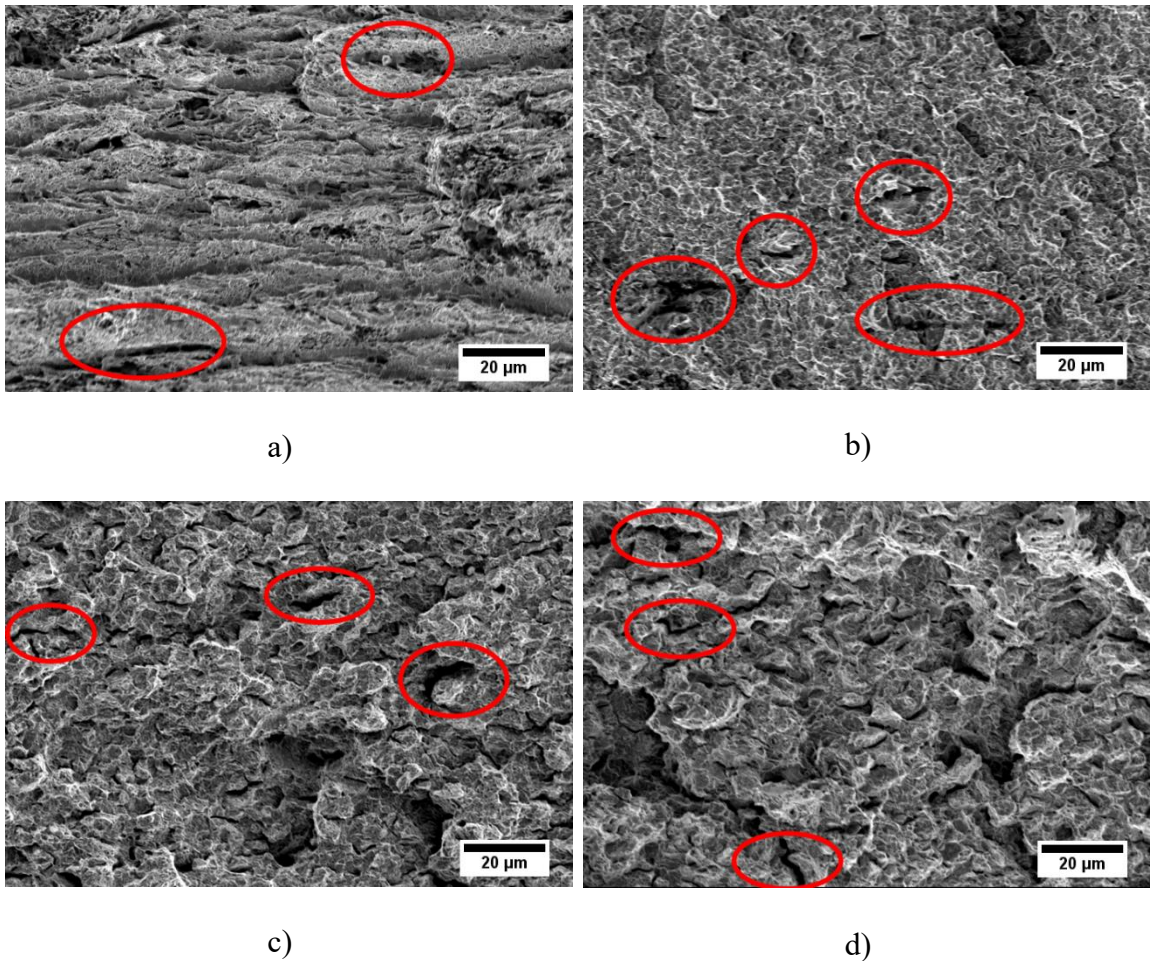


Figure 5.24: Fracture surface micrographs of a) as received, b) S-TM 710°C + 600s; c) S-M 675°C + 60s and d) S-M 675°C + 120s samples where the microcracks are shown using red circles.

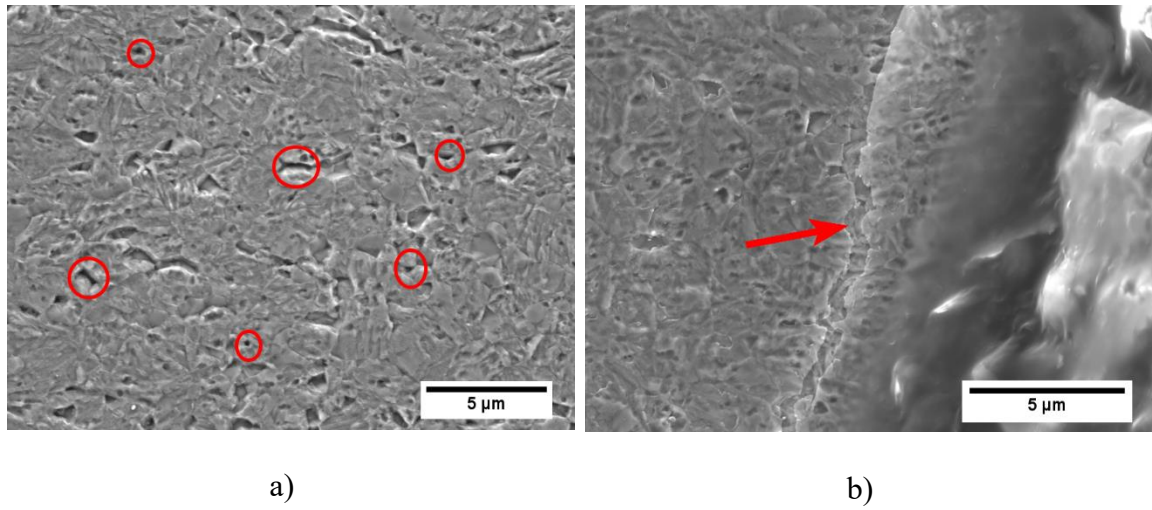


Figure 5.25: Cross-section near fracture surface of the S-TM 710°C + 600s sample where the microvoids and microcracks are shown in red circles and red arrow, respectively.

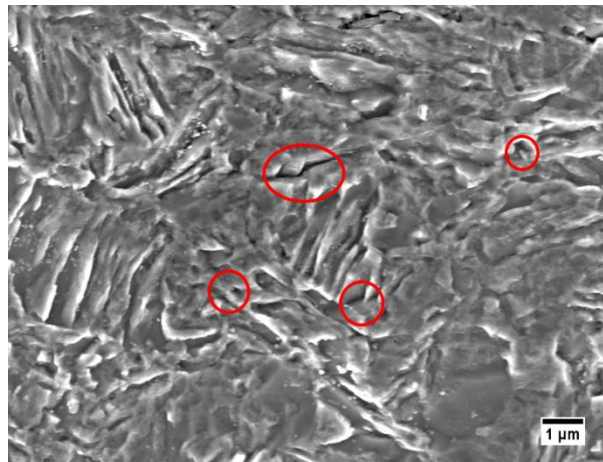


Figure 5.26: Cross-section near fracture surface of the S-M 675°C + 120s sample where microcracks are shown using red circles.

Sample cross-sections near the fracture surface were also analyzed with SEM to identify the dominant fracture mechanism. Figure 5.25 shows the SEM micrographs of the fractured S-TM 710°C + 600s sample. Microvoids and microcracks were observed in Figure 5.25 a). Moreover, a microcrack was observed near the fracture surface which

propagated along the grain boundaries, as shown in Figure 5.25 b) with a red arrow. Similar microcracks and microvoids were also observed in the cross-sectional SEM of the S-M 675°C + 120s sample, as shown in Figure 5.26. Moreover, decohesion of the matrix from inclusions was also observed near the fracture surface, as confirmed by EDS mapping for all samples. Figure 5.27 shows the EDS maps for the S-M 675°C + 120s sample, showing decohesion of the matrix from a MnS inclusion.

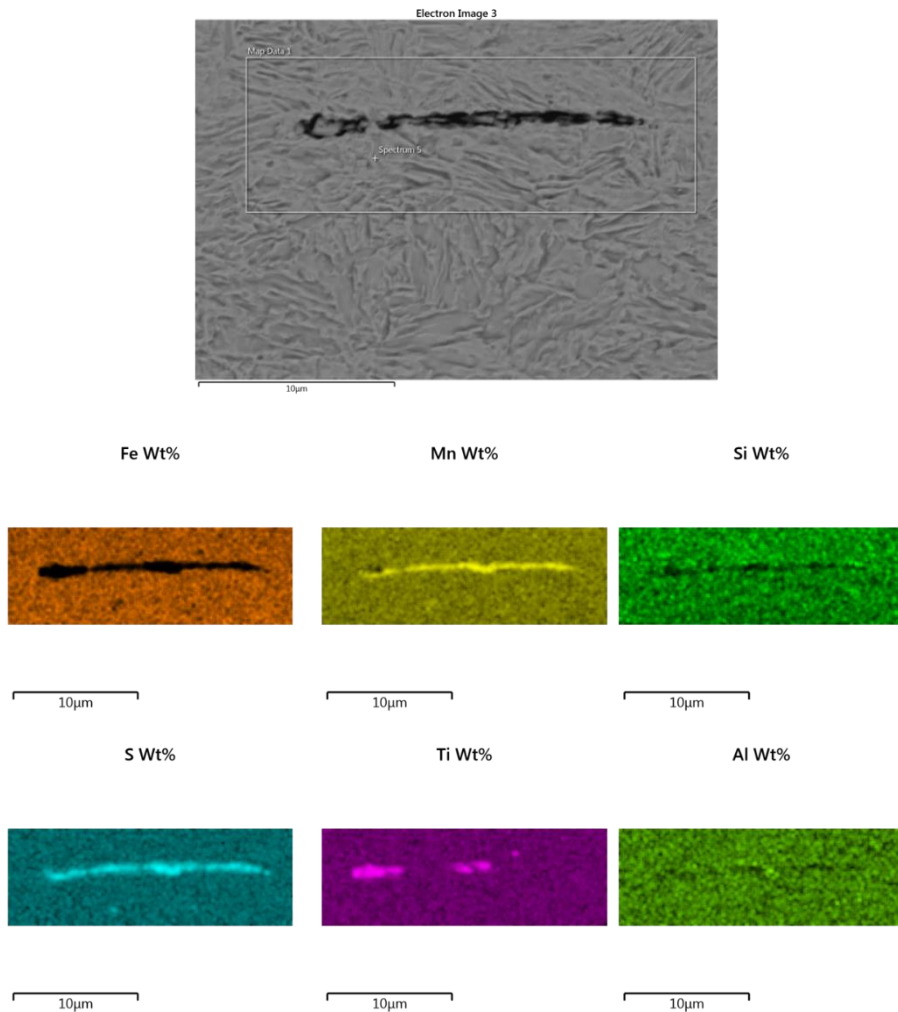
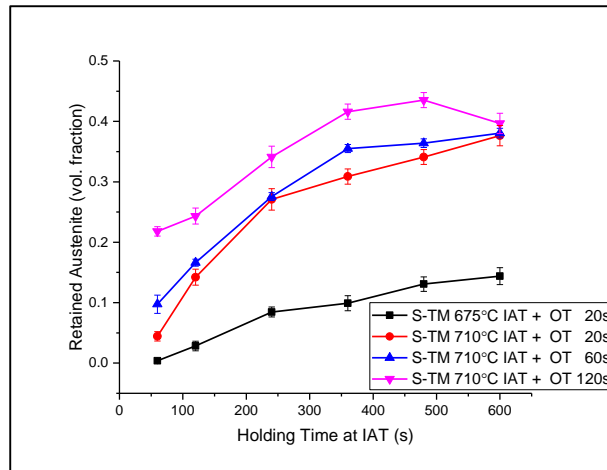


Figure 5.27: EDS mapping of the area showing decohesion of inclusion in S-M 675°C + 120s sample.

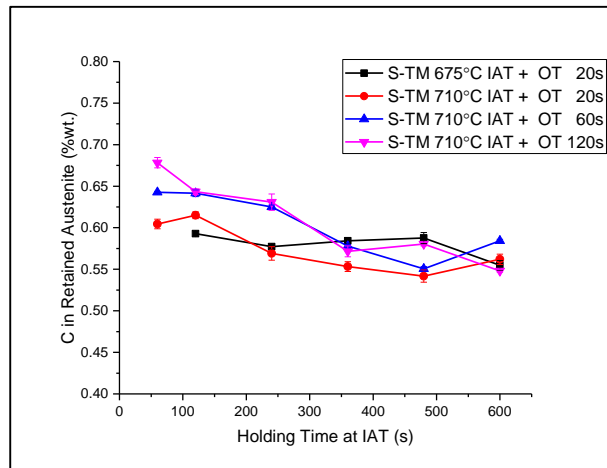
## **5.2 Effect of Overaging Temperature Holding Time**

### **5.2.1 XRD Results**

Both S-TM and S-M samples were annealed using a 60s and 120s OT holding time in order to determine the effect of OT holding time on retained austenite stability and mechanical properties. The annealed samples were analyzed using XRD and the retained austenite volume fraction results are shown in Figure 5.28 and Figure 5.29. The S-TM 710°C IAT samples showed a significant increase in retained austenite volume fraction for IAT holding times up to 480s and a similar fraction for the 600s IAT holding time with the 60s and 120s OT holding times compared to the baseline 710°C IAT + 20s OT samples. In this case, the retained austenite volume fraction was always higher for 60s and 120s OT holding times versus the 20s OT baseline samples. The highest volume fraction of retained austenite was observed for samples annealed at the 710°C IAT for 480s with a 120s OT treatment. It should be noted that the retained austenite C content of the 60s and 120s OT holding time samples did not change significantly versus the baseline 710°C IAT + 20s OT samples, as shown in Figure 5.28 b).



a)

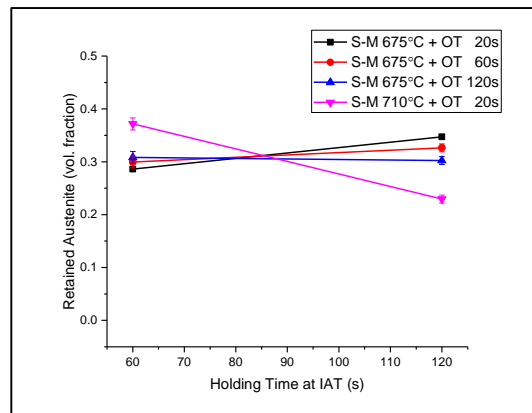


b)

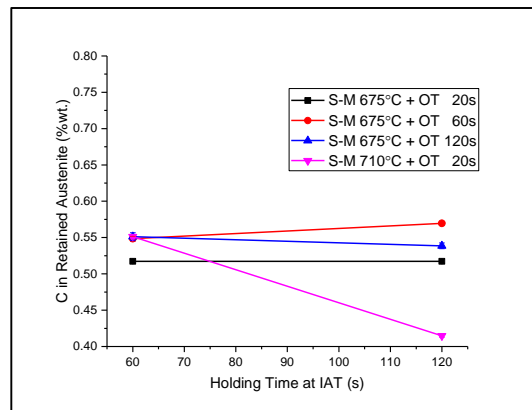
Figure 5.28: a) Retained austenite volume fraction and b) C content in retained austenite as a function of OT holding time for S-TM samples.

The S-M samples showed a different trend with increasing OT holding time compared to S-TM samples, as shown in Figure 5.29. The retained austenite volume fraction did not change significantly with OT holding time for both the S-M 675°C + 60s and S-M 675°C +120s IAT heat treatments. Moreover, there was not any significant change in retained austenite C content for both S-M samples at 675°C IAT regardless of OT holding times, as

shown in Figure 5.29 b). This suggested that C was no longer partitioning into the remaining untransformed austenite at the 460°C OT. Moreover, the retained austenite volume fraction decreased significantly with increasing holding time for S-M 710°C IAT samples subjected to a 20s OT holding time (as shown in Figure 5.29a)). This is attributed to the C content in the retained austenite which decreased significantly with increasing holding time (60s to 120s) for S-M 710°C IAT samples (Figure 5.29 b)). Hence, chemical stability of the intercritical austenite decreased owing to the lower C content and resulted in the intercritical austenite transforming to martensite during final cooling (Figure 5.3).



a)



b)

Figure 5.29: a) Retained austenite and b) C content in retained austenite as a function of

OT holding time for S-M samples.

### **5.2.2 *Microstructural Characterization by SEM***

Scanning electron microscopy (SEM) was used to analyze the microstructures of the annealed samples. Micrographs of S-TM samples are shown in Figure 5.30 and Figure 5.31 for the 710°C IAT with 60s and 120s OT holding times, respectively. In both cases, as the IAT holding time increased, the amount of retained austenite increased and this phase was easier to identify in the SEM micrographs. The micrographs correlated well with the XRD results in Figure 5.28. The SEM observations confirmed the ultrafine grained complex microstructure of the annealed S-TM samples, similar to that observed for the 20s OT holding time S-M samples (Figure 5.6). Ferrite/bainitic ferrite, athermal martensite and retained austenite of different morphologies were observed.

S-M samples annealed with 60s and 120s OT holding times are shown in Figure 5.32. There were no significant differences in the microstructures of the S-M samples regardless of the annealing and OT treatment conditions, correlating well with the XRD results. A complex mixture of different phases was observed. The grains were more lamellar shaped compared to those observed in the S-TM samples (Figure 5.30 and Figure 5.31).

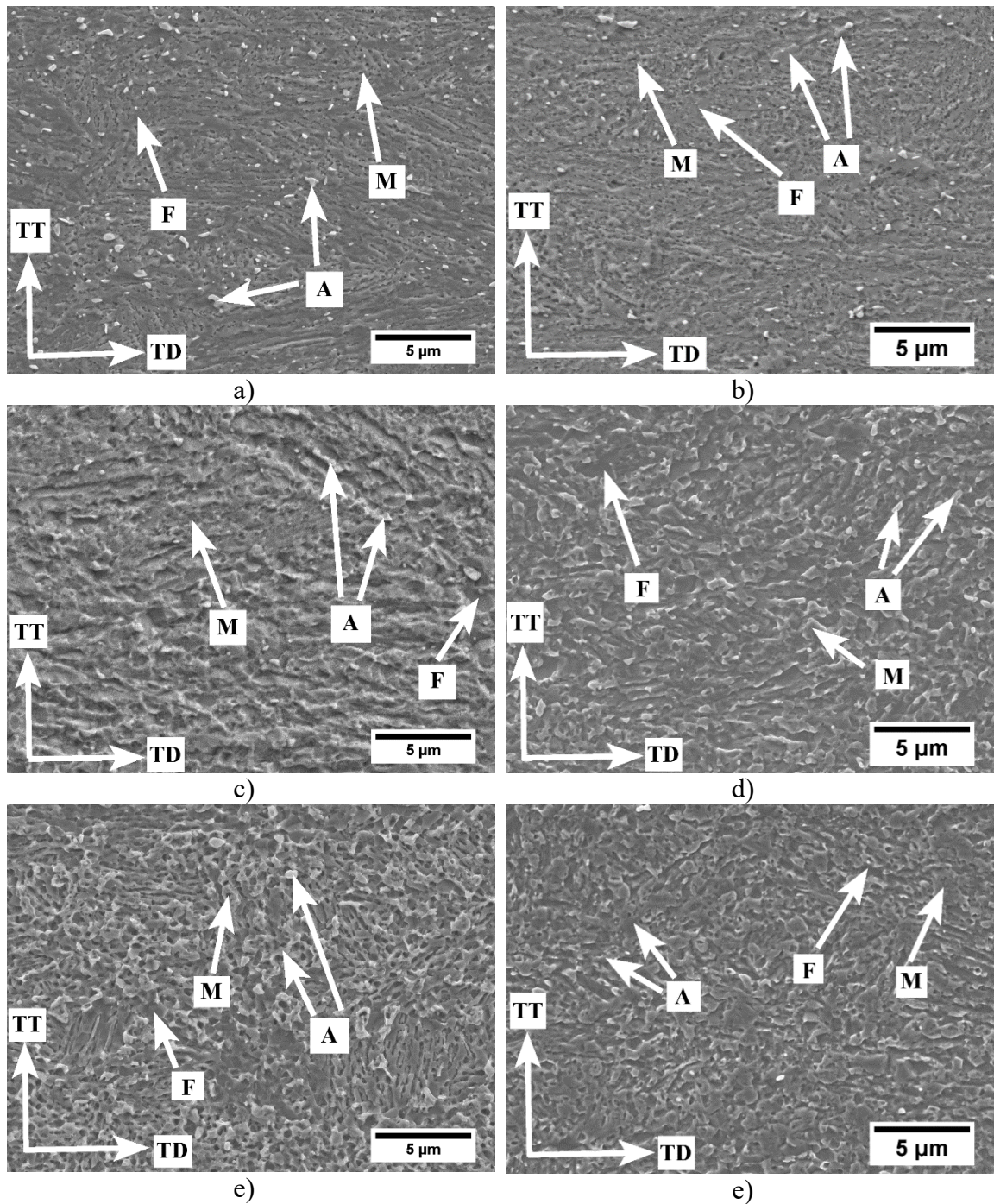


Figure 5.30: SEM micrographs of S-TM samples subjected to 710°C IAT for a) 60s, b)

120s, c) 240s, d) 360s, e) 480s and f) 600s and 60s OT treatment.

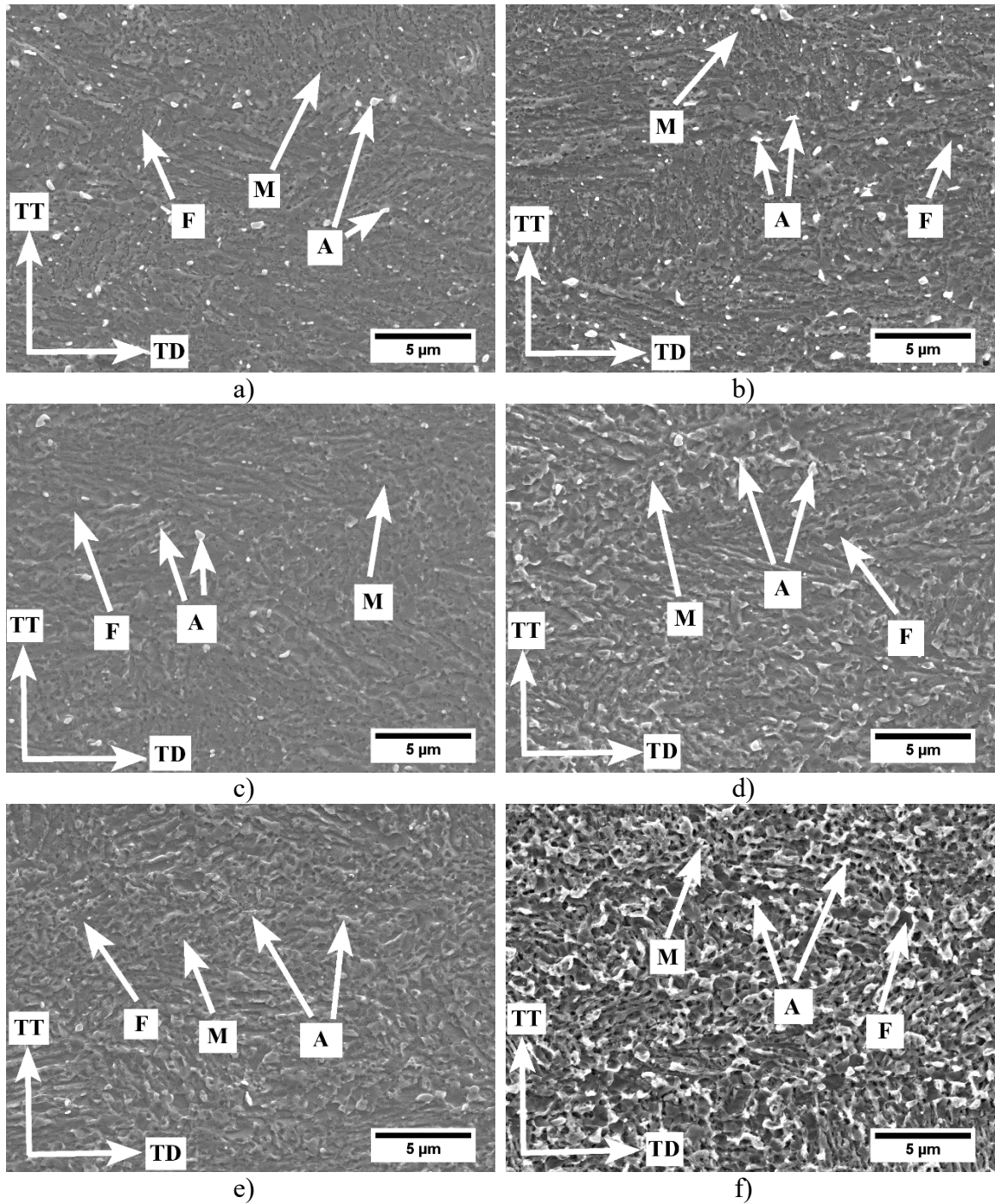


Figure 5.31: SEM micrographs of S-TM samples subjected to 710°C IAT for a) 60s, b) 120s, c) 240s, d) 360s, e) 480s and f) 600s and 120s OT treatment.

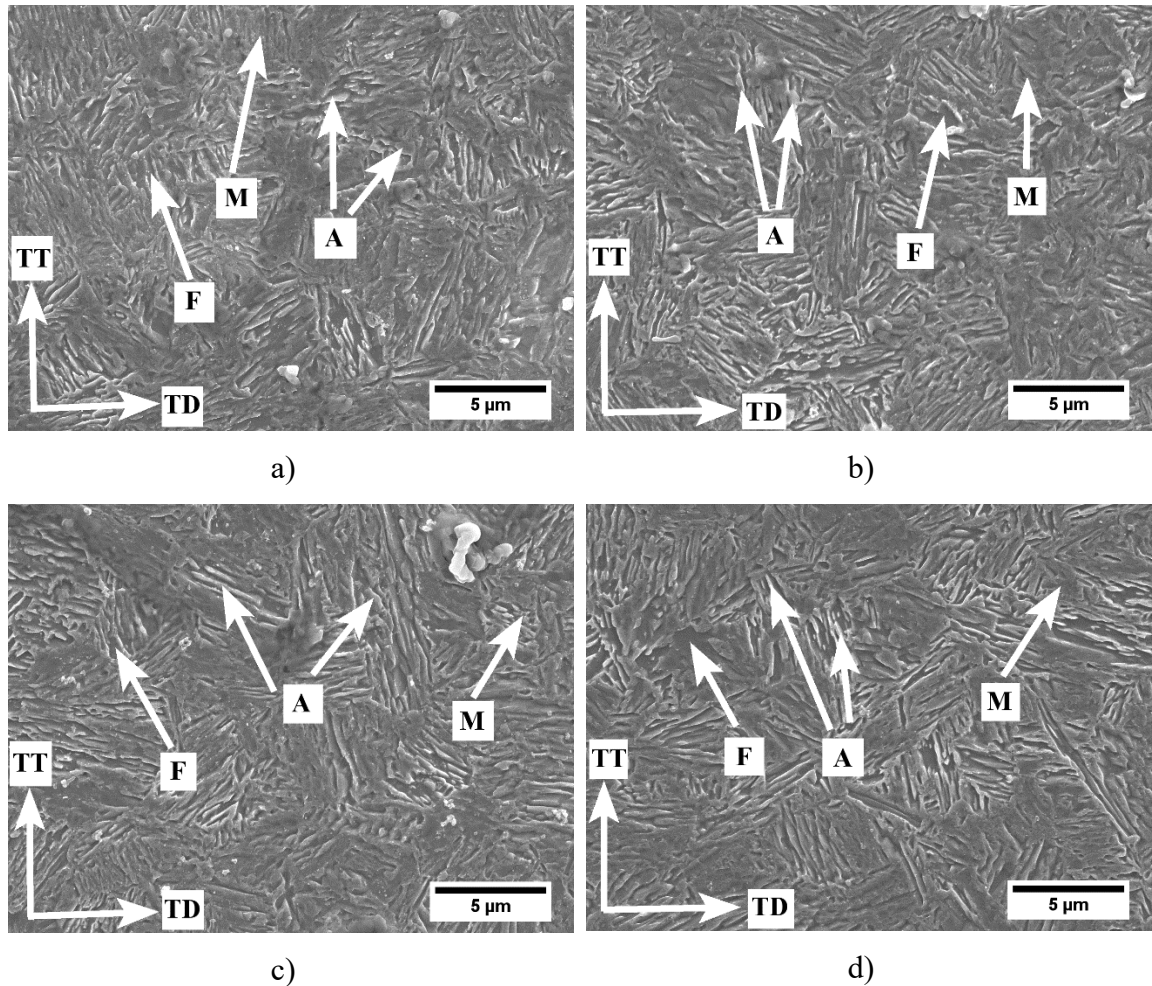


Figure 5.32: SEM micrographs of S-M samples subjected to 60s OT treatment following 675°C IAT for a) 60s, b) 120s; to 120s OT treatment following 675°C IAT for c) 60s, d) 120s.

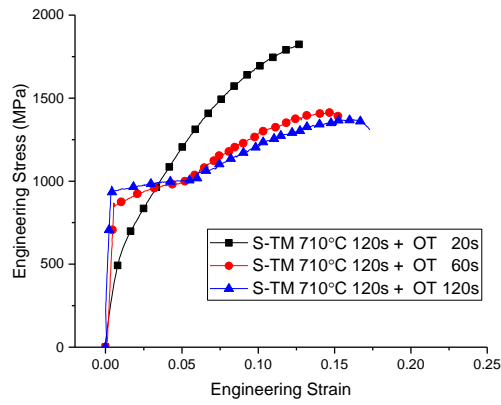
### 5.2.3 Mechanical Properties

Uniaxial tensile tests were conducted in order to determine the mechanical properties of the annealed samples as a function of OT holding time and IAT parameters. The results are shown in Figure 5.33 and the mechanical properties are summarized in Figure 5.34, Figure 5.35 and Table 5.3. The S-TM samples showed an increase in yield strength and

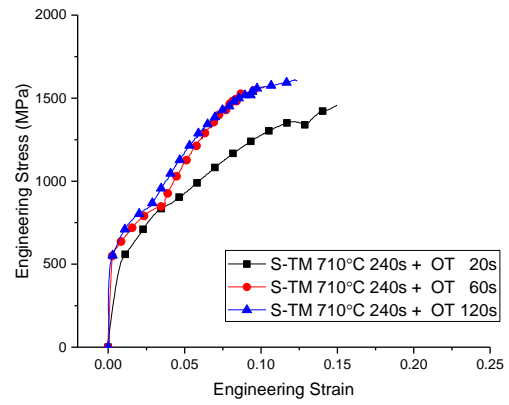
total elongation for the 710°C + 120s IAT condition versus the 20s OT baseline samples (Figure 5.34 a)). However, the ultimate tensile strength decreased significantly (Table 5.3). Another important observation for the 710°C + 120s IA samples was the occurrence of yield point elongation in the samples subjected to the 60s and 120s OT treatment (Figure 5.33a)). This suggests that the ferrite yielded prior to stress induced retained austenite to martensite transformation [69].

In case of the S-TM 710°C + 240s samples, increasing the OT holding did not change the yield strength significantly. However, the total elongation decreased whereas the UTS increased with no significant difference between the 60s and 120s OT holding time samples (as shown in Figure 5.34 b)). This implies the retained austenite was no longer chemically or mechanically stable to promote the desired TRIP/TWIP effect in the S-TM samples annealed for longer time (>120s) at 710°C IAT with 60s and 120s OT holding time.

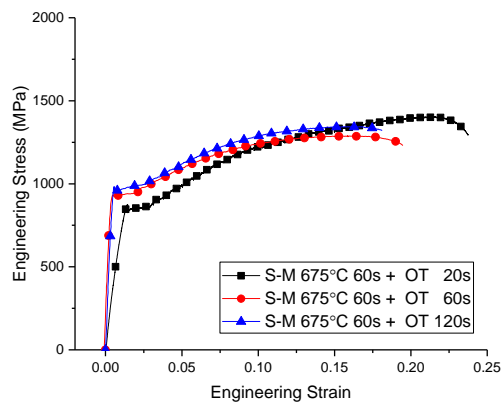
The S-M 675°C IAT samples annealed with the 60s and 120s OT holding times showed a significant increase in yield strength compared to the 20s OT baseline samples (Figure 5.35). However, the UTS and TE decreased resulting in a lower UTS × TE product compared to the 20s OT holding time S-M 675°C + 60s and 675°C + 120s samples. Moreover, yield point elongation was also observed in all the longer (60s and 120s) OT holding time S-M 675°C IAT samples (Figure 5.33 c) and d)).



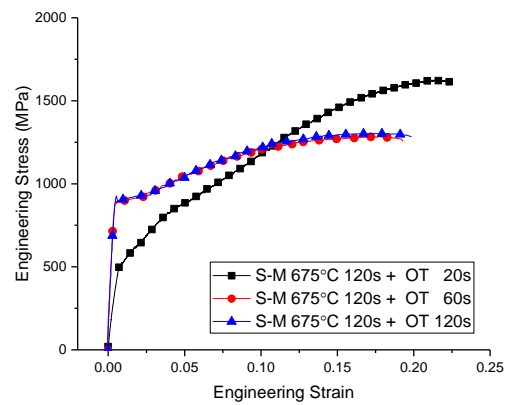
a)



b)

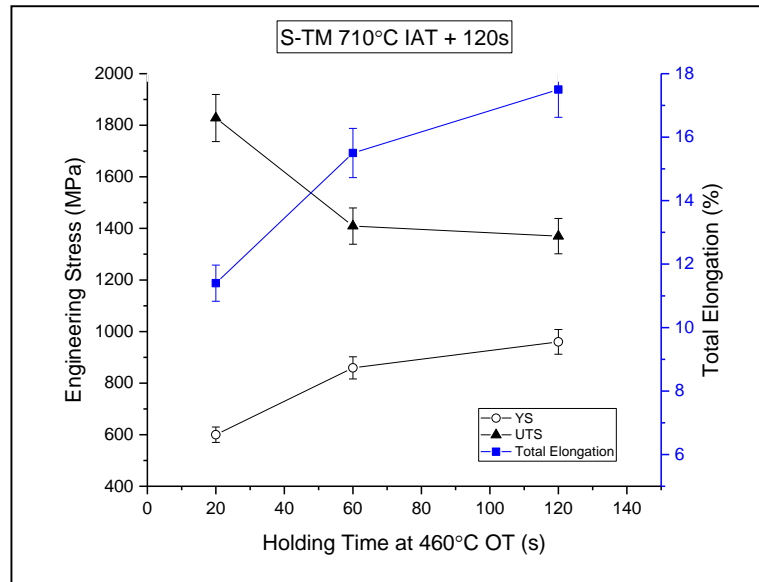


c)

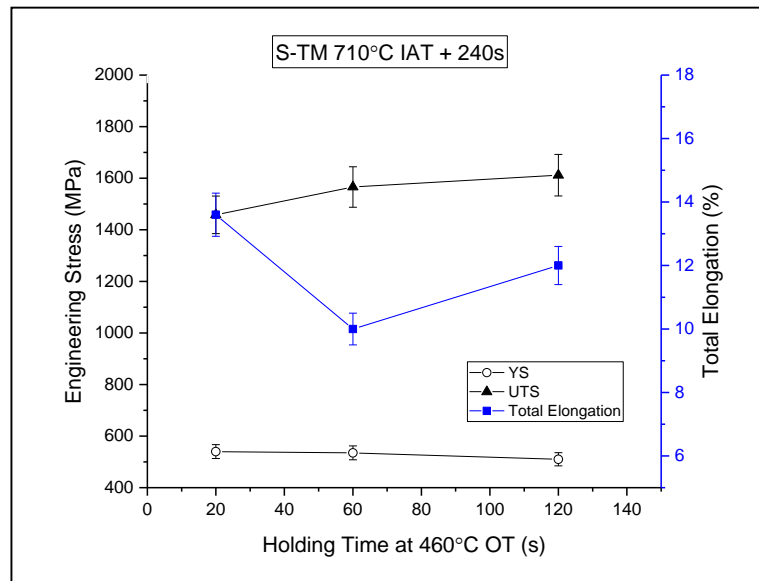


d)

Figure 5.33: Engineering stress vs strain curves as a function of OT holding times for S-TM samples annealed at 710°C IAT for a) 120s, b) 240s and S-M samples annealed at 675°C IAT for c) 60s and d) 120s.

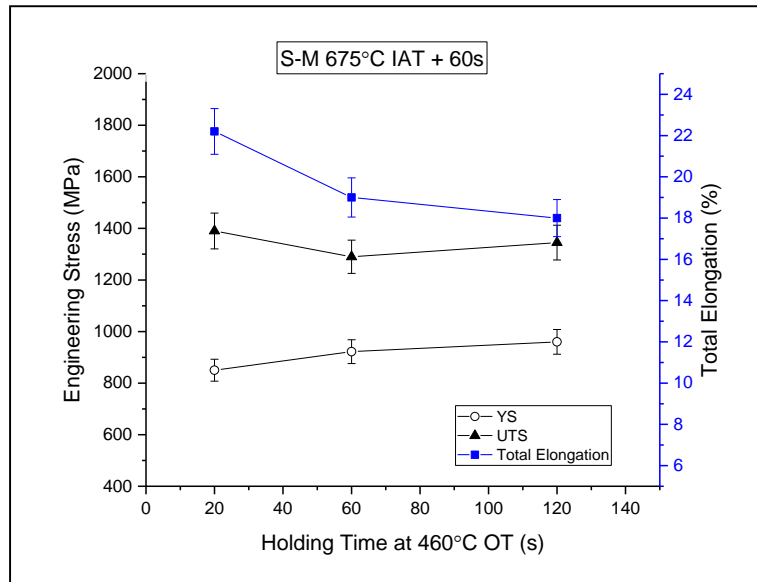


a)

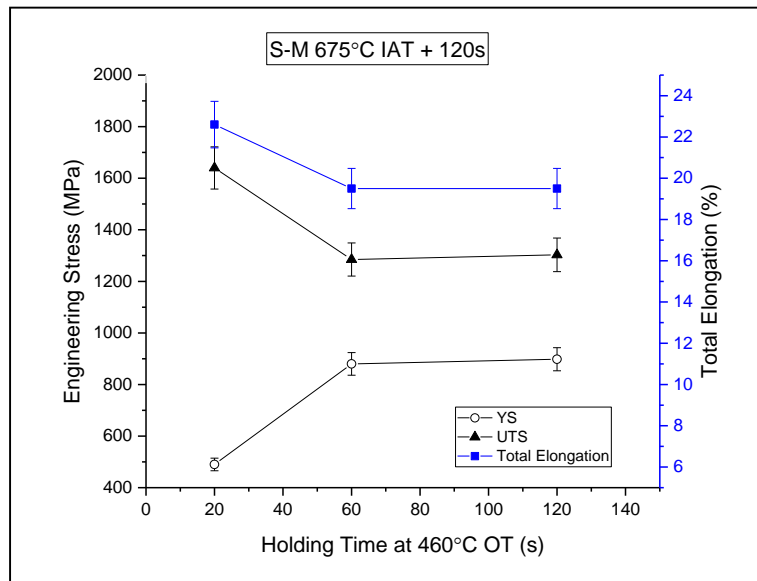


b)

Figure 5.34: Summary of mechanical properties of a) S-TM 710°C + 120s and b) S-TM 710°C + 240s samples as a function of OT holding times.



a)



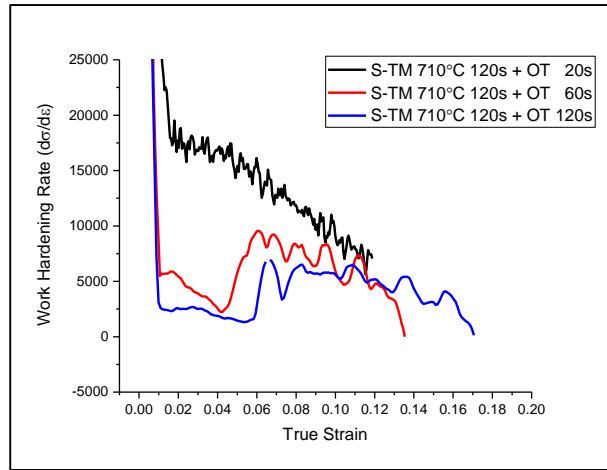
b)

Figure 5.35: Summary of mechanical properties of a) S-M 675°C + 60s and b) S-M 675°C + 120s samples as a function of OT holding times.

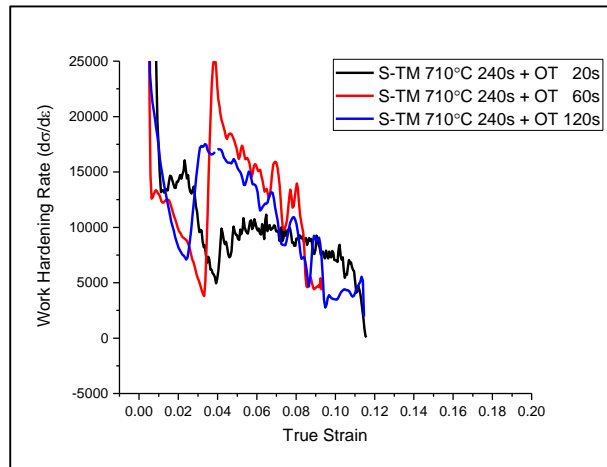
Work hardening rates ( $d\sigma/d\varepsilon$ ) were plotted as a function of true strain and OT holding times to observe their effect on this important parameter. The results are shown in Figure 5.36 and Figure 5.37, for the S-TM 710°C and S-M 675°C IAT samples, respectively. It was observed that the OT holding time had a significant effect on the S-TM 710°C +120s sample (Figure 5.36 a)). In this case, the work hardening rate with increasing strain changed from one consistent with a DP steel [20] to one that showed significant evidence of a TRIP or TWIP effect [68][69] for samples with 60s and 120s OT holding times. This is consistent with the XRD analysis (Figure 5.28) which showed an increase in retained austenite volume fraction. However, the S-TM 710°C + 240s samples with the 60s and 120s OT treatment showed a decreasing trend in work hardening rate initially followed by a sudden increase in work hardening rate at  $\varepsilon \approx 0.03$  and  $\varepsilon \approx 0.04$  for 60s and 120s OT treatment, respectively. The work hardening rate again followed a decreasing trend with increasing strain up to failure (Figure 5.36 b)). This suggests that a significant portion of the retained austenite was not chemically or mechanically stable to result in a gradual transformation to martensite as most of it transformed to martensite at  $\varepsilon \approx 0.03$  and  $\varepsilon \approx 0.04$  for 60s and 120s OT treatment, respectively, causing the sharp increase in work hardening rate (as shown in Figure 5.36 b)).

Figure 5.37 shows the work hardening rate versus true strain curves for the S-M samples as a function of OT holding time. The work hardening rate followed a similar trend with increasing strain regardless of the OT holding time, consistent with the XRD analysis (Figure 5.29), which revealed significant volume fraction of chemically stable retained austenite resulting in the desired TRIP/TWIP effect. The interrupted tensile test results,

shown in the following section (Figure 5.39), also confirmed the gradual transformation of the retained austenite suggesting the presence of chemically stable retained austenite which promotes the TRIP/TWIP effect.

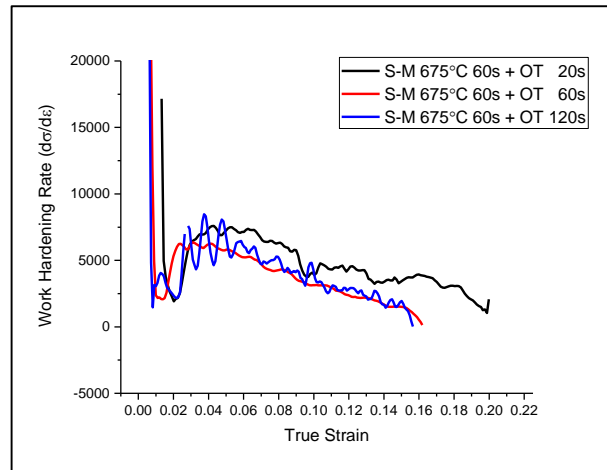


a)

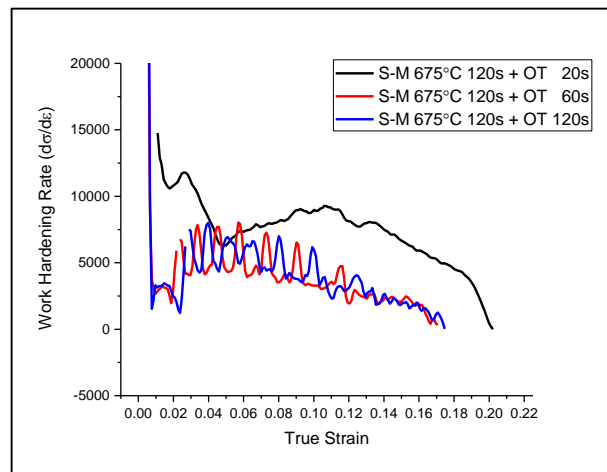


b)

Figure 5.36: Work hardening rate vs true strain for a) S-TM 710°C + 120s and b) S-TM 710°C + 240s samples as a function of OT holding times.



a)



b)

Figure 5.37: Work hardening rate vs true strain for a) S-M 675°C + 60s and b) S-M 675°C + 120s samples as a function of OT holding time.

A PLC effect similar to that observed for the 20s OT baseline samples (Figure 5.22) was identified in Figure 5.36 and Figure 5.37. These instabilities suggest that unstable plastic flow occurred after elastic deformation and were the result of dynamic strain aging where the dislocations interacted with the solute atoms during deformation. Based on the

XRD results (Figure 5.28 and Figure 5.29), the retained austenite C content was approximately 0.45-0.65 (wt.%) for the annealed S-TM and S-M samples which was sufficient to result in dynamic strain aging [68] [70].

Table 5.3 summarizes the mechanical properties of the annealed S-TM and S-M samples subjected to 20s, 60s and 120s OT treatments. It can be seen that S-TM 710°C + 120s samples with 60s and 120s OT treatment had a significant increase in YS and TE along with a significant decrease in UTS compared to the 20s OT baseline samples. The  $UTS \times TE$  product also increased, however, it was still below the target mechanical properties for 3G-AHSSs [14]. This was consistent with XRD results (Figure 5.28) which showed a significant increase in retained austenite volume fraction in sample subjected to 60s and 120s OT treatment compared to 20s OT baseline samples. Moreover, yield point elongation was observed in the 60s and 120s OT samples which might have arose from ferrite that yielded prior to stress induced TRIP effect. De Cooman et al. [69] observed similar yield point elongation behavior in a 7Mn-0.009C (wt.%) medium Mn TRIP-assisted steel where the ferrite yielded prior to retained austenite transformation to martensite. However, although XRD results showed similar increases in the retained austenite in S-TM 710°C + 240s samples, the mechanical properties, specially the TE, did not increase significantly resulting in low  $UTS \times TE$  products compared to the target mechanical properties for 3G-AHSSs [14]. This might be due to the fact that the retained austenite was not sufficiently chemically stable to promote a gradual transformation of retained austenite and maintain high work hardening rates at high strains.

Table 5.3 Summary of the Mechanical Properties (Effect of OT Holding Time)

Sample ID	Yield Strength (MPa)	Ultimate Tensile Strength, UTS (MPa)	Total Elongation, TE (%)	UTS×TE (MPa %)
S-TM (OT 20s) 710°C + 120s	600	1828	11.4	20,839
S-TM (OT 60s) 710°C + 120s	859	1409	15.5	21,839
S-TM (OT 120s) 710°C + 120s	960	1370	17.5	23,975
S-TM (OT 20s) 710°C + 240s	540	1458	13.6	19,828
S-TM (OT 60s) 710°C + 240s	535	1566	10	15,660
S-TM (OT 120s) 710°C + 240s	510	1612	12	19,344
S-M (OT 20s) 675°C + 60s	850	1390	22.2	30,858
S-M (OT 60s) 675°C + 60s	922	1290	19	24,510
S-M (OT 120s) 675°C + 60s	960	1345	18	24,210
S-M (OT 20s) 675°C + 120s	490	1640	22.6	37,064
S-M (OT 60s) 675°C + 120s	880	1285	19.5	25,057
S-M (OT 120s) 675°C + 120s	898	1303	19.5	25,408

Both S-M 675°C + 60s and S-M 675°C + 120s samples subjected to 60s and 120s OT treatments showed similar significant increases in YS and decreases in UTS as well as TE compared to the 20s OT baseline samples. As a result, the UTS × TE product decreased significantly for the S-M samples annealed with 60s and 120s OT holding times. However, this was not consistent with the XRD results (Figure 5.29) which showed similar volume fraction of retained austenite in the S-M samples regardless of OT holding times. Moreover, yield point elongation was also observed in the S-M samples subjected to 60s and 120s OT treatments. This suggests that the ferrite yielded prior to stress induced transformation of retained austenite.

#### ***5.2.4 Interrupted Tensile Tests***

Interrupted tensile tests were conducted for the longer (60s and 120s) OT holding time samples in order to determine if any changes had occurred in the retained austenite transformation kinetics versus the baseline 20s OT samples. The results for the S-TM samples are shown in Figure 5.38. S-TM 710°C + 240s sample followed a similar trend regardless of OT holding time, where the retained austenite transformed rapidly at lower strains and was almost completely transformed by  $\epsilon \approx 0.10$  (Figure 5.38), suggesting that the retained austenite was not stable.

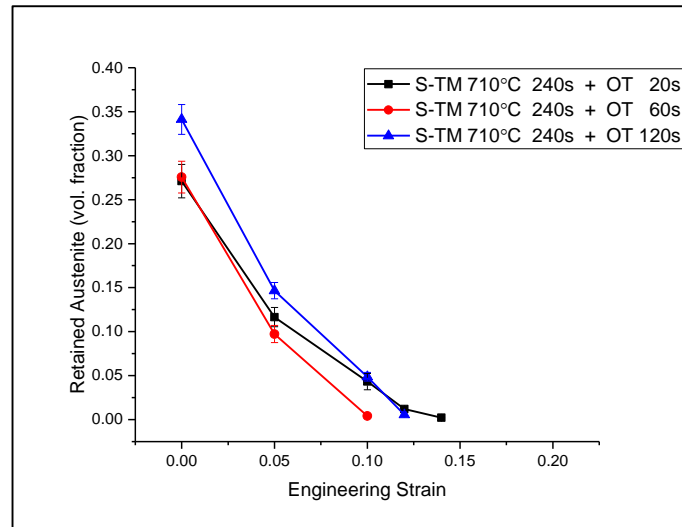
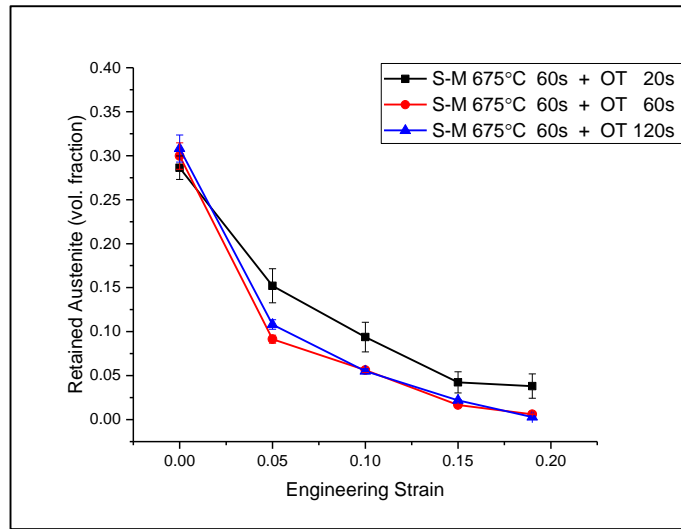
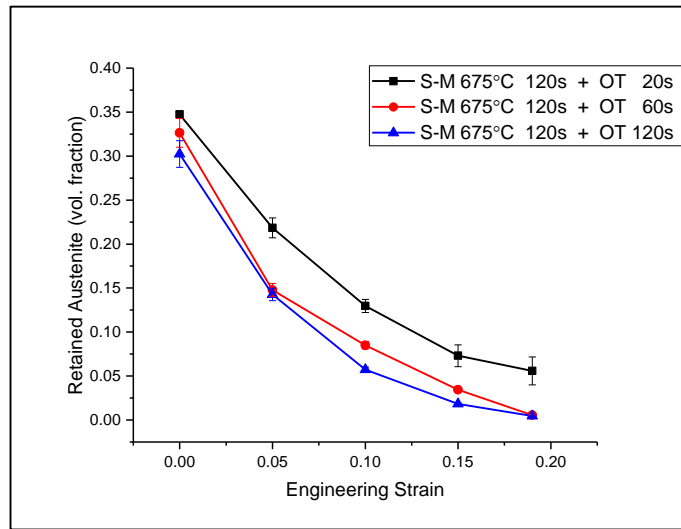


Figure 5.38: Retained austenite transformation kinetics of S-TM 710°C + 240s sample as a function of OT holding times.

Figure 5.39 shows the results of the interrupted tensile tests for S-M 675°C + 60s and S-M 675°C + 120s samples as a function of OT holding time. In both cases, a gradual transformation of retained austenite was observed regardless of OT holding times. This suggests that the retained austenite in the annealed samples was stable enough to promote gradual transformation to martensite at higher strains. This type of gradual transformation is desirable as it results in maintaining high work hardening rate at high strain which delays the onset of necking and results in high strength/ductility balance [20].



a)



b)

Figure 5.39: Retained austenite transformation kinetics of a) S-M 675°C + 60s and b) S-M 675°C + 120s samples as a function of OT holding times.

### **5.2.5 Fractography**

The fracture surfaces of the tensile samples were analyzed using SEM. The SEM micrographs of the S-TM samples as a function of OT holding time are shown in Figure 5.40. Microcracks were observed along with ductile tearing in the case of the S-TM 710°C + 120s samples subjected to the 60s and 120s OT treatment (Figure 5.40 a) and b)). However, the S-TM 710°C + 240s samples with the 60s and 120s OT holding times revealed some cleavage along with ductile tearing, suggesting a mixed fracture mode operating in these cases, as shown in Figure 5.40 c) and d). Moreover, microcracks were observed propagating along the cleavage boundaries, circled red in Figure 5.41.

SEM micrographs of the cross-section near the fracture surface of the S-TM 710°C + 240s samples subjected to the 60s and 120s OT treatment are shown in Figure 5.41. Microvoids and some microcracks were observed at the grain boundaries, between softer grains (ferrite, bainitic ferrite or martensite with low hardness) and harder grains (martensite with high hardness). Moreover, the microvoids and microcracks were more frequent in the sample with the 120s OT holding time (Figure 5.41 b)). These microvoids likely coalesced and formed microcracks which ultimately led to fracture, suggesting that the fracture mechanism was classic void nucleation and coalescence along the grain boundaries, similar to that observed for the 20s OT baseline samples (Figure 5.24).

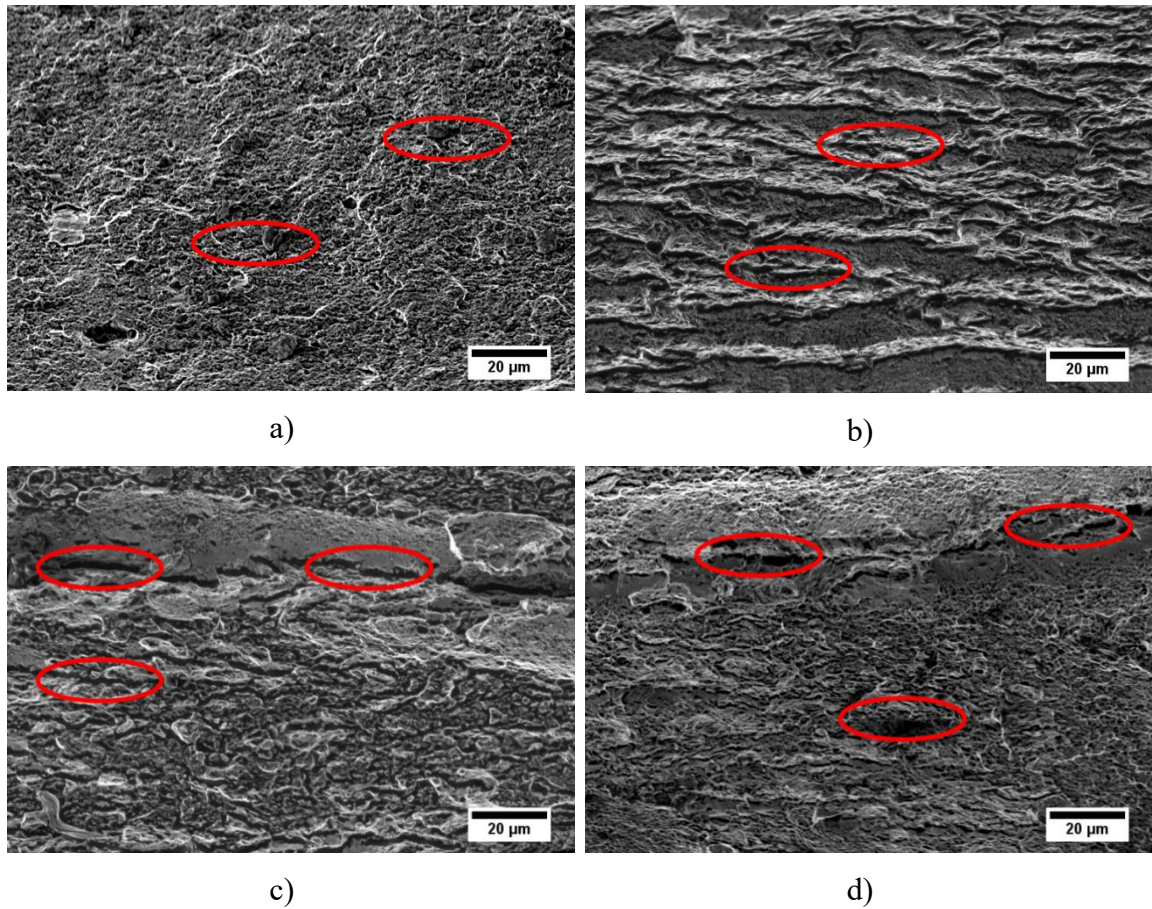


Figure 5.40: Fracture surface micrographs of S-TM 710°C+ 120s samples with a) 60s OT and b) 120s OT and S-TM 710°C + 240s samples with c) 60s OT and d) 120s OT treatment where the microcracks are shown in red circles.

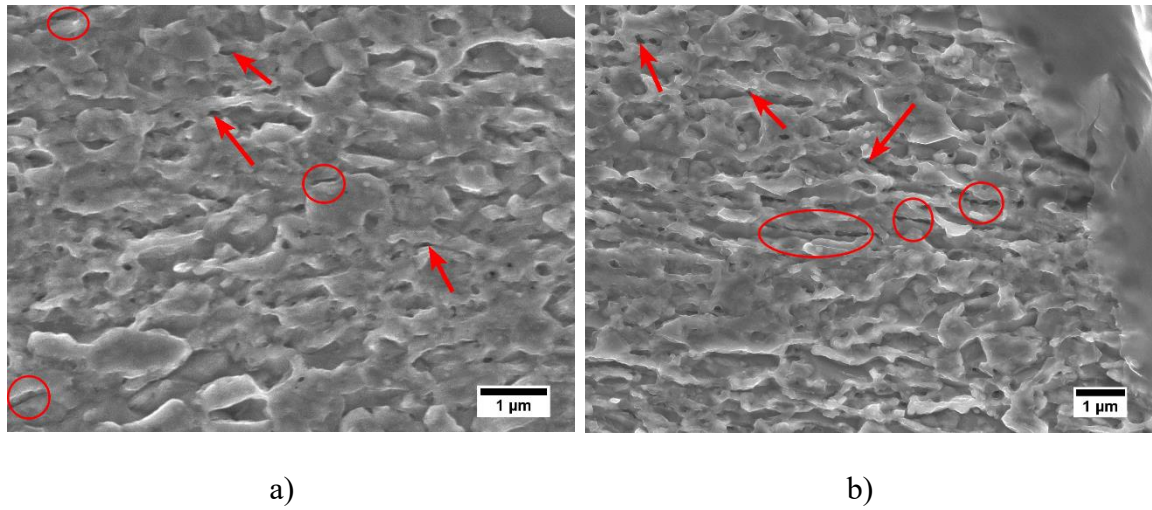


Figure 5.41: Cross section near fracture surface of S-TM 710°C + 240s sample with a) 60s OT and b) 120s OT treatment where the microvoids and microcracks are shown using red arrows and red circles, respectively.

Fracture surfaces of the S-M samples with 60s and 120s OT treatments were also similar to the 20s OT baseline samples (Figure 5.24 c) and d)), as shown in Figure 5.42. Ductile tearing was observed, which suggested that the dominant fracture mode was ductile in nature. Moreover, microcracks were observed more frequently in these samples, circled red in the micrographs, suggesting void coalescence to be the main fracture mechanisms. Cross-sections near the fracture surface also revealed microcracks propagating along grain boundaries, as shown in Figure 5.43, identified by red circles. This suggests the fracture mechanism was a classic void nucleation and coalescence along the grain boundaries, similar to the 20s OT baseline samples (Figure 5.24 and Figure 5.26).

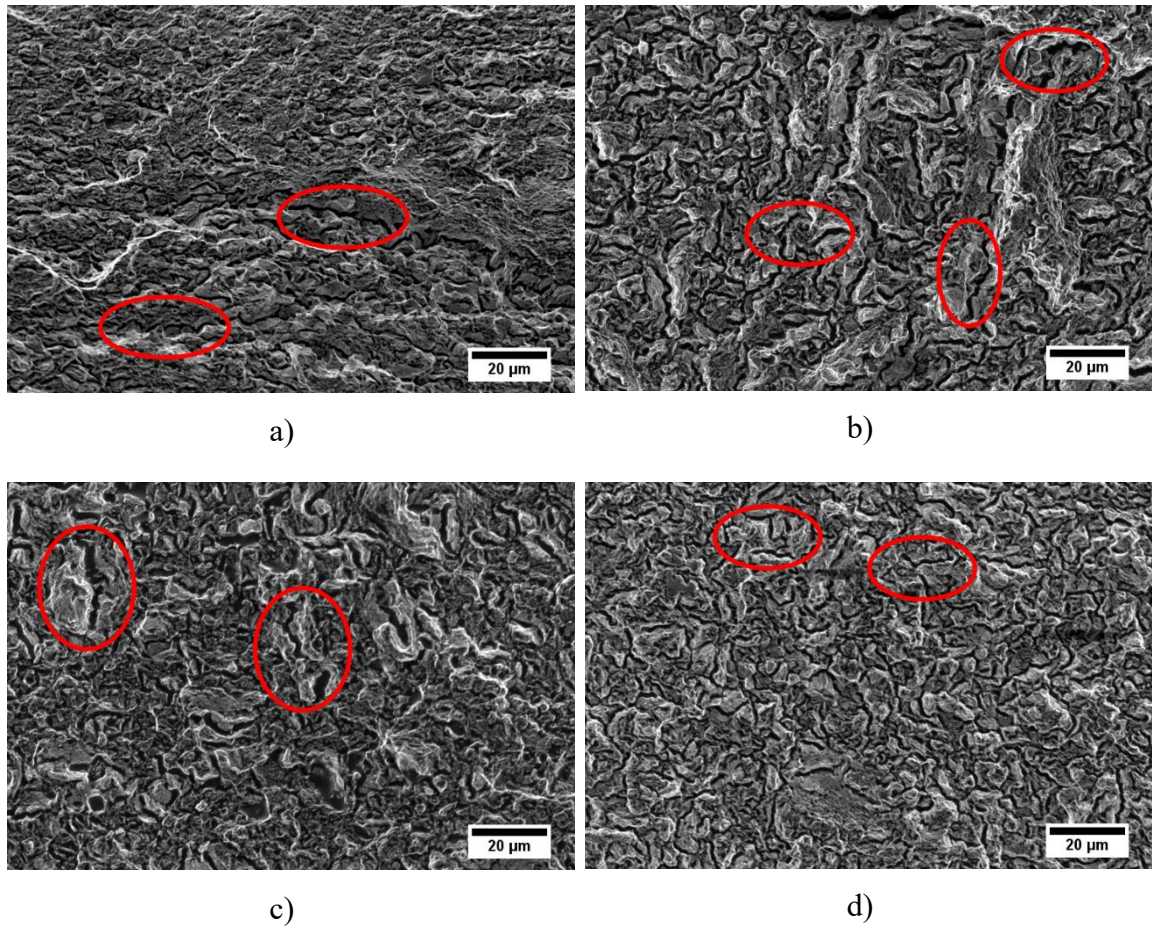


Figure 5.42: Fracture surface micrographs of S-M 675°C + 60s samples with a) 60s OT and b) 120s OT and S-M 675°C + 120s samples with c) 60s OT and d) 120s OT treatment where the microcracks are shown using red circles.

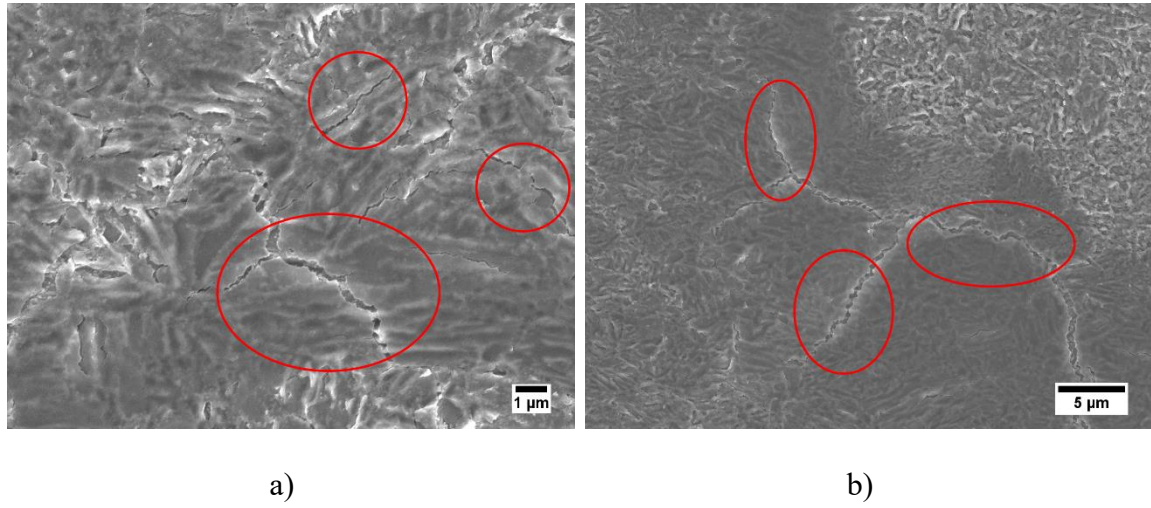


Figure 5.43: Cross-section near fracture surface of S-M 675°C + 120s sample with a) 60s and b) 120s OT treatment where the microcracks are shown using red circles.

### 5.3 Results Summary

An experimental medium Mn TRIP-assisted steel (0.2C-6Mn-1.5Si-0.5Al-0.5Cr wt.%) was annealed with CGL compatible heat treatment parameters in order to determine their effect on the microstructural evolution and mechanical properties. S-TM (tempered martensitic starting microstructure) samples annealed with the 20s OT holding time showed an increasing trend in retained austenite volume fraction with increasing holding time at both the 675°C and 710°C IATs. A long holding time of 600s at 710°C IAT yielded the highest volume fraction of retained austenite in the S-TM samples. On the other hand, S-M (martensitic starting microstructure) samples annealed with the 20s OT holding time followed a different trend compared to S-TM samples in terms of retained austenite volume fraction development. For the 675°C IAT, the retained austenite volume fraction increased significantly with IAT holding time up to 360s. The retained austenite volume fraction started to decrease for IAT holding time > 360s for 675°C and > 60s for 710°C, which was

attributed to the transformation of the intercritical austenite to martensite during final cooling due to low chemical stability. However, 60-120s holding time at 675°C IAT was sufficient to achieve > 0.30 volume fractions of retained austenite. SEM and TEM analysis was performed to characterize the microstructure of the annealed samples which revealed an ultra-fine grained microstructure consisting of a complex mixture of multiple phases (ferrite, bainitic ferrite, retained austenite and martensite). Moreover, dark field TEM showed most of the retained austenite in the S-M samples was present in a film type morphology, which is known to be more mechanically stable compared to the block type morphology. As a result, the mechanical properties of the S-M samples annealed at 675°C IAT for 60, 120s and 360s showed an excellent combination of strength and ductility ( $UTS \times TE > 30,000 \text{ MPa}\%$ ) owing to maintaining high work hardening rates at higher strains. S-TM 710°C + 600s sample also had a high  $UTS \times TE$  product (30,456 MPa%) owing to high volume fractions of chemically stable retained austenite. However, in terms of CGL processing windows, a 600s IAT holding time is not desirable. The interrupted tensile test results for these S-M samples also confirmed a gradual transformation of the retained austenite. Moreover, fracture surface and cross-section near the fracture surface analysis with SEM revealed that the main fracture mechanism was classic void nucleation and coalescence along the grain boundaries.

In the second part of this study, the effect of OT holding time on the microstructural evolution and mechanical properties of the experimental steel was determined. The OT holding time was varied from 20s to 120s in that regard. For S-TM samples, the retained austenite volume fraction increased significantly with increasing holding time at 710°C

IAT compared to baseline 20s OT holding time samples. However, the retained austenite volume fraction did not change significantly regardless of OT holding time in the case of S-M samples. The SEM micrographs correlated well with the XRD results showing a complex mixture of various phases similar to those observed for the 20s OT baseline samples. The mechanical properties were also determined and assessed with respect to the 20s OT baseline samples as well as target 3G-AHSSs mechanical properties (Table 5.3). S-TM 710°C + 120s samples with 60s and 120s OT treatment had an increase in YS and TE compared to the 20s OT baseline samples. However, the UTS decreased significantly resulting in only a slight increase in the UTS × TE product, well below the target for 3G-AHSS mechanical properties. Moreover, yield point elongation was observed in 60s and 120s OT holding time samples suggesting that ferrite yielded prior to the stress induced retained austenite to martensite transformation. S-TM 710°C + 240s samples with 60s and 120s OT treatment had a decreasing and increasing trend in TE and UTS, respectively, compared to the 20s OT baseline samples whereas the YS did not change significantly. The UTS × TE product was less than 20,000 MPa% for these samples. This was inconsistent with the XRD results which showed significant volume fractions of retained austenite. However, interrupted tensile tests revealed that most of the retained austenite transformed at low strain ( $\epsilon \approx 0.10$ ) suggesting the retained austenite was not chemically stable. S-M samples (both S-M 675°C + 60s and S-M 675°C + 120s) subjected to 60s and 120s OT treatment showed a similar increasing trend in YS and decreasing trend in UTS and TE compared to the 20s OT baseline samples, resulting in significant decrease in UTS × TE product. This was also not consistent with the XRD results which showed similar volume

fractions of retained austenite as well as similar retained austenite to martensite transformation kinetics. Moreover, yield point elongation was observed in these S-M samples. In terms of fractography, similar fracture mechanism was observed versus the 20s OT baseline samples. All of these trends will be discussed in detail in the following chapter.

## **6 DISCUSSION**

The effect of intercritical annealing parameters and overaging temperature holding time with different starting microstructures were investigated for a medium Mn TRIP steel containing 0.2C-6Mn-1.5Si-0.5Al (wt.%). As-received tempered martensite and heat treated martensite were the two starting microstructures analyzed in this investigation. The intercritical annealing temperatures were chosen such that they would produce high volume fractions of intercritical austenite. The heat treated samples were analyzed using various techniques. XRD was used to determine the retained austenite volume fractions whereas SEM and TEM were used to characterize the microstructure of the annealed samples. Tensile tests were used to determine mechanical properties as a function of the heat treatments employed, which were then assessed with respect to established target mechanical properties for 3G-AHSSs [14].

### **6.1 Effect of Intercritical Annealing Parameters on S-TM Samples**

The XRD (Figure 5.1) and SEM (Figure 5.4 and Figure 5.5) results showed that for the S-TM samples, the volume fractions of retained austenite increased with holding time for both the 675°C and 710°C IATs, with the 710°C IAT and at least 360s holding time being required to produce the desired volume fractions ( $> 0.30$ ) of retained austenite in these annealed samples. More intercritical austenite formed due to the fact that the reaction proceeded further with longer holding times at the 710°C IAT and the austenite was chemically stable owing to C and Mn partitioning. This trend was consistent with the trends observed for various medium Mn TRIP steels [16][63][64], where the intercritical austenite

was stabilized chemically through C and Mn partitioning at higher intercritical annealing temperatures.

The XRD results (Figure 5.1) showed that the C content of the retained austenite did not change significantly with increasing annealing temperature or holding times, suggesting the C content reached the equilibrium value within a short amount of time due to faster diffusion rate regardless of the IATs. This was also consistent with the findings by De Cooman [32] for a low alloy TRIP-assisted steels where C, being an interstitial alloying element, diffused rapidly and reached its equilibrium concentration within annealing times of 21s. Moreover, although Mn is a substitutional alloying element which diffuses slowly compared to C, a 710°C IAT and longer holding times likely allowed more Mn partitioning into the intercritical austenite as the diffusivity of Mn increased at 710°C IAT. As a result, the intercritical austenite was likely more chemically stable for samples that were annealed for longer holding times at 710°C IAT. However, atom probe tomography (APT) analysis is needed in order to confirm this hypothesis. This chemically stable intercritical austenite did not transform to martensite during final cooling, resulting in higher volume fractions of retained austenite in the annealed samples. This trend, however, is not consistent with low alloy TRIP-assisted steels, where the retained austenite volume fractions tend to decrease with increasing intercritical annealing temperatures. Jacques et al. [71] suggested lower intercritical annealing temperatures for conventional low alloy TRIP-assisted steels as although higher intercritical annealing temperatures yielded higher amount of equilibrium intercritical austenite, this austenite had a lower C content, which made them chemically unstable.

The mechanical properties of the annealed samples having higher volume fractions of retained austenite were determined by uniaxial tensile tests. S-TM samples annealed at 710°C IAT for 120s, 240s and 600s were selected in that regard. The results (Figure 5.20) showed that, although there was a decrease in yield strength and ultimate tensile strength for the S-TM samples with increasing holding time compared to the as-received cold rolled steel, the total elongation increased with IA holding time. This was due to increase in retained austenite volume fractions from 0.05 to 0.37 with increasing holding time at 710°C IAT for S-TM samples, as shown in Figure 5.1. The highest elongation was observed for the sample annealed at 710°C IAT for 600s. This result is consistent with those of Lee and De Cooman [16], who also reported that the best combination of mechanical properties resulted from the annealed medium Mn TRIP steel sample containing over 40% volume fractions of retained austenite. The S-TM sample annealed at 710°C IAT for 600s also had the highest UTS × TE product (30,456 MPa%) among the S-TM samples. However, 600s is too long for an industrial CGL where the steel substrate usually resides for a total of 3-5 minutes in the annealing furnace. Hence, this processing condition is not likely compatible with CGL processing windows.

The work hardening rate for the annealed samples was plotted as a function of true strain in order to indicate whether the TRIP or TWIP effects had occurred during deformation. The results (Figure 5.22) showed that S-TM 710°C +120s sample had a decreasing work hardening rate with increasing true strain. This type of work hardening rate is typically observed in dual phase (DP) steels which do not exhibit the TRIP effect [20]. The S-TM 710°C + 240s and S-TM 710°C +600s samples, however, had a different

work hardening rate compared to the S-TM 710°C + 120s sample. In these samples, the work hardening rate initially decreased followed by a gradual increase in work hardening rate with increasing true strain up to a certain strain. Finally, the work hardening rate decreased with increasing strain to failure. This type of work hardening rate curve is usually observed in steels which exhibit significant TRIP/TWIP effects owing to gradual retained austenite to martensite transformation [11][72] or twinning within the austenite. In addition, a recent study by Lee et al. [21] showed that medium Mn TRIP steels can have both TWIP and TRIP effects depending on the heat treatment parameter and stacking fault energy (SFE) of the retained austenite. They have found that if the room temperature SFE of the austenite phase was approximately 20 mJ/m<sup>2</sup>, the plasticity enhancing mechanism started by mechanical twinning during deformation followed by the deformation induced transformation of retained austenite to martensite. This led to an exceptional strength/ductility balance (~65,000 MPa %). The SFE of the retained austenite in this study was determined using Dumay et al. model [39] and found to be approximately 8.51 mJ/m<sup>2</sup> which suggests the retained austenite transformed by twinning or  $\epsilon$  martensite formation. However, detailed TEM needs to be done in order to evaluate the effect of stacking fault energy of retained austenite on the plasticity enhancing mechanisms and overall mechanical properties of this experimental medium Mn TRIP steel.

Moreover, the instabilities observed in the work hardening rate were likely due to the Portevin-Le Chatelier (PLC) effect owing to dynamic strain aging. Ghasri-Khouzani [68] observed similar instabilities in work hardening rate for high Mn TWIP steels with high C content (0.4 and 0.6 wt.%). The XRD results (Figure 5.1) showed that retained austenite C

content was approximately 0.45 – 0.60 (wt.%) for the annealed S-TM samples which was sufficient to result in the observed PLC effect.

## **6.2 Effect of Starting Microstructure**

The sample starting microstructure had a significant effect on the retained austenite formation kinetics. The XRD and SEM results (Figure 5.2, Figure 5.6 and Figure 5.7) showed that a 675°C IAT and shorter holding times (60s and 120s) were sufficient to result in > 0.30 volume fractions of retained austenite in the case of the martensitic starting (S-M) microstructure samples. By contrast, a 710°C IAT and 360s holding time was required to achieve > 0.30 volume fraction of retained austenite in the as tempered martensitic (S-TM) starting microstructure samples.

As reported by Nakada et al. [17], the martensite to austenite transformation is more rapid versus that of the tempered martensite starting microstructure, due to the fact that the martensite is highly strained and supersaturated with carbon as it is the product of diffusionless transformation of intercritical austenite during quenching. Hence, less energy is required for the nucleation and growth of the intercritical austenite at the martensite lath boundaries during intercritical annealing resulting in the rapid reversion of the martensite to austenite. The authors also observed thin austenite films forming along martensite lathes during the annealing of a 0.1 C – 5 Mn (wt.%) steel which were more chemically stable due to C and Mn partitioning. The authors reported a higher Mn diffusivity in the martensitic matrix compared to the austenite based on DICTRA simulation results. Moreover, Luo and Dong [22] observed higher volume fractions of retained austenite for 0.1 C – 5 Mn (wt.%) and 0.2 C – 5 Mn (wt.%) TRIP steels that had a martensitic starting

microstructure versus a conventional cold rolled microstructure consisting of martensite, ferrite and some cementite. Lamellar retained austenite was observed in their study for martensitic samples owing to the nucleation sites being at the martensite lath boundaries where the highly strained martensite rapidly reverted to austenite during intercritical annealing.

Previous studies [10][47][65][73][74] on low alloy TRIP-assisted steels have suggested that lamellar retained austenite is more chemically and mechanically stable compared to blocky retained austenite because of both higher chemical stability, owing to higher carbon content and higher mechanical stability owing to being mechanically constrained by the surrounding bainitic ferrite and martensite phases. Moreover, Lee et al. [64] and Luo [49] have also concluded that lamellar retained austenite was both chemically and mechanically more stable compared to blocky retained austenite in medium Mn TRIP steels. This suggests that lamellar or film type retained austenite is both chemically and mechanically more stable compared to blocky retained austenite in both conventional low alloy and medium Mn TRIP steels. Similar film-type retained austenite was observed in this study for the S-M samples analyzed by TEM and shown in Figure 5.9, Figure 5.12 and Figure 5.13. This suggests the faster transformation kinetics during the austenite reversion transformation in the martensitic starting microstructure (S-M) samples resulted in more intercritical austenite within a short amount of time (60s and 120s). This reverted austenite nucleated at the martensite lath boundaries and was present as film type retained austenite which is known to be more stable compared to blocky retained austenite. As a result, higher volume fractions of stable retained austenite were detected in the final microstructure after

60s and 120s holding times at 675°C IAT for the S-M samples versus the same times for the 710°C IAT treatment for the S-TM samples

However, at longer holding times, the S-M samples showed a decreasing trend in retained austenite volume fractions compared to that observed in S-TM samples, as shown in Figure 5.2. In particular, there was a decrease in retained austenite volume fraction for S-M samples annealed longer than 360s at the 675°C IAT and for longer than 60s at the 710°C IAT. This can be attributed to unstable austenite which transformed to martensite during cooling, as shown by the XRD results in Figure 5.3. The C content was significantly lower for the 710°C IAT compared to the 675°C IAT for a given IA holding time (Figure 5.1 and Figure 5.2), suggesting that the retained austenite was chemically less stable for the 710°C IAT samples which resulted in austenite to martensite transformation during final cooling. However, the XRD data, as shown in Figure 5.2, revealed that the C content did not change significantly for various IA holding times at 675°C IAT. In this case, lower volume fractions of retained austenite was likely attributed to the mechanical stability of the retained austenite. This was also consistent with the results observed by Luo [49] who reported that retained austenite stability decreased with increasing holding times and it was related to the grain growth phenomenon, i.e. longer holding times increased the austenite grain size without any significant change in the C content of that grain. As a result, a retained austenite grain that was stable at the lower IA times was no longer stable at longer holding times with similar amount of C. This was related to the mechanical stability of the retained austenite grains which was associated with the energy required to accommodate the austenite to martensite transformation strain. For larger austenite grains, less energy

was required to generate dislocations which would accommodate the transformation strain, making them less mechanically stable compared to smaller austenite grains.

TEM analysis of the S-M samples also revealed carbide precipitation for both the 675°C and 710°C IATs regardless of the holding time. EDS analysis showed that these  $M_{23}C_6$  type carbides were Cr and Mn-rich. This was consistent with the results observed by Han and Lee [51] for various medium Mn (5, 7 and 9 Mn wt.%) steels. They showed that heating rate had a profound effect on carbide precipitation and at least a 15°C/s heating rate was required to have a diffusionless austenite reversion transformation (ART) which would result in a carbide free microstructure. In this study, the heating rate was 5°C/s which resulted in diffusion based ART. As a result, carbide precipitation occurred regardless of the intercritical annealing temperature and holding time. Moreover, orientation relationships (ORs) between ferrite and retained austenite were determined based on the dark field TEMs and their corresponding SAD patterns. Both Nishiyama-Wasserman (N-W) and Kurdjumov-Sacks (K-S) orientation relationships were confirmed for S-M samples (Figure 5.14), suggesting two different crystallographic orientation for the bcc phase. However, Lee et al. [21] observed only one type of orientation relationship (K-S) between retained austenite and ferrite for two different Fe-0.15C-6Mn-1.5Si-3Al (wt.%) and Fe-0.3C-6Mn-1.5Si-3Al (wt.%) steels. In this study, two different ferrite zone axes were identified instead of one (Figure 5.13) suggesting different crystallographic orientation for ferrite which resulted in two different orientation relationships.

The S-M samples achieved mechanical properties (Figure 5.21) similar to the best mechanical properties of the S-TM samples with conditions more compatible with CGL

processing capabilities. The S-M samples annealed at 675°C IAT for 120s met the target mechanical properties for 3G-AHSSs [14], yielding a  $UTS \times TE$  product of 37,064 MPa%. Luo and Dong [22] also observed better mechanical property combination for martensitic starting microstructure samples compared to cold rolled samples for 0.2 C-5 Mn (wt.%) and 0.1 C-5 Mn (wt.%) steels annealed for 10 minutes at 650, 670, 690 and 710°C IATs. This superior mechanical property balance was the result of high volume fractions of chemically and mechanically stable lamellar retained austenite, formed by an austenite reversion transformation (ART) from martensite during annealing. In this study, similar lamellar retained austenite was observed (Figure 5.9, Figure 5.12 and Figure 5.13) which was more chemically and mechanically stable compared to blocky retained austenite as discussed earlier. The interrupted tensile test results (Figure 5.23) of selected S-M samples showed that the retained austenite gradually transformed to martensite during straining. This gradual transformation of retained austenite was desirable as it resulted in the maintenance of a high work hardening rate at high strains, as shown in Figure 5.22b). The work hardening curves followed similar trends (maintaining high work hardening rate at high strain) to steels which are known to exhibit a significant TRIP/TWIP effect. Maintaining high work hardening rates at high strain results in the delay of onset of necking and increases the ductility of the material [75].

Fracture surfaces and cross-section near the fracture surfaces of the tensile samples were analyzed using SEM. Ductile tearing and grain pull-out were observed on the fracture surfaces (Figure 5.24) which suggested that the main fracture mechanism was classic void nucleation and coalescence along the grain boundaries. Moreover, cross-sectional analysis

near the fracture surface, as shown in Figure 5.26, confirmed multiple microvoids and microcracks at the grain boundaries. Similar fracture mechanism was also observed by Bellhouse and McDermid [1], Zhang et al. [55] and De Cooman [32] for annealed low alloy TRIP-assisted steels. This suggests that similar fracture mechanism operated during the damage accumulation stage in both conventional low alloy and this experimental medium Mn TRIP steel.

### **6.3 Effect of Overaging Temperature Holding Time**

The effect of OT holding time was also investigated in this study in order to assess the effect of this process parameter on retained austenite stability as well as the mechanical property balance. The OT holding time was varied from 20s to 120s for both the S-TM and S-M samples. The higher IAT (710°C) and lower IAT (675°C) were chosen, respectively, for the S-TM and S-M samples as these temperatures yielded higher volume fraction of retained austenite compared to their counterpart IATs using the 20s OT holding time. In that regard, similar analysis techniques were used i.e. XRD, SEM, uniaxial and interrupted tensile tests and fractography.

The retained austenite volume fraction and C content of the retained austenite were determined by using XRD and can be found in Figure 5.28 and Figure 5.29. The S-TM samples showed a significant increase in retained austenite volume fractions for 60s and 120s OT holding times compared to 20s OT baseline samples (Figure 5.28 a)). However, the C content of the retained austenite did not change significantly, as shown in Figure 5.28 b), suggesting that the C content had already reached the equilibrium value and was no longer partitioning into the retained austenite. Hence, the increased volume fractions of

retained austenite might be attributed to Mn partitioning owing to longer OT holding times. However, atom probe tomography (APT) analysis needs to be done to confirm this hypothesis.

On the other hand, there was not any significant change in retained austenite volume fractions in the case of the S-M samples subjected to the 60s and 120s OT treatment compared to 20s OT baseline samples. Also, the C content of the retained austenite did not change significantly, as shown in Figure 5.29 b). This suggests a different mechanism may be behind the retained austenite stability for the S-M samples. As a result, APT analysis also needs to be done for these S-M samples and compare them with the S-TM samples to confirm this hypothesis. The microstructures of these annealed samples were analyzed using SEM (Figure 5.32) and the results correlated well with the XRD findings as shown in Figure 5.29. The microstructures of the S-M samples annealed with 60s and 120s OT holding times did not have any significant difference other than most of the retained austenite was present in the film shape along with other phase constituents.

The mechanical properties showed different trends depending on their heat treatment parameters. The S-TM 710°C + 120s samples subjected to 60s and 120s OT holding times showed a significant increase in yield strength and total elongation compared to the 20s OT baseline samples. However, the ultimate tensile strength decreased significantly in these samples (Figure 5.34 a)). This was likely due to an increase in chemically stable retained austenite after heat treatment. Moreover, work hardening rates of the S-TM 710°C + 120s samples with the 60s and 120s OT treatment showed similar trend (maintaining high work hardening rate at high strains) which are generally observed in steels exhibiting

TRIP/TWIP effect owing to significant amount of chemically stable retained austenite (Figure 5.36 a)). However, the  $UTS \times TE$  product was below the target mechanical properties for the 3G-AHSSs [14].

The S-TM 710°C + 240s samples showed a completely different trend. In this case, the total elongation decreased whereas the ultimate tensile strength increased with no significant difference between the 60s and 120s OT holding time samples (as shown in Figure 5.35 b)). Moreover, there was not any significant change in yield strength in these samples regardless of OT holding times. This implies the retained austenite was no longer sufficiently chemically or mechanically stable to promote the desired TRIP/TWIP effect in the S-TM samples annealed for longer time (>120s) at the 710°C IAT with 60s and 120s OT holding time. The interrupted tensile test results for these heat treatment condition also revealed that retained austenite transformed rapidly at low strains (Figure 5.38), confirming the hypothesis that the retained austenite was not chemically stable.

Both the S-M 675°C + 60s and S-M 675°C + 120s samples subjected to the 60s and 120s OT treatment showed similar significant increases in YS and decrease in UTS as well as TE compared to the 20s OT baseline samples. The  $UTS \times TE$  product decreased significantly for the S-M samples annealed with the 60s and 120s OT holding times owing to decreased stability of the retained austenite. However, this was not consistent with the XRD results (Figure 5.29) as well as work hardening rate plots (Figure 5.36) and interrupted tensile test results (Figure 5.39) which showed similar trends regardless of OT holding time. Furthermore, yield point elongation phenomenon was observed for the S-M samples with 60s and 120s OT treatments. Emadoddin et al. [76] reported that yield point

elongation can be reduced by increasing the volume fractions of stable retained austenite. Yield point elongation was still observed although the retained austenite amount was quite high in this study. Estrin and Kubin [27] suggested that the ultra-fine-grained microstructure in various materials resulted in localized deformation leading to Lüders strain owing to low work hardening rates. Gibbs et al. [25] reported significant yield point elongation for a 7.1Mn - 0.1C (wt.%) TRIP steel annealed at 600°C for 168 hours. It was concluded that this type of yielding was controlled by localized plastic deformation of strain aged recrystallized ferrite. Afterwards, homogenous plastic deformation and retained austenite transformation started and the gradual transformation of austenite increased the work hardening rate resulting in high strength and ductility balance. De Cooman et al. [69] also reported yield point elongation for a 7Mn (wt.%) TRIP steel intercritically annealed at 600°C and explained that the yield point elongation was promoted in conditions where the retained austenite had a higher C content. This resulted in more stable retained austenite with higher yield strength compared to ferrite. Moreover, the ferrite had low dislocation density and room temperature static strain aging took place in this ferrite. As a result, the yielding of the strain aged ferrite occurred prior to any retained austenite transformation, resulting in localized deformation by the nucleation and propagation of Lüder bands during yielding.

Xu et al. [50] studied the effect of tempering temperatures (100°C - 600°C) on the stability of retained austenite in a 0.2C-5Mn (wt.%) medium Mn steel with martensitic starting microstructure which was also ART annealed at 650°C for 6 hours. The authors reported high UTS (~1000 MPa) and ductility (~40%) for the samples tempered at 400°C

owing to significant volume fraction (~35%) of chemically stable retained austenite. Moreover, the retained austenite volume fraction decreased significantly for samples tempered at 500°C. As a result, the authors suggested 400°C to be the optimum tempering temperature for their medium Mn steel. In that regard, for future work, lower OT temperatures (~400°C) should be studied thoroughly for this experimental medium Mn TRIP steel in order to determine its effect on the retained austenite stability

In summary, different heat treatment conditions and starting microstructures were analyzed for a medium Mn TRIP steel. The resultant mechanical properties were assessed with respect to the target mechanical properties for 3G-AHSSs. S-TM samples annealed at 710°C IAT for 600s yielded mechanical properties in the range of the target mechanical properties for 3G-AHSSs. However, this condition was not compatible in terms of CGL processing. S-M samples, on the other hand, met the target mechanical properties with CGL compatible annealing conditions, annealing at 675°C IAT for 60s and 120s. The effect of OT holding time was also assessed in order to evaluate the robustness of the heat treatments. Although it increased the total elongation in some S-TM samples and yield strength in some S-TM and S-M samples, yield point elongation was observed suggesting Lüder type localized deformation. In future, the effect of lower OT temperature as well as more detailed more TEM work needs to be done to evaluate the effect of stacking fault energy (SFE) of retained austenite on both TRIP and TWIP effect. In addition, APT analysis also needs to be done to understand the effect of C and Mn in chemically stabilizing the retained austenite. Finally, the heat treatment parameters resulting in target mechanical properties should be assessed in terms of selective oxidation and reactive wetting.

## **7 CONCLUSIONS AND RECOMMENDATIONS FOR FUTURE STUDY**

### **7.1 Conclusions**

In this study, a prototype medium Mn TRIP steel was annealed using different heat treatment parameters and starting microstructures. The effects of intercritical annealing parameters, starting microstructure and overaging temperature holding time on the microstructure evolution and mechanical properties of the annealed samples were determined. Moreover, the mechanical properties were assessed in terms of the target mechanical properties for 3G-AHSSs to select CGL compatible heat treatment parameters. The following conclusions can be drawn based on the results observed in this investigation:

- 1) For 20s OT holding time, retained austenite volume fraction increased with holding time at 675°C and 710°C IATs for the S-TM samples, with the S-TM 710°C + 600s heat treatment yielding the highest volume fractions of retained austenite (~0.37) for this starting microstructure.
- 2) Similar volume fractions (~0.37) of retained austenite observed for the S-TM 710°C + 600s sample was achieved for S-M samples annealed at 675°C IAT for 60s, 120s and 360s with a 20s OT owing to the faster austenite reversion kinetics associated with the martensitic starting microstructure
- 3) The retained austenite decreased significantly when the IAT holding time was > 360s at 675°C and > 60s for the 710°C IAT for S-M samples owing to the presence of

chemically/mechanically unstable intercritical austenite that transformed to martensite during final cooling.

- 4) TEM analysis revealed that the retained austenite in the S-M samples had a film type morphology, which is known to be more chemically and mechanically stable compared to blocky retained austenite.
- 5) The S-TM 710°C + 600s, S-M 675°C + 60s, S-M 675°C + 120s and S-M 675°C + 360s samples had an excellent combination of strength and ductility ( $UTS \times TE > 30,000$  MPa%) owing to high volume fractions of chemically stable retained austenite.
- 6) The OT holding time had significant effect on both S-TM and S-M samples. For the longer (60s and 120s) OT treatments, the S-TM samples annealed at the 710°C IAT for holding times  $> 120s$  resulted in unstable retained austenite which transformed to martensite at low strain, yielding low  $UTS \times TE$  products (i.e.  $< 20,000$  MPa%).
- 7) For the S-M samples, longer (60s and 120s) OT treatments resulted in significant increases in yield strength. However, yield point elongation was observed in these samples. Moreover, the  $UTS \times TE$  products decreased significantly which might be attributed to decreased retained austenite stability.

Finally, based on the results of this project, it can be concluded that this prototype medium Mn TRIP steel, depending on the starting microstructure, can achieve 3G-AHSS target mechanical properties using CGL-compatible thermal processing cycles. Moreover, depending on successful reactive wetting, it may be possible to perform both thermal processing and galvanizing of this steel in the industrial CGL.

## **7.2 Recommendations for Future Study**

Some future work is recommended based on these results in order to fully understand the physical metallurgy and the galvanizability of this experimental medium Mn TRIP steel. The following recommendations can be considered as extensions of the present study:

- 1) Atom probe tomography (APT) analysis can be done in order to evaluate Mn and C partitioning in retained austenite. This would explain the effect of C and Mn in chemically stabilizing the retained austenite.
- 2) TEM analysis can be conducted to determine the stacking fault energy (SFE) of the retained austenite which would indicate the type of plasticity enhancing mechanisms operating in this steel.
- 3) The effect of lower overaging temperature ( $\sim 400^{\circ}\text{C}$ ) on retained austenite stability and the resultant mechanical properties should be determined.
- 4) A selective oxidation and reactive wetting study should be conducted on the S-M samples that met the target mechanical properties for 3G-AHSSs with CGL compatible heat treatment parameters.

## 8 REFERENCES

- [1] E.M. Bellhouse and J.R. McDermid, *Metall. Mater. Trans. A*, 41A (2010) 1539-1553.
- [2] A. Arlazarov, M. Gouné, O. Bouaziz, A. Hazotte, G. Petitgand and P. Barges, *Mater. Sci. Eng. A*, 542 (2012) 31– 39.
- [3] D.K. Matlock, J.G. Speer, E.D. Moor and P.J. Gibbs, *JESTECH*, 15 (2012) 1-12.
- [4] E. Ghassemieh, *Materials in Automotive Application, State of the Art and Prospects, New Trends and Developments in Automotive Industry*, Prof. Marcello Chiaberge (Ed.) (2011), ISBN: 978-953-307-999-8, InTech.
- [5] T.A. Swartzell, *Lightweighting and steel technologies in the all-new 2016 Chevrolet Malibu and 2017 Buick LaCrosse, Great Designs in Steel 2016*, Livonia, Michigan, USA (2016).
- [6] C. Shutte: *SAE Technical Paper 2015-01-0405* (2015), doi: 10.4271/2015-01-0405.
- [7] J.R. McDermid, private communication, May 21, 2015
- [8] R.H. Wagoner, *Report: Advanced High-Strength Steel Workshop*, Arlington, Virginia, USA, October (2006) 22–23.
- [9] P.J. Jacques, *Curr. Opin. Solid State Mater. Sci.*, 8 (2004) 259-265.
- [10] J.R. McDermid, H.S. Zurob and Y. Bian, *Metall. Mater. Trans. A*, 42A (2011), 3627-3637.
- [11] M. Ghasri-Khouzani and J.R. McDermid, *Mater. Sci. Eng. A*, 621 (2015), 118-127.
- [12] M. Blumenau, M. Nordan, F. Friedel and K. Peters, *Surf. Coat. Technol.*, 206 (2-3) (2011) 559-567.
- [13] O. Bouaziz, S. Allain and C. Scott, *Scripta Mater.*, 58 (2008) 484-487.

- [14] L.G. Hector Jr., R. Krupitzer and A.K. Sachdev, Proc. Intl. Symp. on New Develop. in Advanced High-Strength Sheet Steels, Vail, CO (2013) 341-349.
- [15] W.Q. Cao, C. Wang, J. Shi, M.Q. Wang, W.J. Hui and H. Dong, Mater. Sci. Eng. A, 528 (2011) 6661-6666.
- [16] S. Lee and B.C. De Cooman, Metall. Mater. Trans. A, 44A (2013) 5018-5024.
- [17] N. Nakada, K. Mizutani, T. Tsuchiyama and S. Takaki, Extended Abstracts of HMnS 2014 Conf., Aachen, Germany (2014) K2-89.
- [18] A. Marder, "The Metallurgy of Zinc-coated Steel," Progress in Materials Science, 45 (2000) 191-271.
- [19] Mr. E.A. Silva, private communication, U.S. Steel Research.
- [20] P. Jacques, Q. Furnémont, A. Mertens and F. Delannay, Philos. Mag., 81 (2001) 1789-1812.
- [21] S. Lee, K. Lee and B.C. De Cooman, Metall. Mater. Trans. A, 46A (2015) 2356-2363.
- [22] H. Luo and H. Dong, Mater. Sci. Eng. A, 626 (2015) 207-212.
- [23] R.A. Grange, C.R. Hribal, Edgar C. Bain Lab. Fundam. Res. Rep. No. 1453, USS, November 1968.
- [24] R.L. Miller, Metall. Trans. 3 (1972), 905–912.
- [25] P.J. Gibbs, E. De Moor, M.J. Merwin, B. Clausen, J.G. Speer and D.K. Matlock, Metall. Mater. Trans. A, 42A (2011) 3691-3702.
- [26] D.W. Suh, J.H. Ryu, M.S. Joo, H.S. Yang, K. Lee and H.K.D.H. Bhadeshia, Metall. Mater. Trans. A, 44A (2013) 286-293.

- [27] Y. Estrin and L.P. Kubin, *Continuum Models for Materials with Micro-structure*, H. E. Mühlhaus, ed., Wiley, New York (1995) 365.
- [28] S. Alibeigi, R. Kavitha, R.J. Meguerian and J.R. McDermid, *Acta Mater.*, 59 (2011) 3537-3549.
- [29] F.B. Pickering, *Physical Metallurgy and the Design of Steels*. London, UK: Applied Science Publishers Ltd.: 11 (1978).
- [30] E. Girault, A. Mertens, P. Jacques, Y. Houbaert, B. Verlinden and J. Van Humbeeck, *Scripta Mater.*, 44 (2001) 885-892.
- [31] J. Maki, J. Mahieu, B.C. De Cooman, and S. Claessens, *Mater. Sci. Technol.*, 19 (2003) 125–31.
- [32] B.C. De Cooman, *Curr. Opin. Solid State Mater. Sci.*, 8(2004) 285-303.
- [33] P. Jacques, Q. Furnémont, S. Godet, T. Pardoën, K. Conlon and F. Delannay, *Philos. Mag.*, 86 (2006) 2371-2392.
- [34] Q. Furnémont, M. Kempf, P. Jacques, M. Göken and F. Delannay, *Mater. Sci. Eng. A*, 328 (2002) 26-32.
- [35] E. De Moor, P.J. Gibbs, J.G. Speer, D.K. Matlock and J.G. Schroth, *AIST Trans.*, 7 (3) (2010) 133-144.
- [36] H.K.D.H. Bhadeshia, *ISIJ International*, 42 (2002) 1059-1060.
- [37] G.B. Olson and M. Cohen: *Metall. Trans. A*, 6 (1975) 791–795.
- [38] S. Lee and B.C. De Cooman, *Metall. Mater. Trans. A*, 45A (2014) 6039–6052.
- [39] A. Dumay, J.-P. Chateau, S. Allain, S. Migot, and O. Bouaziz, *Mater. Sci. Eng. A*, 483-484 (2008) 184–87.

- [40] S. Lee and B.C. De Cooman, *Metall. Mater. Trans. A*, 44A (2013) 3136–3146.
- [41] S.W. Lee, S.J. Lee, B.C. De Cooman, *Scr. Mater.* 66 (2012) 832–833.
- [42] G. Miyamoto, H. Usuki, Z.-D. Li and T. Furuhashi, *Acta Mater.*, 58 (13) (2010) 4492-4502.
- [43] N. Nakada, T. Tsuchiyama, S. Takaki and N. Miyano, *ISIJ Int.*, 51 (2) (2011) 299-304.
- [44] R. Wei, M. Enomoto, R. Hadian, H.S. Zurob and G.R. Purdy, *Acta Mater.*, 61 (2013) 697-707.
- [45] J. Han, S.-J. Lee, J.-G. Jung and Y.-K. Lee, *Acta Mater.*, 78 (2014) 369–377.
- [46] J. Shi, X. Sun, M. Wang, W. Hui, H. Dong and W. Cao, *Scripta Mater.* 63 (2010) 815-818.
- [47] H. Matsuda, H. Noro, Y. Nagataki and Y. Hosoya, *Mater. Sci. Forum*, 638-642 (2010) 3374-3379.
- [48] Y.-K. Lee and J. Han, *Mater. Sci. Technol.*, 31(7) (2015) 843-856.
- [49] H. Luo, *Scripta Mater.*, 66 (2012) 829-831.
- [50] H.F. Xu, J. Zhao, W.Q. Cao, J. Shi, C.Y. Wang, J. Li and H. Dong, *ISIJ Int.*, 52 (5) (2012) 868-873.
- [51] J. Han and Y.-K. Lee, *Acta Mater.*, 67 (2014) 354–361.
- [52] Garcia-Gonzalez, Ph.D. Thesis, University of Pittsburgh, 2005.
- [53] M.L. Brandt, Ph.D. Thesis, Northwestern University, 1997.
- [54] T. Furukawa, H. Huang and O. Matsumura, *Mater. Sci. Technol.*, 10 (1994) 964–970.
- [55] M. Zhang, L. Li, Y. Su, R. Fu, Z. Wan and B.C. De Cooman, *Steel Res. Int.*, 78 (2007) 501–505.

- [56] Q. Furnémont, P.J. Jacques and T. Pardoen, *Journal de Physique IV*, 11 (2001) Pr5-325-Pr5-332.
- [57] H. Yu, S. Li and Y. Gao, *Mater. Charact.*, 57 (2006) 160-165.
- [58] L. Chen, R. Fourmentin and J.R. McDermid, *Metall. Mater. Trans. A*, 39 (2008) 2128-2142.
- [59] ASTM E975-13, Standard Practice for X-Ray Determination of Retained Austenite in Steel with Near Random Crystallographic Orientation, ASTM International, West Conshohocken, PA, USA (2013).
- [60] R. Ruhl and M. Cohen, *Trans. TMS-AIME*, 245 (1969) 241-251.
- [61] D. Dyson and B. Holmes, *J. Iron Steel Inst.*, 208 (1970) 469.
- [62] ASTM Standard E 8M – 01ε2, Standard Test Methods for Tension Testing of Metallic Materials [Metric], ASTM International, West Conshocken, PA, USA.
- [63] E. De Moor, D.K. Matlock, J.G. Speer and M.J. Merwin, *Scripta Mater.*, 64 (2011) 185-188.
- [64] S. Lee, S.-J. Lee and B.C. De Cooman, *Scripta Mater.*, 65 (2011) 225-228.
- [65] B. Timokhina, P.D. Hodgson and E.V. Pereloma, *Metall. Mater. Trans. A*, 35A (2004) 2331-2341.
- [66] B.V.B Rao, *Metall. Trans. A*, 10(1979) 645.
- [67] K.W. Andrews, D.J. Dyson and S.R. Keown, “Interpretation of Electron Diffraction Patterns”, Plenum US (1967), DOI 10.1007/978-1-4899-6475-5.
- [68] M. Ghasri-Khouzani, PhD Thesis, McMaster University (2015).

- [69] B.C. De Cooman, P. Gibbs, S. Lee and D.K. Matlock, *Metall. Mater. Trans. A*, 44A (2013) 2563-2572.
- [70] X. Liang, J.R. McDermid, O. Bouaziz, X. Wang, J.D. Embury and H.S. Zurob, *Acta Mater.* 57 (13) (2009) 3978-3988.
- [71] P. Jacques, X. Cornet, Ph. Harlet, J. Ladriere and F. Delannay, *Metall. Mater. Trans. A*, 29A (1998) 2383-2393.
- [72] Y. Bian, M.A.Sc Thesis, McMaster University (2009).
- [73] P.J. Jacques, J. Ladriere and F. Delannay, *Metall. Mater. Trans. A*, 32A (2001) 2759-2768.
- [74] F.G. Caballero, C. Garcia-Mateo, J. Chao, M.J. Santofimia, C. Capdevila and C.G. de Andres, *ISIJ Int.*, 9 (2008) 1256-1262.
- [75] P.J. Jacques, E. Girault, Ph. Harlet and F. Delannay, *ISIJ Int.*, 41 (2001) 1061-1067.
- [76] E. Emadoddin, A. Akbarzadeh and G. Daneshi, *Mater. Sci. Eng. A*, 447(2007) 174-179.